Dissertation

submitted to the
Combined Faculties for the Natural Sciences and for Mathematics
of the
Ruperto-Carola University of Heidelberg, Germany
for the degree of

Doctor of Natural Sciences

Put forward by
Dipl.-Phys. Dirk Lennarz
Born in Mönchengladbach, Germany

Oral examination: October 17th, 2012

A Study of

Transient Very-High-Energy Gamma-Ray Emission from Gamma-Ray Bursts and Supernovae

with H.E.S.S.

Referees: Prof. Dr. Werner Hofmann
Prof. Dr. Stefan Wagner

Abstract

Gamma-ray bursts (GRBs) and supernovae (SNe) are well known examples of celestial transient events. Their tremendous energy release provides the ability to accelerate particles to the highest energies. The High Energy Stereoscopic System (H.E.S.S.) is an array of four imaging atmospheric Cherenkov telescopes, covering gamma-ray energies between 100 GeV and 100 TeV (VHE range). In this work the H.E.S.S. data on GRBs are searched for VHE gamma-ray emission. Amongst them is the analysis of GRB 100621A, the brightest X-ray source so far detected by the *Swift* satellite. Measurements at lower energies make it a promising candidate within the sensitivity reach of the H.E.S.S. instrument, however no indication of VHE emission is found. The derived upper limits constrain the existence of additional spectral components and provide important input for understanding the emission process. Furthermore, H.E.S.S. pointing positions are compared to a recently created, unified SN catalogue in order to identify extragalactic SNe accidentally in the field of view during the observation of other targets. The analysis reveals no significant detection, which allows one to constrain possible VHE emission scenarios. This work also includes a technical discussion of the H.E.S.S. telescope pointing accuracy. A new approach, the SingleCCD concept, is discussed and evaluated, which is interesting for the next generation of imaging atmospheric Cherenkov telescopes.

Kurzfassung

Gammablitze (GRBs) und Supernovae (SNe) sind bekannte Beispiele transienter Himmels-Ereignisse. Durch die enorme Menge an freigesetzter Energie haben sie die Möglichkeit, Teilchen auf die allerhöchsten Energien zu beschleunigen. Das High Energy Stereoscopic System (H.E.S.S.) besteht aus vier abbildenden, atmosphärischen Tscherenkow-Teleskopen, die Gammastrahlungs-Energien zwischen 100 GeV and 100 TeV (VHE Bereich) abdecken können. In dieser Arbeit werden die H.E.S.S. Daten von GRBs auf VHE Gammastrahlungs-Emission untersucht. Unter ihnen ist auch die Analyse von GRB 100621A, der hellsten Röntgenquelle, die bisher vom *Swift*-Satellit detektiert wurde. Messungen bei niedrigeren Energien zeigen, dass es ein vielversprechender Kandidat innerhalb des Sensitivitätsbereichs des H.E.S.S. Instruments ist, allerdings wurden keine Anzeichen für VHE Emission gefunden. Die daraus ableitbaren Flussobergrenzen schränken die Existenz zusätzlicher spektraler Komponenten ein und geben einen wichtigen Beitrag zum Verständnis des Emissionsprozesses. Des Weiteren wurden die H.E.S.S.-Beobachtungsrichtungen mit einem kürzlich veröffentlichten, vereinigten SN-Katalog verglichen, um extragalaktische SNe zu identifizieren, die sich zufällig im Blickfeld bei der Beobachtung anderer Quellen befinden. Die Analyse zeigt keine signifikante Detektion, wodurch man mögliche VHE Emissions-Modelle einschränken kann. Diese Arbeit beinhaltet auch eine technische Diskussion der Genauigkeit der H.E.S.S. Teleskopausrichtung. Ein neuer Ansatz, das SingleCCD-Konzept, wird diskutiert und ausgewertet, welches interessant für die nächste Generation abbildender, atmosphärischer Tscherenkow-Teleskope ist.

Werke dauern lange, so lange, wie sie uns beschäftigen. Je länger sie dauern, umso reicher können sie werden. Was fertig ist, was niemanden mehr berührt, ist am Ende!

Günter Behnisch - German Architect

Contents

List of Figures

List of Tables

Chapter 1

Introduction

Astronomy, unlike any other natural science, provides a remarkable and universal fascination and interest to people from different cultures and backgrounds. This may also be one of the reasons why it is one of the oldest sciences, already studied by prehistoric cultures. During the Renaissance astronomical knowledge had a great impact on the scientific revolution and definitely changed people's view of the world. Apart from its huge cultural impact, astronomy is also a remarkable example of human innovation and progress. Step by step the complete electromagnetic spectrum, in addition to visible light, became accessible to mankind, leading to new fields like radio, X-ray, ultraviolet and infrared astronomy. This thesis deals with the last electromagnetic window to the universe, which was opened in the 1960s. However, due to experimental challenges, gamma-ray astronomy, covering photon energies above $\sim 100\,\mathrm{keV}$, needed some time to mature.

Exactly one hundred years ago (in 1912) Victor Hess discovered a radiation of cosmic origin, which soon became known as *cosmic rays* [1]. The energy spectrum of the cosmic rays extends over about 13 orders of magnitude in energy and in that range covers approximately 31 orders of magnitude in flux (see Fig. 1.1). The flux is at most energies nearly isotropic with deviations of less than 0.1% [2]. Cosmic rays, composed of charged nuclei, are accelerated by cosmic particle accelerators. But even a hundred years after their discovery a main question remains: how and where are particles accelerated to such enormous energies?

Gamma-ray astronomy might be the key to solve the question related to the cosmic accelerators. Cosmic rays are deflected by magnetic fields and their spectrum is modified by the escape of particles from the galaxy. Photons on the other hand, are particles without charge and mass that do not decay. Their spectra and fluxes directly reflect those of the accelerated particles and thus provide important insights into the physics of the sources. At high energies the absorption in matter is comparably low, which makes them good astronomical messenger particles.

The energy range of gamma-ray astronomy ($\gtrsim 100\,\mathrm{keV}$) covers at least 14 decades in energy. In can be divided into four different bands: the medium-energy (ME) band from 100 keV to 30 MeV, the high-energy (HE) band from 30 MeV to 100 GeV, the very-high-energy (VHE) range from 100 GeV to 100 TeV and the ultra-high-energy (UHE) regime above 100 TeV. Several detection methods are required to cover this huge range in energy. The energy bands are not motivated by the physics of the sources, but by the differences in their detection techniques.

In this thesis the VHE regime of gamma-ray astronomy will be covered. Gamma rays in this energy range are measured by detecting the electromagnetic cascade that develops when a VHE photon interacts with the Earth's atmosphere. Imaging Atmospheric

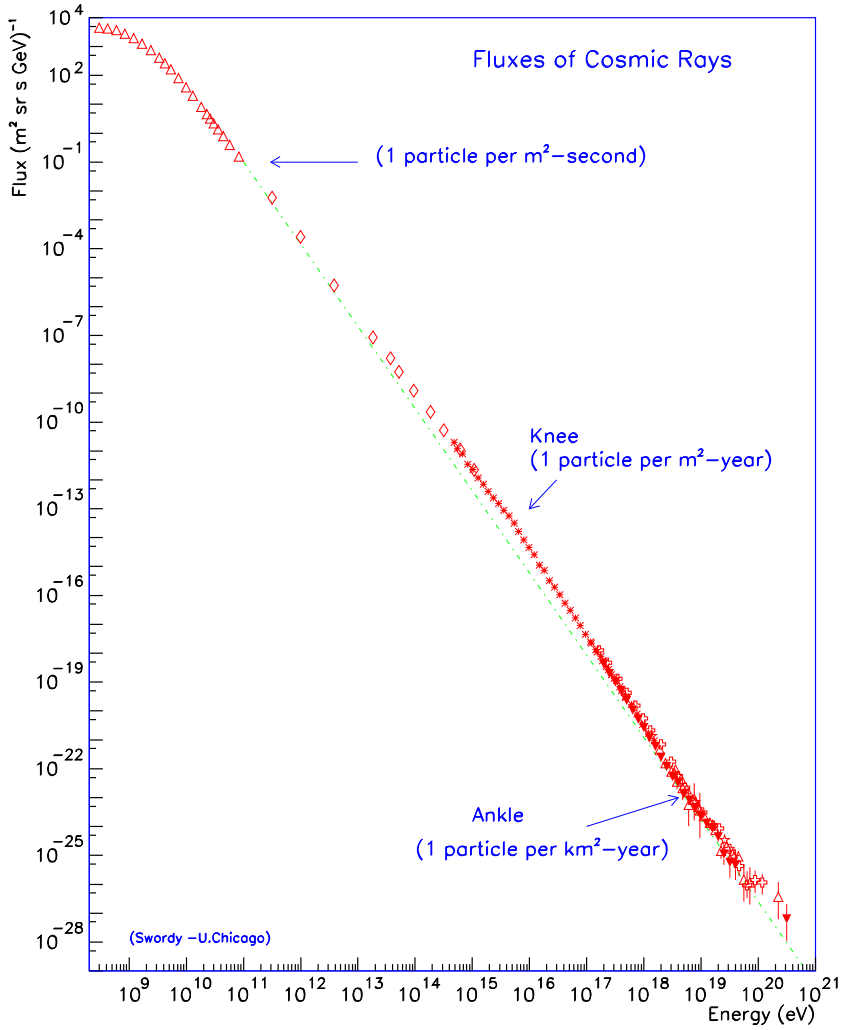

Figure 1.1.: Energy spectrum of the cosmic rays as measured by various experiments [3].

Cherenkov Telescopes (IACTs) can reconstruct the direction and energy of the incoming gamma ray by detecting Cherenkov light emitted by the charged particles in the electromagnetic shower. A detailed discussion on IACTs can be found in Chapter 2. The High Energy Stereoscopic System (H.E.S.S.) has been a very successful IACT that immensely enhanced the number of known VHE sources. Its details are described in the same chapter.

An important calibration for IACTs is the so-called "pointing". It is the capability to relate the events seen in the telescope camera to the precise origin in the sky. Mechanical deformations of the telescope make this transformation non-trivial. The current way of determining the H.E.S.S. pointing is described in Chapter 3. Two optical CCD cameras are used to monitor the movement of the telescope camera and the sky at the same time. During this thesis a hardware replacement has started and the impact on the H.E.S.S. pointing is evaluated in the same chapter. Furthermore, a new approach to

the telescope pointing is investigated. Chapter 4 summarises the results of replacing the current approach with two CCDs by a single CCD.

Main subject of this thesis is the search for VHE emission from transient events, which are astronomical objects or phenomena that can only be detected during a limited time scale, ranging from seconds to years. One examples of such transients are supernovae (SNe). In 1572 the famous Danish astronomer Tycho Brahe observed the sudden appearance of a new and bright celestial object. He discussed his discovery in a book called *de nova et nullius aevi memoria prius visa stella*, which is Latin for "concerning the new and never before seen star". This coined the term *nova* for this kind of phenomena. It was not until the beginning of the 20th century that people realised that novae can be divided into different classes according to their luminosity. Fritz Zwicky and Walter Baade coined the term "super-novae" for the more luminous novae. They also postulated that SNe originate in the catastrophic explosions of stars and linked the newly discovered cosmic rays to these events [4]. Furthermore, they correctly suggested the gravitational collapse of the stellar interior as an energy source and predicted a remnant made of densely-packed neutrons, which they called "neutron" star. This visionary idea was proven in 1967, when radio astronomers discovered the first pulsar and it became clear that these objects could only be rapidly spinning neutron stars. Chapter 5 gives a short introduction to the physics of SNe and discusses possible scenarios of VHE emission. H.E.S.S. observations of nearby SNe are selected using a recently created, unified SN catalogue and analysed for signs of VHE emission. The consequences of the H.E.S.S. results on the VHE emission scenarios are discussed.

Another example of transient events are gamma-ray bursts (GRBs). Their emission peaks in the gamma-ray band and for the brief time they last, they can outshine every other gamma-ray source in the sky. They happen at random locations and to our current knowledge they are not recurrent. The first GRB was discovered serendipitously on July 2, 1967 by the American series of satellites called *Vela* [5]. These were military satellites designed to monitor violations of the Nuclear Test Ban Treaty. Fortunately it was realised that the signal was not characteristic for a nuclear test. After the first discovery more events of the same kind were discovered in the data. The results were not published until 1973, when the detection of 16 bursts during a three-year period was reported. Chapter 6 summarises the observational progress on GRB observations and the currently accepted model for GRBs. Their tremendous energy release provides the ability for particle acceleration up to the highest energies, thus these transient events are natural candidates to search for the emission of VHE gamma rays. Up to now there has been no detection of VHE emission from GRBs. However, such a measurement would be important to further characterise the acceleration mechanisms. The H.E.S.S. GRB programme and the analysis of GRBs that H.E.S.S. has observed in the last years are presented.

Chapter 2

Imaging Atmospheric Cherenkov Telescopes

This chapter starts with an introduction into the basic detection principle of an Imaging Atmospheric Cherenkov Telescopes (IACT). In Sec. 2.2 the experimental backgrounds are discussed in more detail. Then the High Energy Stereoscopic System (H.E.S.S.) from which the data analysed in this work are obtained is described. Section 2.4 discusses the data analysis chain that is used to obtain the results presented in the later chapters.

2.1. Introduction

The atmosphere of the Earth is nontransparent to gamma rays. In order to avoid the absorption in the atmosphere, large balloons that go to the top of the atmosphere or space-born detectors can be used. The biggest challenge for gamma-ray telescopes is the fact that gamma rays above $\sim 1\,\mathrm{MeV}$ cannot be focused. Furthermore, fluxes are getting low at the highest energies, which would require larger collection areas. For space missions a compromise has to be found between detector size and the payload of the spacecraft. It is a lucky coincidence in Nature, that at the maximum energy that can be reached for satellites it is again possible to use ground-based instruments, although the atmosphere is still opaque at these energies.

2.1.1. Electromagnetic Showers

A primary photon that enters the atmosphere initiates an electromagnetic shower. These showers originate from a combination of photon and electron or positron energy loses. The most important features can be easily understood in a toy model approach first introduced by Heitler [6] (see Fig. 2.1). In the following discussion the term electron will be used for e^- and e^+ at the same time.

The simple model is based on three assumptions. Firstly, electrons and photons undergo repeated two-body splittings by only two different processes: the photons interact via pair production, while the electrons, feeling the electric field of the surrounding material, lose energy via one-photon bremsstrahlung. Secondly, each particle interacts after travelling one splitting length:

$$\lambda = X_0 \ln 2 \ , \tag{2.1}$$

where X_0 is the radiation length of the corresponding medium. A splitting length is the distance over which the electrons lose, on average, half of their energy and is roughly

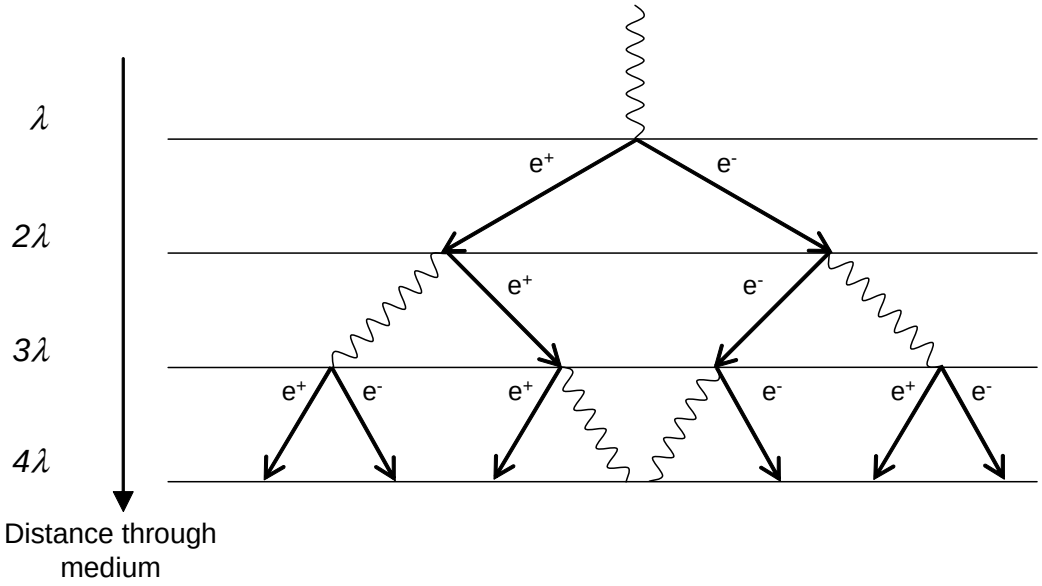

Figure 2.1.: A schematic view of a simple model for an electromagnetic shower. Photons and electrons/positrons undergo repeated two-body splittings after each splitting length λ.

the mean free path of the photon (which is $9/7X_0$). The third assumption is that in each two-body splitting the energy is equally shared amongst the products. Hence, at each iteration the number of particles doubles and the particle energy is cut in half. After n iterations, for an incident photon of energy E_0, the number of particles is 2^n and their average energy is $E_n = E_0/2^n$. Multiplication stops when E_n is too low for pair production or bremsstrahlung. Heitler sets this point at the critical energy E_c, which is the energy when the electron energy loss for bremsstrahlung equals the ionisation energy loss in collisions. The critical energy decreases with the atomic number of the medium and is about 85 MeV in air.

The cascade reaches the maximum number of particles ($N_{\max}$) when all particles are at the critical energy, so conservation of energy demands:

$$E_0 = E_c N_{\max} \tag{2.2}$$

This maximum is more commonly expressed as the number $n_{\max}$ of splitting lengths. Since $N_{\max} = 2^{n_{\max}}$ it follows from Eq. 2.2 that $n_{\max} = \ln(E_0/E_c)\ln 2$, thus giving with Eq. 2.1:

$$X_{\max} = n_{\max}\lambda/\ln 2 = X_0 \ln(E_0/E_c) \tag{2.3}$$

This simple model correctly predicts two basic features of real electromagnetic showers: the maximum number of particles in the shower is proportional to the energy of the primary photon and the depth of the shower is proportional to the logarithm of the energy. Monte Carlo simulations show that the depth estimated from Eq. 2.3 is already a very good approximation. There are however some shortcomings in this simple model. Firstly, the Heitler model overestimates $N_{\max}$, since it does not take into account attenuation of

particle numbers. Furthermore, the composition of the shower maximum (in the Heitler model, 1/3 photons and 2/3 electrons) has too many electrons. The main reasons are that often more than one bremsstrahlung photon is created and many electrons are absorbed in the air. In actual showers the photons greatly outnumber the electrons.

The first interaction typically happens after the gamma ray traversed one radiation length of atmosphere, which is at an typical altitude of 20 km above sea level. The shower maximum is approximately at 8 km for a 1 TeV primary photon.

2.1.2. Cherenkov Radiation

The electrons and positrons induce Cherenkov emission in the atmosphere. Cherenkov radiation is emitted from a dielectric medium if the velocity of a charged particle in that medium exceeds the local speed of light. The particle induces a polarisation that is asymmetric along the particle trajectory. This creates a residual electric field and emits coherent electromagnetic radiation. The Cherenkov photons are emitted under a characteristic angle θ_c, for which the following relation holds true:

$$\cos\theta_c = \frac{1}{n\beta} \ , \tag{2.4}$$

where β is the velocity of the particle in units of the vacuum speed of light and n the index of refraction of the medium.

The emission occurs over a broad wavelength band and is peaked in the ultraviolet. From Eq. 2.4 it can be seen that there is a threshold energy for the production. There is an analogy to supersonic shocks for sound, as the sonic boom is only produced when an object exceeds the velocity of sound in the medium.

2.1.3. Detection on the Ground

In the VHE regime the secondary electrons and positrons are almost completely absorbed before they reach the ground. The Cherenkov light, however, will suffer little atmospheric absorption and can reach the ground. Two effects are important for how the shower is seen on the ground. With increasing density of the atmosphere the refraction index becomes bigger and thus the Cherenkov angle broadens. At the same time the distance the emitted photons can travel to the ground decreases. Thus the Cherenkov photons illuminate a circle of about 100 m radius around the shower axis with an optical photon density of about 100 photons/m^2 at ground level for a 1 TeV primary photon.

The Cherenkov light can be collected and focused by an optical telescope, typically onto on array of fast photomultipliers. With this image it is possible to reconstruct the direction and energy of the incoming gamma ray. The typical timescale for a Cherenkov light pulse is about 10 ns, so a good time resolution is critical. Since the brightness of the Cherenkov light is very low, observations are typically carried out during clear, moonless nights, leading to a duty factor of about 10-20%. It also means that telescopes have to be build far away from manmade light sources like e.g. city lights. IACTs typically have a much larger effective area compared to satellite experiments. This is because the telescope can be anywhere inside the Cherenkov light pool on the ground. The effective area at high energies is nearly independent of the mirror collection area, which only determines the minimum gamma-ray energy that can be measured.

2.2. Experimental Backgrounds

There are various experimental backgrounds that have to be controlled when operating IACTs. The most important one is the hadronic cosmic-ray background because the sensitivity of the instrument is directly determined by the capability to suppress this background.

2.2.1. Hadronic Cosmic Rays

When a hadronic cosmic ray (p, He,...) enters the atmosphere it also creates a shower, which is superficially similar to the electromagnetic shower discussed before. The interaction happens via the strong force and the scattering is inelastic. For the development of the hadronic shower the production of charged and neutral pions is most important and for the simplified model discussed now it can be assumed that all particles are of this kind.

Also hadronic showers can be discussed in a simple Heitler like model, where the splitting length λ is now the interaction length of strongly interacting particles. Hadrons interact after travelling one interaction length and at each interaction create two-third charged and one-third neutral pions. The neutral pions can be assumed to immediately decay, thus creating electromagnetic subshowers. The charged pions travel another interaction length, interact again and produce the second generation of pions. Multiplication stops when the individual pion energy drops below a critical energy, when it becomes more likely for the $\pi^{\pm}$ to decay rather than to interact. The charged pions decay into muons which can then reach the ground.

An important difference to electromagnetic showers is that the neutral pions remove at each interaction one-third of the energy for new cascade particle production. However, the particles created in these electromagnetic cascade are the ones that emit most of the Cherenkov light. This means that a 300 GeV photon produces roughly the same amount of Cherenkov light than a 1 TeV proton. Since charged cosmic rays are about $10^3 - 10^4$ times more numerous than gamma rays and have a similar Cherenkov emission, this background needs a very efficient suppression.

The lateral extension of a shower is determined by the transverse momenta of the secondary particles. Inelastic hadron-nucleon scattering leads to high transverse momenta, compared to the lateral spread of electromagnetic showers that is caused by multiple scattering. Thus hadronic cascades are much broader and more scattered than electromagnetic ones. This can be seen in Fig. 2.2, which shows a Monte Carlo simulation of the development of an electromagnetic and hadronic shower. It can also be seen that fluctuations in the development of a hadronic cascade lead to a much more irregular pattern of Cherenkov light on the ground. Discrimination between electromagnetic and hadronic showers can be done by exploiting these differences (see section 2.4).

2.2.2. Night Sky Background

Another kind of background comes from the general brightness of the night sky, the night sky background (NSB). However, for a detector composed of several photomultipliers it can be very effectively suppressed on trigger level. A first reduction comes from the

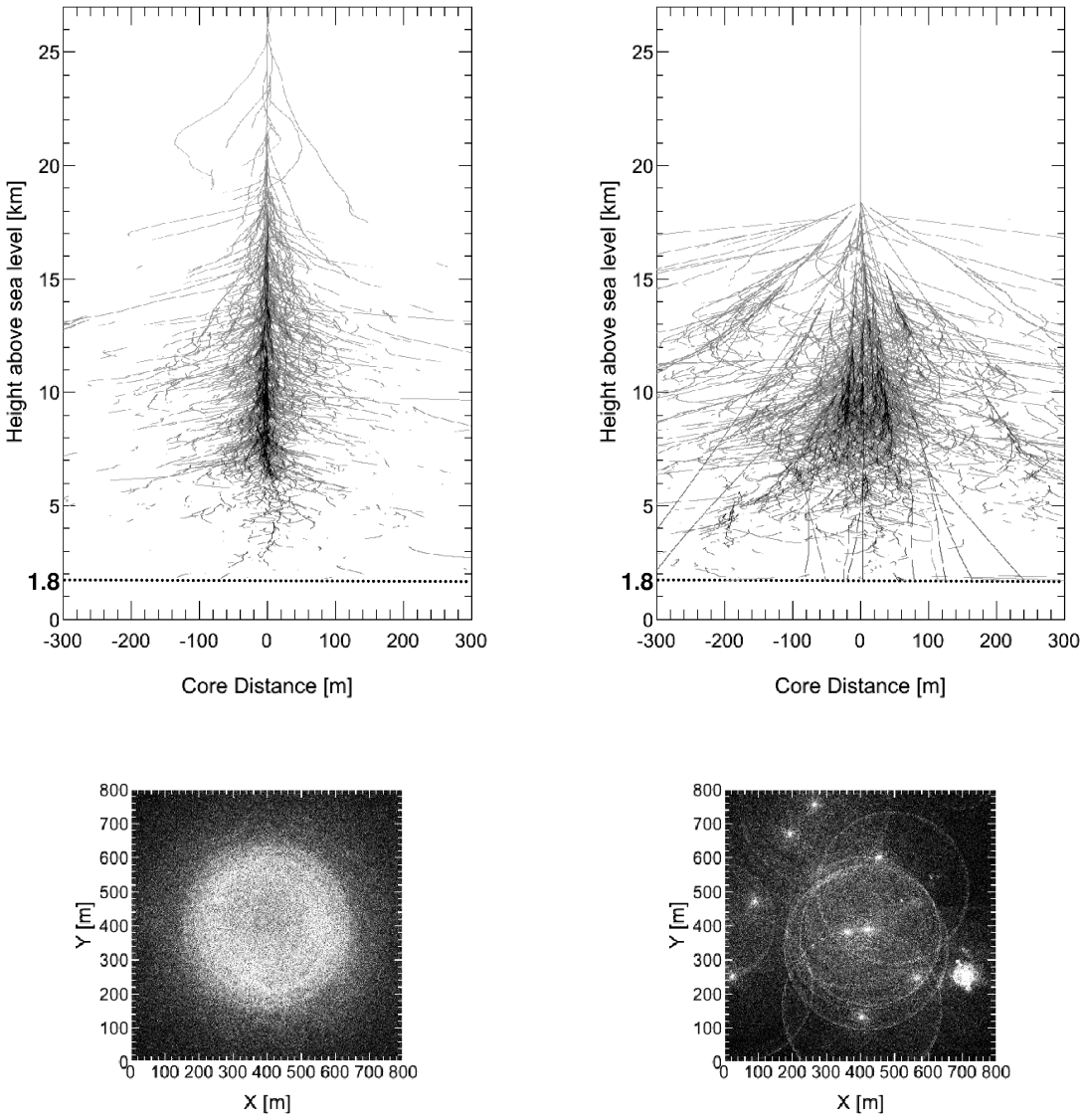

(a) 300 GeV gamma-ray

(b) 1 TeV proton

Figure 2.2.: Comparison between Monte Carlo simulations of a 300 GeV gamma ray (left) and a 1 TeV proton (right) for a detector 1.8 km above sea level (by K. Bernlöhr using sim_telarray [7]). In the upper panel the tracks of individual Cherenkov light emitting particles are shown in an (y,z) projection where the darkness of the particle tracks corresponds to the amount of produced Cherenkov light. The lower panel shows the distribution of Cherenkov light on the ground.

threshold of the individual photomultiplier. Lowering the photomultiplier threshold increases the sensitivity to lower energetic showers, but also creates more random triggers from the NSB. Secondly, since the typical timescale for a Cherenkov light pulse is about 10 ns, a fast coincidence trigger can be used for various photomultipliers. And finally, if various telescope are used to see the same shower a trigger can be introduced by demanding another coincidence between telescopes. Such "stereoscopic" observations have other advantages as well as discussed later.

2.2.3. Cosmic Electron Background

Electromagnetic cascades in the atmosphere can also be induced by cosmic electrons. They are a factor of 100-1000 times less numerous than hadronic cosmic rays, but suppression is much more complicated. As discussed before the mean free path length of photons is slightly higher than the one for electrons. This results in a slightly higher first interaction point (and therefore shower maximum) for electrons compared to gamma rays. The current generation of IACTs cannot use this for separation, but the next generation of IACTs might be able to do so [8].

2.3. The High Energy Stereoscopic System

The section starts with a short overview of past and present IACTs. Then the components of the High Energy Stereoscopic System (H.E.S.S.) are discussed. Finally a short outlook to H.E.S.S. II is given.

2.3.1. Overview

The first solid detection of a VHE source was made with the Whipple 10 m gamma-ray telescope in 1989 [9]. After more than one year of observation the Crab Nebula was detected, a steady, bright source that has become the standard reference source for VHE astronomy. The next generation of Cherenkov telescopes, e.g. the HEGRA system, featured arrays of multiple telescopes. As it will be seen in this chapter, stereoscopic observations have various advantages, besides the better night sky background suppression already discussed. Currently three major imaging Cherenkov telescope arrays are operational: H.E.S.S., the Major Atmospheric Gamma-Ray Imaging Cherenkov (MAGIC) telescopes [10] and the Very Energetic Radiation Imaging Telescope Array System (VERITAS) [11]. They consist of 2-4 telescopes. The next generation of IACT, e.g. CTA, will be comprised of a much larger number of telescopes $\mathcal{O}(20-100)$ for improved sensitivity and energy range.

The first phase of H.E.S.S. is comprised of four telescopes. H.E.S.S. started data taking in June 2003, when the first telescope was ready. All four telescopes became operational in December 2003 [12]. The second phase of H.E.S.S. will add another telescope and is described separately below.

2.3.2. Components of H.E.S.S.

H.E.S.S. is located 1800 m above sea level in the Khomas Highland of Namibia. Figure 2.3 shows an aerial view of the H.E.S.S. site. The telescopes are arranged in a square with 120 m side length with one diagonal oriented north-south.

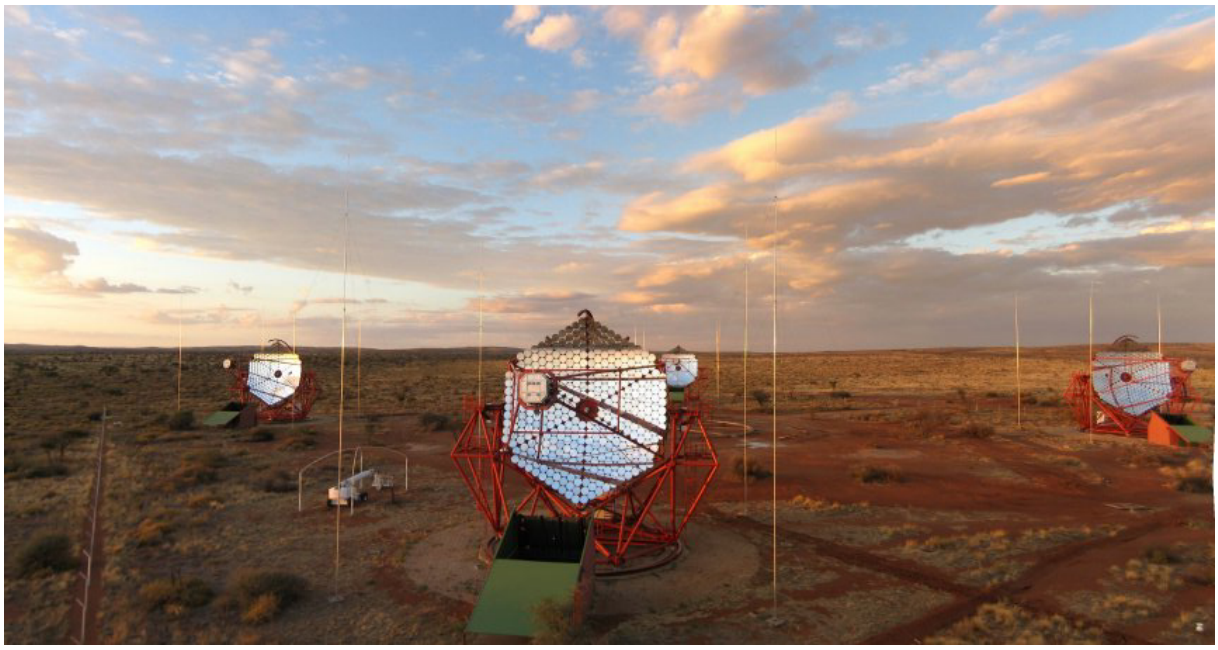

Figure 2.3.: Aerial view of the H.E.S.S. telescopes (from D. Nedbal).

Mount and Dish

The telescopes have an altitude-azimuth mount, which implies that each drive system has two separate motors. The basis of the telescope rotates on circular rails of about 7 m radius around the azimuth axis and carries the dish, which rotates around the altitude axis. The telescope is driven by a computer controlled drive system that allows to track celestial objects across the sky. It has a maximum speed of about 100 °/min to repoint the telescope. The steel structure was designed for high rigidity, which is important for the telescope pointing discussed in Chapter 3. The weight of one telescope including all components like mirrors and camera is about 60 t.

Reflector

As discussed before, the telescope should have a large collection area to lower the energy threshold. One way of achieving this is the Davies-Cotton design [13]. It uses tessellated spherical mirrors of equal focal length. They are located on an optical support structure with the same radius of curvature than the focal length. A Davies-Cotton reflector is easy to built and provides a good image quality out to a few degrees from the optical axis, since off-axis aberrations are smaller compared to a parabolic reflector. However, the surface is not isochronous, meaning a spread in the arrival time of the light.

H.E.S.S. has a $\sim 100\,\mathrm{m}^2$ tesselated mirror surface composed of 380 quartz-coated mirrors of aluminised glass. The facets are of 60 cm diameter and arranged in a Davies-Cotton

design with a focal length of 15 m. Each mirror facet has two remote-controlled motors that allow to align them. To this end the projection of a star is monitored by a CCD camera in the centre of the dish when the facet is moved. After alignment the 80% containment radius of the optical point spread function is smaller than 0.08° (or half the diameter of one pixel, see below) out to 2 ° off-axis. Detailed information on the optical characteristics can be found elsewhere [14, 15].

Camera

Each H.E.S.S. telescope is equipped with a pixelated camera of 960 photomultiplier tubes (PMTs) arranged in a hexagonal design. The advantage of a pixelated camera was already pointed out for reducing the night sky background. The advantage of PMTs is that they can provide the required nanosecond resolution and single-photon detection, but they have to be operated at high voltage and can easily be damaged by excessive light. For the choice of the PMT it is important to consider that Cherenkov photons in the atmosphere suffer absorption (mostly by ozone) and Rayleigh and Mie scattering. This shifts the peak of the Cherenkov light emission from ultraviolet to blue. Luckily, PMTs with a peak sensitivity between 300-450 nm are available and the NSB is near its minimum.

In front of each PMT pixel is a Winston cone light concentrator (called *funnel*) to improve the light collection efficiency (see Fig. 2.4). One pixel subtends approximately 0.16°, resulting in a field of view of 5° in diameter. The funnels are fixed with the help of a funnel plate and the camera is protected by a so-called lid from sunlight and dust. It covers the camera and is only opened during observations. Eight positioning LEDs are attached radially symmetric to the corners of the hexagon to monitor the position of the Cherenkov camera (important for pointing, discussed in Chapter 3). The red LED light is guided with the help of optical fibers to so-called *diffusers*. They focus the light to a plane aligned with the funnel entrance windows.

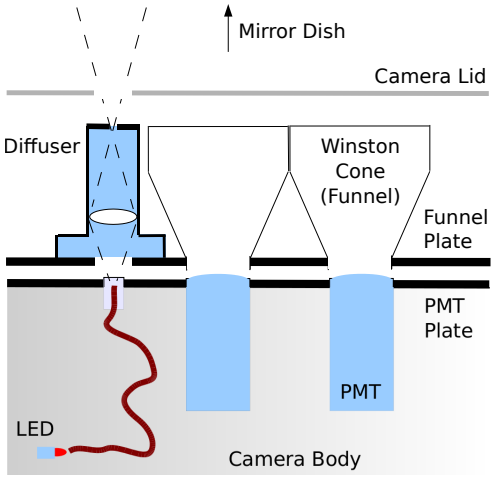

Figure 2.4.: Schematic view of a H.E.S.S. Cherenkov camera (from I. Braun and C. van Eldik). Each PMT pixel has a Winston cone in front to concentrate the light onto the pixel. The LEDs with the diffusers are used to measure the position of the Cherenkov camera, which is important for the telescope pointing.

Each PMT pixel has three electronics channels, one for triggering and two data channels

with different gains. PMT signals are stored in a 1 GHz analog ring sampler, which buffers 128 ns of data. This is needed because a readout decision needs 70-80 ns to be computed and distributed to the ring samplers. The camera has a diameter of about 1.6 m and a weight of about 800 kg. During operation 5 kW of heat are dissipated with air cooling.

Trigger

The triggering is done in three different stages at PMT level, at camera and at array level. The camera is divided in overlapping 8x8 pixel sectors. A typical pixel trigger threshold is about 5 photoelectrons and a camera trigger is issued once a coincidence of signals in a certain number of pixels (3-4) of one sector is detected. For a typical PMT pulse shape the effective coincidence window is only about 1.3 ns which efficiently rejects uncorrelated PMT signals from the NSB.

The camera triggers are sent to a central trigger station. Only events seen by at least two of the four telescope are accepted in order to allow stereoscopic image analysis (explained in the next section). For such events a trigger confirmation is sent back to the telescopes and the data in the analog ring sampler is digitised and read out. Detailed information on the trigger system can be found elsewhere [16].

2.3.3. H.E.S.S. Phase II

In the second phase of H.E.S.S. a large Cherenkov telescope is placed in the centre of the four H.E.S.S. I telescopes. The construction was recently finished and the telescope had first light in July 2012. The new telescope is the largest Cherenkov telescope ever built. It has a focal length of $\sim 36\,\mathrm{m}$ and an increased mirror area of $\sim 600\,\mathrm{m}^2$. Each of the ~ 850 mirror tiles has a hexagonal shape and a flat-to-flat size of 90 cm. The diameter of the PMT pixels is the same as for H.E.S.S. I, but due to the increased focal length each pixel now subtends only 0.067° of the sky. The H.E.S.S. II camera consists of 2048 PMTs, which results in a total field of view of 3.2°.

H.E.S.S. II will improve the sensitivity of the current system and even more important extend the energy range to an expected threshold of $\approx 30\,\mathrm{GeV}$. Thus phenomena so far only accessible with the current generation of satellite-borne detectors in the high-energy range, like e.g. gamma-ray bursts (see Chapter 6), should become accessible. An important fact for the detection of transients is the fact that the H.E.S.S. II drive system, with a design speed of about $200\,^\circ/\mathrm{min}$, will be much faster than the old telescopes. For GRBs it will be shown in Chapter 6 that a speedy follow-up is advantageous, which is guaranteed by the fast drive system.

2.4. H.E.S.S. Standard Data Analysis

In this section the H.E.S.S. standard data analysis is described. It will be applied in the later chapters when the H.E.S.S. data on supernovae and gamma-ray bursts are analysed. In a first step the raw data are processed, which includes data quality selection, calibration and image cleaning. Then a Hillas reconstruction and analysis are performed. More information on the involved steps can be found elsewhere [17].

2.4.1. Data Quality Selection

Before H.E.S.S. data is used in analysis it undergoes a standard quality test to remove observations with hardware problems. Observations are divided into so-called *runs* with a nominal length of 28 min. The most important hardware criterion is the number of active pixels in the camera. In order to protect the PMTs they have an over-current protection that switches them automatically off if the current becomes too high. Over-current due to bright stars can be predicted and the pixels are switched on again after the star transit. Occasionally other bright transients (meteorites, lightnings, airplanes or satellites) cause PMTs to be switched off until the end of the run. The run is rejected if more than 120 pixels have hardware problems or more than 50 pixels were switched off.

As will be explained below, the atmosphere has a systematic effect on the energy reconstruction. Hence, for spectral analysis data collected during unstable weather conditions are also rejected. The presence of clouds or dust in the atmosphere absorbs Cherenkov light, which leads to fluctuations in the system trigger rate. If the variations in the trigger rate are too high (above 10%) or the trigger rate deviates by more than 30% from the expected rate the run is rejected. The estimation of the expected rate includes the fact that the trigger rate is a function of zenith angle and the optical performance of the telescopes.

Further data quality cuts include the stability of the tracking and the trigger. Only runs with a nominal length of 10 min pass the data quality selection.

2.4.2. Calibration

The PMTs provide an analog signal that needs to be digitised and converted to a number of photoelectrons. The most important parameters are the flat-field coefficients, the pedestal and the gain, which is the conversion factor between counts and photoelectrons. The flat-field coefficients level the response of the camera to a homogeneous exposure of light. A flat-fielding unit is installed on each telescope that can provide the required light signal. The pedestal is the mean count value without any light exposure and can be determined with special observations when the camera is covered from external light. The count conversion factor is obtained with the help of a single photoelectron unit. It illuminates the camera with a pulsed LED. In the recorded count spectrum two peaks can be identified, the pedestal peak which corresponds to pixels without any signal and the single photoelectron peak. More information on the calibration can be found elsewhere [18].

2.4.3. Image Cleaning

In order to improve the accuracy of the image analysis an image cleaning is performed first. The camera contains photons that are unrelated to the Cherenkov shower, e.g. from NSB. In the standard procedure all pixels containing a signal of more than 10 or 5 photoelectrons are kept if they have a neighbouring pixel with more than 5 or 10 photoelectrons, respectively.

2.4.4. Event Reconstruction

Figure 2.5 shows the basic geometry of an event recorded by an IACT. The shower geometry can be described by two parameters: the direction of the incoming gamma ray, called *shower direction* and the intersection of the extrapolation of the primary particle track with the plane of the telescope dish, called *impact parameter*. As seen in Fig. 2.5 a shower image induced by a gamma ray shows an elongated, roughly elliptical shape. The major image axis of the ellipse points towards the shower direction on the one side and to the impact parameter on the other side. The width of the image, which is measured along the minor axis, originates from the lateral spread of the shower.

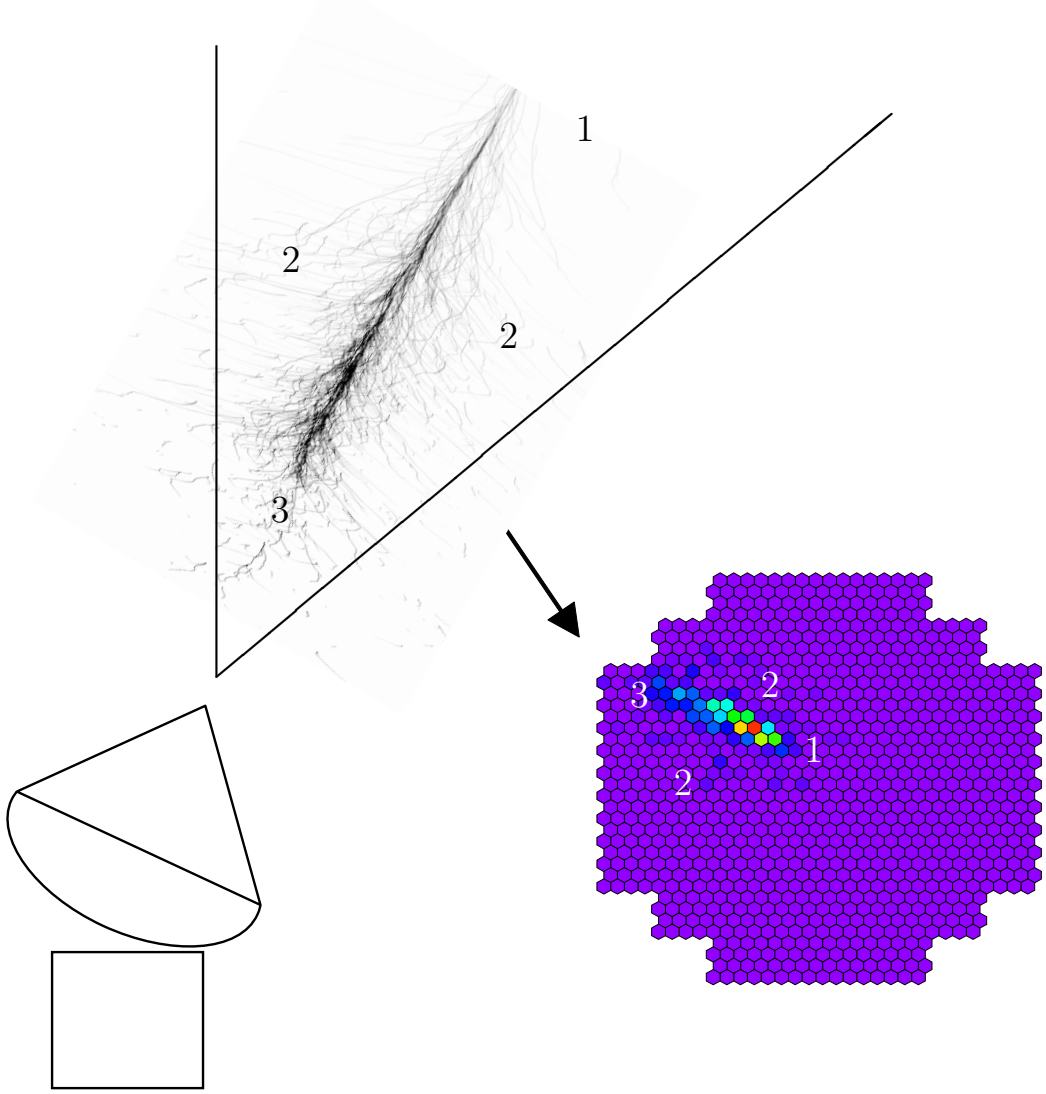

Figure 2.5.: Sketch of the basic geometry of an IACT event. In general the air shower is not on the optical axis of the telescope, but parallel to it. The Cherenkov light is collected from a reflector and a spatial intensity distribution is recorded by a camera. The camera image is elliptical, where the major axis connects the shower direction and the impact parameter.

The images can be very easily parameterised by a simple moment analysis of the ellipse

[19, 20]. These parameters are generally referred to as *Hillas parameters*. Another approach for reconstructing the shower geometry is using the full image information, where the shower parameters are directly fitted to the amplitudes measured in the individual pixels [21, 22]. In the following only the Hillas parameters are discussed in more detail. Due to the setup of the trigger an event is always seen by at least two telescopes, which allows for stereoscopic reconstruction.

Hillas Parameters

A sketch of the Hillas parameters can be seen in Fig. 2.6. They can be divided in orientation and shape parameters. The orientation parameters are used to geometrically reconstruct the shower direction and impact parameter. They are given by the distance between the centre of the camera and the centre of gravity of the shower image, simply called *distance*, and the orientation ϑ, which measures the angle between the major axis of the image and the line corresponding to the distance.

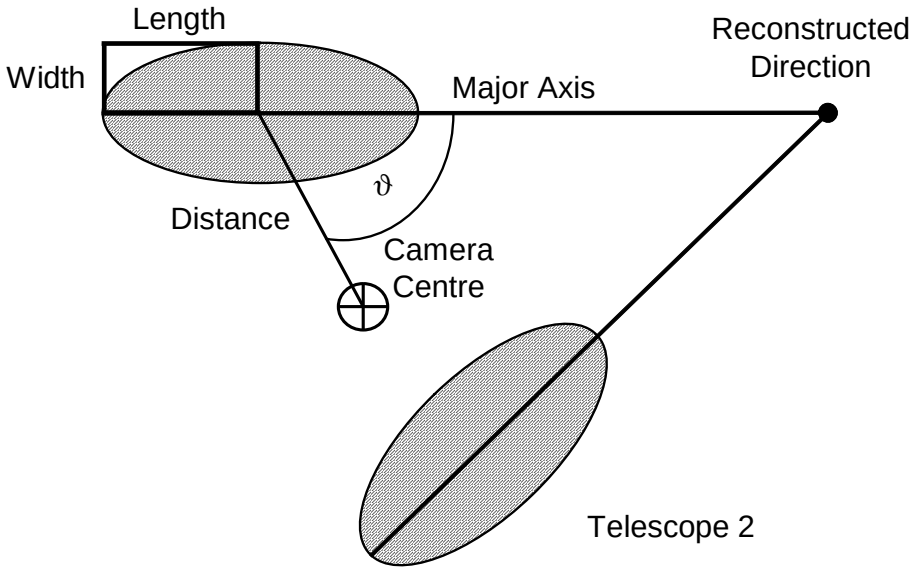

Figure 2.6.: Sketch showing the Hillas parameters for a shower seen by two telescopes.

The advantage of having more than one Cherenkov telescope seeing the same shower was already discussed with respect to the suppression of the NSB. The reconstruction also profits because the images can be superimposed. The intersection of the major axes then yields the shower direction.

In case the image is seen by more than two telescopes, the reconstruction of the shower parameters is even more improved because the shower geometry is overconstrained. There are various algorithms that can be used for stereoscopic reconstruction [23]. The accuracy of the reconstructed shower direction depends on the number of telescopes seeing the same event and the brightness, but for two telescopes it is typically already better than $\sim 0.1°$.

The important shape parameters are *length*, which gives the spread of light along the major axis, *width*, which is a similar measure along the minor axis and *size*, which measures the brightness of the image in number of photoelectrons. Length and width carry

information about the longitudinal and lateral development of the shower. The combination with the centre of gravity of the shower image provides information about the shower maximum. The size is influenced by the energy of the primary particle, the impact parameter and the zenith angle of the observation.

2.4.5. Gamma Hadron Separation

As discussed in Sec. 2.2, the hadronic cosmic rays are the most important background that needs to be reduced. The longitudinal and lateral development of hadronic and electromagnetic showers are very different due to differences in the interaction processes. This information is carried in the length and width of the shower images. Thus they provide a possibility to discriminate between the two shower types, e.g. by imposing certain selection cuts on the image parameters.

Due to the limited size of the camera, showers at the edge of the field of view can be clipped. This means that their Hillas parameters do not characterise the shower accurately and e.g. a gamma-ray shower at the edge might look like a hadron induced shower in the middle of the camera. Thus the radial acceptance of gamma-ray and background events is not constant, but drops of towards the edge of the camera. However, from this argument one expects that the acceptance of the camera should be radially symmetric.

Pre-Selection Cuts

H.E.S.S. applies a first set of cuts (pre-selection cuts) called *size* and *distance cut*. Events with a low number of photoelectrons (corresponding to a low size value) are rejected. For faint showers the Hillas parameters are only very ill-defined. Furthermore, events that have a large distance to the camera centre are also rejected, since the signal acceptance drops of towards the edge of the camera.

Selection Cuts

The cuts for gamma hadron separation are based on the mean scaled width (w_{scaled}) and length (l_{scaled}). From Monte Carlo simulations mean values $\langle l \rangle$ and $\langle w \rangle$ are calculated for gamma rays and background. A lookup table is created to predict $\langle l \rangle$ and $\langle w \rangle$ as a function of the reconstructed image amplitude and impact parameter. The image amplitude and reconstructed impact parameter from actual showers are used to calculate:

$$l_{\mathrm{scaled}} = \frac{l - \langle l \rangle}{\sigma_l} \quad \text{and} \quad \mathrm{w}_{\mathrm{scaled}} = \frac{\mathrm{w} - \langle \mathrm{w} \rangle}{\sigma_{\mathrm{w}}}, \tag{2.5}$$

where l and w are the length and width of the actual shower and σ the scatter of the corresponding mean value. The *mean reduced scaled length* (MRSL) and *mean reduced scaled width* (MRSW) are obtained by averaging the corresponding quantities over all telescopes participating in the event.

Optimised Cuts

The cuts are applied to the image size, the image distance, MRSL and MRSW. The optimum set of cuts to achieve the best signal to noise ratio depends on the spectrum

of the gamma-ray source. H.E.S.S. has three different kind of analysis cuts and the corresponding values can be found in Table 2.1. The so-called *standard cuts* are optimised for a point source with a flux of 10% of the Crab nebula and a spectrum with a power-law with a similar spectral index of $\Gamma = 2.39$. *Hard cuts* are optimised for a source with a flux of 1% of the Crab flux and $\Gamma = 2.0$. They have an improved sensitivity for weak sources with a hard spectrum by improving the signal to noise ratio with a hard cut on the background. The higher intensity cut selects better reconstructed events at the expense of a higher energy threshold. *Loose cuts* are optimised for a source with a Crab like flux and $\Gamma = 3.0$. The lower intensity cut reduces the energy threshold at the expense of a higher background acceptance.

Instead of simple one dimensional cuts the background rejection can also be done using a multivariant cut on the Hillas parameters [24]. Such a cut variable can for example be obtained from boosted decision trees. A multivariant cut typically yields a better background suppression than one dimensional cuts and therefore a better signal to noise ratio.

2.4.6. Background Estimation

Even after analysis cuts one is typically not left with a background free sample, but with a certain number of gamma-ray candidates (N_{on}) in the signal region around the source position (the so-called *on-region*). These events contain signal (N_{Sig}) and background events (N_{BG}).

Significance

One of the main question for a source discovery is how significant N_{Sig} is compared to N_{BG}. The underlying questions is: what is the probability that the observed number of signal events is merely caused by a fluctuation of the background?

Unfortunately N_{Sig} and N_{BG} cannot be extracted directly from N_{on}. The solution is to compare N_{on} to an expected number of background events (N_{off}). In general the background estimate N_{off} can have a normalisation factor α, e.g. if the region of background extraction is larger than the region for N_{on}. This means that $N_{\mathrm{BG}} = \alpha N_{\mathrm{off}}$. The best estimate for the number of signal events is called N_{excess} and is given by:

$$N_{\mathrm{excess}} = N_{\mathrm{on}} - \alpha N_{\mathrm{off}} \tag{2.6}$$

It has been shown with the help of a likelihood ratio method that the significance σ of N_{excess} compared to the background is best estimated with the Li & Ma formula [25]:

$$\sigma = \sqrt{2\left(N_{\mathrm{on}} \ln\left(\frac{1+\alpha}{\alpha}\left(\frac{N_{\mathrm{on}}}{N_{\mathrm{on}}+N_{\mathrm{off}}}\right)\right) + N_{\mathrm{off}} \ln\left((1+\alpha)\left(\frac{N_{\mathrm{on}}}{N_{\mathrm{on}}+N_{\mathrm{off}}}\right)\right)\right)} \tag{2.7}$$

It is applicable for α between 0.1-10, $N_{\mathrm{on}} > 10$ and $N_{\mathrm{off}} > 10$.

Due to inaccuracies in the reconstruction, the arrival directions of events from a point source are smeared out in a distribution, typically referred to as *point spread function* (PSF). The optimal size of the on-region is the one that maximises the signal to noise ratio and thereby the significance. Since the PSF depends on the analysis cuts the optimal

size of the on-region is also adapted for each of the H.E.S.S. analysis cuts. It is commonly expressed in units of θ^2, where θ is the distance from the reconstructed shower position to the centre of the on-region. The values can also be found in Table 2.1.

Type	Size [p.e.]	Distance [°]	MRSL Min.	MRSL Max.	MRSW Min.	MRSW Max.	θ^2_{cut} [degress^2]
Standard	80	2.0	-2.0	2.0	-2.0	0.9	0.0125
Hard	200	2.0	-2.0	2.0	-2.0	0.7	0.01
Loose	40	2.0	-2.0	2.0	-2.0	1.2	0.04

Table 2.1.: The analysis cuts used in the H.E.S.S. standard data analysis for the different types of sources scenarios as described in the text. The definition of the cut values is given in the text as well.

Estimating N_{off} is challenging because it depends on the current energy threshold (which in turn depends on the zenith angle, the atmosphere and the optical performance of the telescope), the current NSB and the acceptance, which depends on the position of the signal region in the camera. Three common ways to estimate the background are now described [26].

On/Off

The first Cherenkov telescopes used On/Off observations, where observations of the on-region are mixed with observations of same duration of an empty field at equal zenith angles. It is then assumed that the background is equal in the two data sets and thus a simple difference of the two field of views provides a measurement of N_{excess}. The advantage of this technique is that the significance for the whole camera can be calculated without further input, which allows to easily create excess and significance sky maps of the whole region seen by the camera. A major drawback of this technique is the fact that the source region is observed only half of the time.

Reflected-Region Background

The problem of the On/Off method can be avoided by observing the source region in so-called *wobble* mode [27]. The observation position is displaced from the centre of the camera to allow source observation and background estimation from the same camera field of view. It is important that the wobble offset is large enough so the camera centre does not overlap with the on-region.

The reflected-region background method is only applicable for wobble observations and exploits the fact that the background acceptance of the camera is to first order radially symmetric. The regions for background estimation (*off-regions*) are obtained by rotating the on-region around the observation position (see Fig. 2.7). They should not overlap and have some distance to the on-region to avoid contamination from misreconstructed events. Off-regions feature the same size and offset to the camera centre as the on-region, which means that the off-events are taken at the same time and with the same background acceptance as the on-events. If other gamma-ray sources are in the field of view, some region around them has to be excluded for the placement of off-regions. The normalisation factor α in Eq. 2.6 accounts for the different number of on- and off-regions.

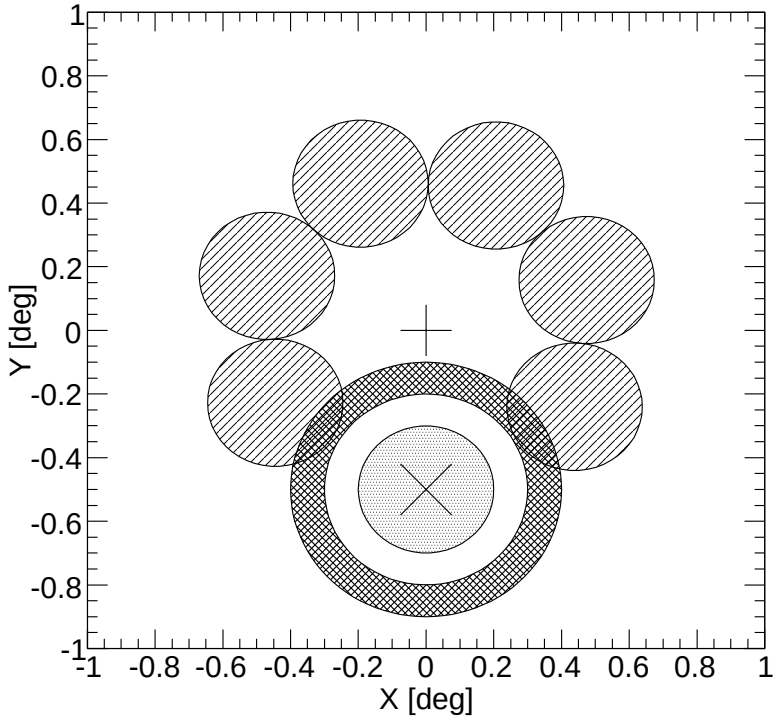

Figure 2.7.: Sketch showing two methods for background modelling described in the text. The observation position of the telescope is marked by a plus, while the target position is marked by an X. Both are displaced from each other by the wobble offset. The x- and y-axis show the cartesian camera coordinates expressed as angular difference. The on-region surrounds the target position and is indicated by the dotted area. The off-regions for the reflected-region background method are given by the striped areas. For the ring background method the off-region is given by the hatched ring.

In order to avoid systematic effects if the acceptance is not radially symmetric, the wobble position is altered around the target position between different observations. The reflected background is best suited for spectral analysis because the acceptance is typically energy dependent and this effect cancels out. In principle the on-region can have an arbitrary shape, but in most cases circular regions are used that are suited for point sources.

Ring Background

The ring background method can be applied to any position within the field of view. A ring is created around the test region (on-region) with some distance between the inner ring radius and the on-region from which N_{off} is derived (in Fig. 2.7 the ring is constructed for a test region which is put on the target position). Regions with known gamma-ray sources have to be excluded from the area of the ring. By using a model for the background acceptance and accounting for the different areas of ring and on-region the normalisation factor α can be calculated.

The advantage of this method is that it provides the background for the whole field of view and thus allows the determination of excess and significance sky maps. A downside is the dependence on the modelling of the background acceptance. It is derived empirically by using data sets without known gamma-ray sources. Since the background acceptance is typically energy dependent the ring background is less suited for spectral analysis.

2.4.7. Flux Determination and Limits

The basic ingredient to reconstruct the energy of an event is the intensity of the image, which is e.g. given by the size parameter from the Hillas parametrisation. The amount of Cherenkov photons measured on the ground is roughly proportional to the number of charged particles in the shower, which in turn allows to estimate the energy of the primary particle. However, the measured intensity also depends on the impact parameter, because the shower is considerable dimmer if the telescope is no longer inside the central $\sim 100\,\mathrm{m}$ radius around the shower axis. Furthermore, it depends on the zenith angle of the observation because the Cherenkov light has to transverse more atmosphere for larger zenith angles and hence suffers more absorption. The latter also causes the energy threshold of the instrument to be zenith angle dependent.

After the shower is reconstructed a lookup table is used to get the best estimate for the energy. Typical energy resolutions, which are defined as $(E_{\mathrm{reco}} - E_{\mathrm{true}})/E_{\mathrm{true}}$, where E_{reco} and E_{true} are the reconstructed and the simulated energy respectively, that can be achieved are $\mathcal{O}(15\%)$.

There are some more effects that make the energy reconstruction difficult. The atmospheric extinction can change e.g. due to clouds or dust and thus the transmissivity is different. Hence, spectral analysis is typically limited to data taken in clear nights. Furthermore, the response of the optical system can change over time. One way to estimate this is to look at the Cherenkov light emitted by single muons whose light yield can be estimated from geometrical arguments [28]. These are typically events that pass close to the telescope. The decreasing optical performance of the telescopes can be monitored and a correction factor, called *muon correction*, is multiplied with the reconstructed energy.

Flux Upper Limits

In case of a non-detection of a source it is interesting to find the limit on the assumed source spectrum that is still compatible with the non-detection. This needs the specification of a confidence level. For example, an upper limit at a confidence level of 90% means that the probability that the actual flux is higher than the given upper limit is 10%, but remained undetected. In the H.E.S.S. analysis upper limits on the number of excess events (N_{UL}) are calculated using the method of Rolke et al. [29].

For a given source spectrum $S(E)$ the number of expected excess events (N_{exp}) is given by:

$$N_{\mathrm{exp}} = \int_{E_{\mathrm{min}}}^{\infty} dE \int_{0}^{T} dt S(E) A_{\mathrm{eff}}(E,T) \ , \tag{2.8}$$

where T is the deadtime corrected livetime of the used observations and $A_{\mathrm{eff}}(E,T)$ the effective gamma-ray collection area. The later one is time-dependent, because the data set

typically contains several observations at different zenith angles and thus different energy thresholds and effective areas. The gamma-ray effective area contains a contribution from an energy-dependent gamma-ray selection efficiency and the gamma-ray detection probability. Thus it does not only depend on the experiment and observation conditions (like zenith angle), but also on the cuts used for gamma hadron separation. The effective areas are determined from Monte Carlo simulations. If combining several observations, N_{exp} is evaluated for each of them separately. The flux upper limit F_{UL} is then obtained by integrating the normalised source spectrum ($S_N(E)$) for which $N_{\mathrm{exp}} = N_{\mathrm{UL}}$:

$$F_{\mathrm{UL}}(> E_{\mathrm{min}}) = \int_{E_{\mathrm{min}}}^{\infty} S_N(E) dE \ . \tag{2.9}$$

For the upper limit determination a further cut is applied to the events. The energy threshold above which events are used for spectral analysis (E_{min}) is defined as the higher value of:

1. the peak of the expected differential count rate versus energy, which is obtained by multiplying the H.E.S.S. effective areas with the expected source spectrum,

2. the energy where the energy bias becomes less than 10%.

This approach reduces systematic uncertainties originating from the estimation of the effective areas. H.E.S.S. can still detect gamma rays with energies below this threshold and all events are used when the significance of a gamma-ray excess is estimated.

Chapter 3

H.E.S.S. Pointing Corrections

As discussed in Chapter 2, the accuracy of the reconstructed shower direction for a single gamma-ray event is typically about $\sim 0.1\,^{\circ}$. However, for a huge number of events the centre of gravity of their distribution can be determined much more accurately. The position of a bright source reaches a statistical accuracy of better than $10\,''$. It is shown in the current chapter that systematic errors on the telescope pointing, which is the ability to relate the measured images in the Cherenkov camera to the origin in the sky, are much larger than this and therefore this "mis-pointing" needs to be corrected. In the first section astrometric corrections are introduced in general and mechanical reasons for mis-pointing of the H.E.S.S. telescopes are discussed. H.E.S.S. uses two methods to correct for the mis-pointing, which are discussed in the next two sections. In the H.E.S.S. standard approach (Sec. 3.2) a model is created, which predicts the mis-pointing for different observation positions. To further reduce the systematic uncertainties additional pointing corrections can be calculated simultaneously to the data taking (precision pointing, Sec. 3.3). The last section discusses a necessary replacement of the pointing hardware that was conducted during this thesis. This requires a calibration of the new hardware, which is additionally described.

3.1. Introduction

This section starts with a short introduction to the idea of astrometric corrections. Then known astronomical corrections when transforming coordinates from the sky to the ground are briefly discussed. Mechanical effects for the H.E.S.S. telescope mis-pointing are illustrated in the last subsection.

3.1.1. Astrometry

Any kind of astronomical observation receives its meaning from the accurate relation between the image and the origin in the sky. In optical astronomy this "pointing problem" is known by the name of *astrometry*. This branch of astronomy deals with precise measurements of the positions of stars and other celestial objects. If one has a set of accurately known star positions, one can use them as reference points on the sky, e.g. to describe the position of new objects in the sky or to track movements of objects. Using relative positioning allows even amateur astronomers with simple telescopes to achieve an arcsecond resolution. Astrometry is therefore also closely linked to the creation of star catalogues.

For IACTs it is not possible to base the telescope pointing on strong reference sources, because the number of sources is only of the order of 100. This makes it very unlikely that more than one source falls in the same field of view. Therefore the telescope mis-pointing, which is the deviation from the actual to the nominal or expected observation position on the sky, must be corrected for each observation separately. It can amount to several arcminutes and it is desirable to reduce this systematic error to the same or an even lower level than the statistical error. Furthermore, multi-wavelength data (e.g. optical, X-ray or radio) typically have a much better angular resolution. The interpretation of source models and physics can therefore benefit immensely if the source positions provided by the IACTs are as accurately as possible.

The mis-pointing needs to be modelled or measured for each telescope separately. Due to the large field of view of IACTs and the fact that gamma rays are recorded on an event-by-event basis it is not necessary to apply pointing corrections online. They can be calculated offline and may be replaced later e.g. in case that better corrections are found that further reduce systematic effects.

3.1.2. Astronomical Corrections

Pointing corrections include two steps well known from other ground based observations, namely the transformation from celestial to ground based coordinates and corrections due to atmospheric refraction. They are briefly discussed here for completeness and more information can be found in the specified references.

Astronomical Coordinate Transformations

The sky presents itself as a two dimensional projection of positions onto the celestial sphere. A widely-used system to map celestial objects is the equatorial coordinate system. It uses two spherical coordinates that are perpendicular to each other and the projection of the Earth equator onto the celestial sphere serves as the reference plane. The right ascension ranges from 0 ° to 360 ° and describes the orientation on the reference plane, and the declination, which ranges from -90 ° to +90 °, marks the distance to the reference plane. Coordinates in this system do not depend on the latitude and longitude of the observer or, to first order, the time of the observation. To second order certain effects change the position of objects. A well known effect is the parallax motion of stars against a distant background due to the rotation of the Earth around the Sun. Other effects are precession and nutation of the Earth's rotational axis. Thus equatorial coordinates are typically reported for a fixed point in time, called epoch. The current epoch is called J2000.0, which corresponds to 2000 January 1 11:58:55.816 UTC.

For ground based telescopes another coordinate system is used that describes the sky as it is currently visible above the observer. The horizontal coordinate system uses the observer's local horizon as reference plane and replaces the right ascension and declination angle with azimuth and altitude. The altitude of +90 ° is called zenith, so the altitude is often expressed as zenith angle (i.e. 90 °-altitude).

In H.E.S.S. two types of horizontal coordinate systems are used, the *AltAzSystem* and the *HorizonSystem*. The difference between the two systems is the application of a correction for atmospheric refraction (see below). The implementation of the H.E.S.S. coordinate systems is described in greater detail by Gillessen [30].

Atmospheric Refraction

Celestial objects close to the horizon appear higher than they actually are. The reason for this is that the electromagnetic radiation has to pass through the atmosphere on a path with variations in air density, which deflects it from a straight line. Atmospheric refraction gets stronger for lower altitudes and is of the order of $10'$ for an altitude of $5°$. The refraction is wavelength dependent and it changes with the conditions of the atmosphere, like temperature, pressure and humidity.

Two effects for H.E.S.S. are worth mentioning. Stars are typically detected by CCD cameras, which are primarily sensitive to red light. Cherenkov light on the ground, however, is peaked in the blue as is the typical quantum efficiency of the used photomultipliers. Due to the different wavelengths, the observed refraction for stars (650 nm) and Cherenkov showers (450 nm) is slightly different. Furthermore, the Cherenkov light traverses only the lower part of the atmosphere, which is why the refraction is lower than for star light. This is taken into account with a reduction factor.

Further details on the implementation of the atmospheric refraction correction and the reduction factor can be found elsewhere [31]. Figure 3.1 shows the refraction for star light and the H.E.S.S. standard atmosphere and the relative influence of various parameters. H.E.S.S. has a weather station on site that measures the atmospheric conditions at ground level. It can provide a very rough knowledge of atmospheric parameters, but the resulting uncertainty in the correction can still exceed $30''$ for low altitudes. Therefore the H.E.S.S. standard pointing is restricted to an altitude of above $25°$. The measured atmospheric conditions are used when evaluating the results of the pointing runs (more details in Sec. 3.2). However, since the influence is small, only a correction for the standard atmosphere is applied during data analysis. Precision pointing is limited to altitudes above $45°$ to make uncertainties in the refraction smaller than $5''$ and the actual data from the weather station is used also during data analysis.

3.1.3. Mechanical Reasons for Mis-Pointing

The following list contains examples for mechanical effects that lead to mis-pointing of the telescopes:

- tracking offsets,
- tracking non-linearities,
- non-vertical alignment of the azimuth axis,
- offsets and rotation of Cherenkov camera,
- non-perpendicular alignment between the azimuth and the altitude axes,
- bending of telescope components.

The main idea of the telescope mechanical model used in the H.E.S.S. standard pointing is to mimic these effects as well as possible and all effects are explained in more detail when the mechanical model is introduced in Sec. 3.2.2. As an introduction the influence of some of these parameters is demonstrated here. Figure 3.2 shows how the position of

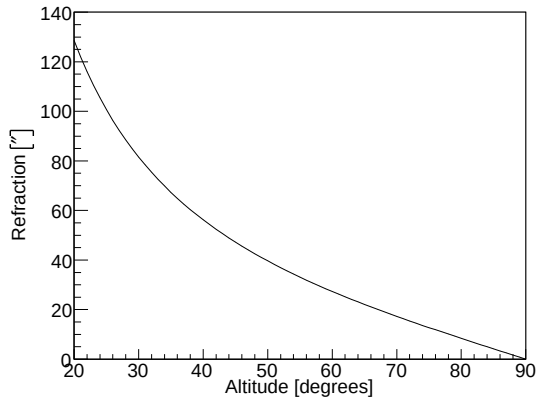

(a) Refraction for the H.E.S.S. standard atmosphere (10% relative humidity, 1023 mbar (sea level) pressure and 10 °C) as a function of altitude.

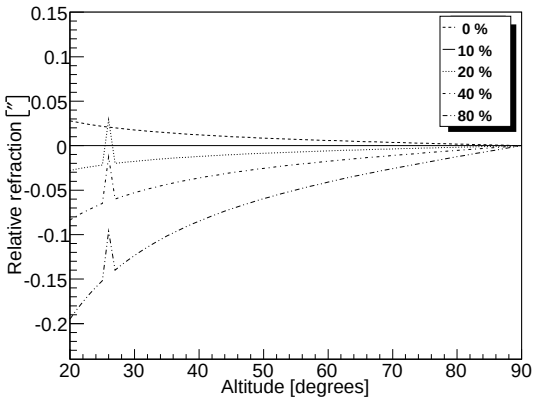

(b) The influence of varying the relative humidity relative to the values for the standard atmosphere. There seems to be some numerical problem, but the effect is so small that it is negligible.

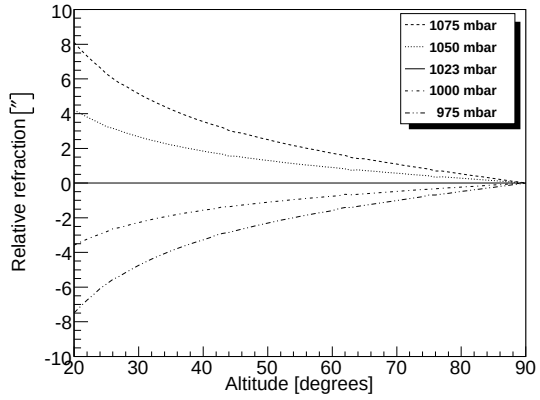

(c) The influence of varying the (sea level) pressure relative to the values for the standard atmosphere.

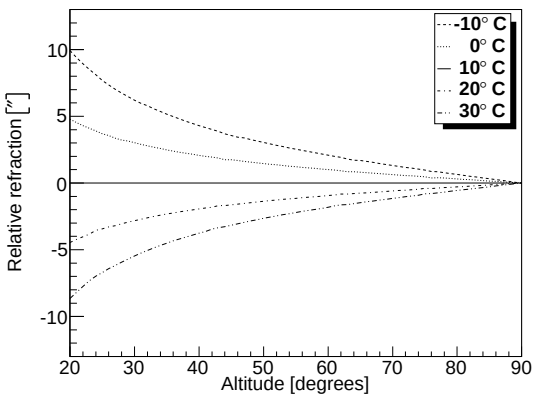

(d) The influence of varying the temperature relative to the values for the standard atmosphere.

Figure 3.1.: Refraction for star light (650 nm) and the influence of various parameters on the resulting correction.

the Cherenkov camera centre changes as a function of altitude. The dominant effect here is the gravitational pull on the Cherenkov camera, which is indicated by the good fit to a cosine function. As discussed in Sec. 2.3 the camera has a weight of about 800 kg, which leads to significant mast bending with decreasing altitude.

The displacement of the telescope optical axis with respect to the sky is measured in Fig. 3.3 as a function of azimuth. Here the dominant effect is the non-vertical alignment of the azimuth axis, which explains the sinusoidal behaviour. For CT3 the tilt in the axis is of the order of 1 cm, which has to be compared to the rail diameter of $\sim$ 15 m. The spread in the curve, which is much larger than the one in Fig. 3.2, shows that also other effects, e.g. the non-perpendicular alignment between the azimuth and the altitude axes, are important.

The two effects demonstrated here already amount to mis-pointing corrections of the order of several arcminutes and the residuals are still larger than the statistical error for

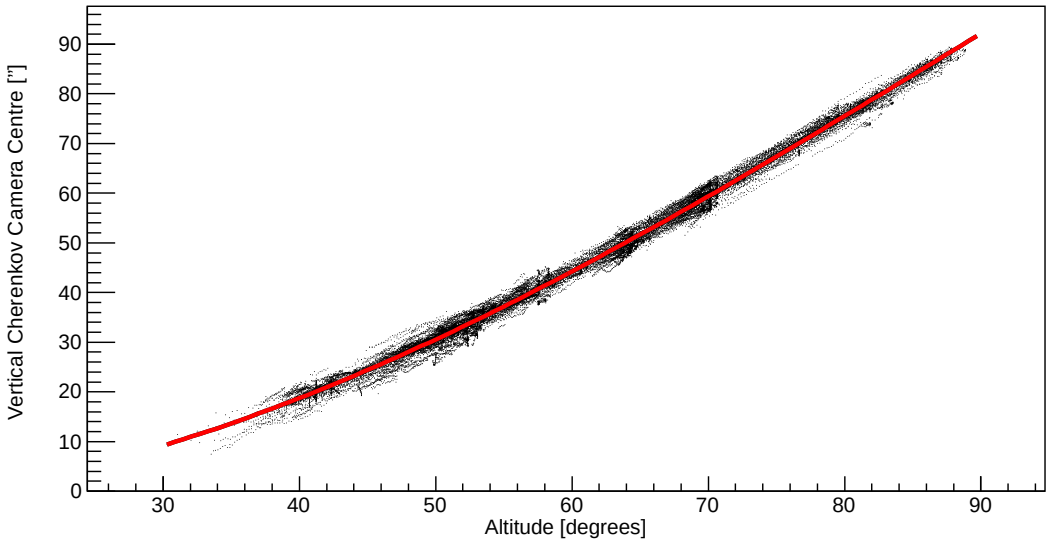

Figure 3.2.: Position of the Cherenkov camera centre for CT4 (runs 55000-60000) as a function of altitude with an arbitrary offset subtracted. Each point corresponds to the determination of the camera centre, obtained by fitting the eight positioning LEDs on the camera (the method is introduced in detail in Sec. 3.2.1). The shift is well described by a cosine function of the form $y = y_0 + A\cos\alpha$, where α is the altitude. A fit to the data (red line) yields $A = (-95.9 \pm 0.04)''$ (giving each point an equal weight in the fit).

bright sources. Therefore, a sophisticated approach to the correction of the mis-pointing of the H.E.S.S. telescopes is now discussed.

3.2. Standard Pointing

The main idea of the H.E.S.S. standard pointing is to create a model that is capable of predicting the mis-pointing for all possible telescope orientations. Measurements of the telescope mis-pointing can be made in special calibration runs, where the telescope is pointed at bright stars and the Cherenkov camera lid is closed. The star gets imaged by the telescope mirrors onto the lid and the desired correction is the difference between the centroid of the star image and the centre of the Cherenkov camera. More details on these special calibration runs, called *pointing runs*, and on the data reduction can be found in Sec. 3.2.1. With 20-40 measurements covering different positions in the sky it is possible to disentangle the different mechanical contributions to the mis-pointing. The pointing runs are used to create a mechanical model which is introduced in the next subsection. In the last subsections an example of a pointing model is shown and the remaining systematic uncertainties are briefly discussed.

3.2.1. Data Collection

Here the different steps from the hardware measurement to the calculation of a telescope mis-pointing are presented.

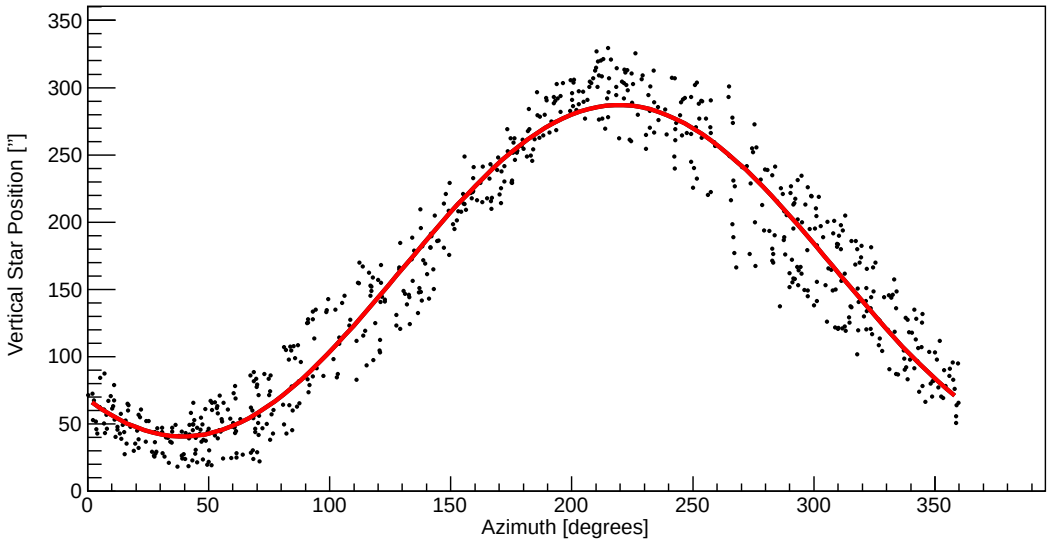

Figure 3.3.: Position of a star projected onto the Cherenkov camera for CT3 (runs 40000-65000) as a function of azimuth with an arbitrary offset subtracted. In contrast to Fig. 3.2 the data were obtained only from pointing runs (introduced in Sec. 3.2.1). To guide the eye the data are fitted using a sine function (red line, giving each point an equal weight in the fit). No correction for refraction was applied, therefore only stars above 70 ° altitude are used in the plot.

Hardware

In order to measure the difference between the centroid of the star image and the Cherenkov camera centre an optical CCD camera is installed in the centre of each telescope dish, which is called the *LidCCD*. The LidCCD is in a steel housing that supports the optical lens. It is mounted onto a plate, which is firmly attached to the dish to prevent any movement of the CCD. The first generation of LidCCD is an Apogee Ap2Ep with a KAF-1600E chip featuring 1536x1024 pixels. It is readout over a 45 m parallel port cable. The readout is very slow and takes approximately one minute for a full frame image to complete. Until late 2004 a 180 mm lens was used on the telescope and then replaced with a 135 mm one (Nikon Nikkor). The smaller focal length yields a larger field of view at the cost of a lower resolution. With the new lens the complete Cherenkov camera with all eight reference LEDs (see Fig. 2.4) is visible, compared to the old optics where only three of the LEDs were visible. The idea behind the higher resolution in the first place was that it might be an advantage for the initial mirror alignment of the telescope. However, recently the mirrors of the H.E.S.S. telescopes have been refurbished and mirror alignment was done with the new optics without problems. It can be therefore concluded, that the new optics are better suited because the increased number of LEDs reduces systematics in the pointing corrections. The CCDs are actively cooled with the help of Peltier elements to keep them at a constant temperature of -25 ° C. This avoids thermal expansion and differences in the CCD pictures due to differences in the ambient temperature. Thermal noise of the CCD chip is not an issue. It has been shown that for an exposure time of 30 min for temperatures up to -5 °C the noise of the camera is still dominated by the readout noise

of the electronics [32] and the exposure times used in H.E.S.S. are much shorter. Thus for the replacement cameras (see Sec. 3.4) the cooling temperature was increased to -5 °C in order to spare the chip from thermal stress in case of sudden warming, e.g. due to a power failure.

Pointing Runs

During pointing runs the LidCCD takes images of bright stars tracked by the telescope and of the LEDs that determine the orientation of the Cherenkov camera. Stars are selected from the Hipparchos catalogue [33]. They should homogeneously sample the (Cartesian) azimuth-altitude plane, which also means that the same star can be used more than once at a different time during the night. For pointing runs no astronomical darkness is required, so the data can be recorded when the moon is above the horizon. They are typically done at the beginning and the end of each dark time period. Target stars are selected in such a way that the telescopes do not point at the moon and that the distance between the moon and the target star is always smaller than 177 ° to prevent direct light from behind the mirrors onto the camera lid.

Due to a large difference in brightness, different exposure times are needed for the stars and LEDs. Therefore in each pointing run two images are recorded immediately after each other. The exposure time t for the image of a star with apparent magnitude m is calculated by $t = t_S \cdot 2.512^{m-m_S}$, where $m_S = -1.46$ and $t_S = 0.7$ s are reference values measured for Sirius. Only stars brighter than magnitude 3 are targeted during pointing runs, leading to a maximum exposure time of roughly 40 s. The second image has a fixed exposure time of 0.5 s. The brightness of the LEDs is adjusted in such a way that the maximum of the spot in the image is approximately one third of the maximum count rate ($\sim 20,000$ counts for 16 bit resolution).

Data Reduction

A list of spots with the LEDs and the star has to be extracted from the LidCCD images. This is done in a two-step procedure using tools provided by the eclipse library of ESO [34]. In the first step the eclipse function *find_obj* is used, where the image smoothing with the 5×5 flat kernel has been replaced by a 3×3 median filter. Then a so-called kappa-sigma clipping is applied, which means that a binary image is created with the threshold at the mean image pixel value plus two standard deviations. The mean is estimated by the median and the standard deviation by the mean distance to this median value. A morphological binary closing (performing an erosion and a dilatation) with a 3×3 kernel is performed so structures smaller than this kernel disappear. On each remaining zone eclipse standard statistical measurements are performed to determine the spot centre of gravity, size and brightness.

The second step should provide a more accurate spot extraction. To this end sub-frames of 20×20 pixels are created around each object. After applying the median filter a segmentation method is run that was designed to deal with non-constant backgrounds. All pixels below the determined background level, the frame borders and pixels further away than four times the current estimate for the spot size are set to zero. Finally, the spot characteristics are calculated with the remaining pixels.

More details on the spot extraction can be found elsewhere [32, 35, 36]. It has been shown elsewhere [32] that the H.E.S.S. spot extraction algorithm returns inconsistent values for the spot brightness and the spot size. The reason for this appears to be a wrongly estimated background level during the image segmentation in the second step. However, it does not appear to influence the accuracy of the determination of the centre of gravity [36], which is the only thing that is needed accurately. In later studies, where the spot size is of importance, a different algorithm is used (described in [32]).

Fit of Camera Centre

The spots identified in the LED exposure are fitted to the design position of the LEDs by using the following transformation:

$$\begin{aligned} x_{\text{Spot}} &= S \cdot (x_{\text{Design}} \cdot \cos\theta - y_{\text{Design}} \cdot \sin\theta) + \Delta_x, \\ y_{\text{Spot}} &= S \cdot (x_{\text{Design}} \cdot \sin\theta + y_{\text{Design}} \cdot \cos\theta) + \Delta_y. \end{aligned} \tag{3.1}$$

S is the scale between pixel numbers in the LidCCD and metre on the lid, thus providing an effective focal length for the optics. The angle θ can be used to measure the rotation of the Cherenkov camera, while Δ_x and Δ_y provide the offset to some fixed reference point. It does not matter what that reference point is, as long as the star positions are measured against the same one. Only the difference is important for the pointing correction. All parameters are passed to a Minuit [37] based fitting algorithm that tries to minimise the summed square distances between the spots and the design positions.

The optical axis of the LidCCD is pointing at the centre of the Cherenkov camera, so all LEDs have about the same distance from the optical axis. Systematic effects like e.g. optical aberrations would thus cancel out. This cancelling only works if the same number of LEDs is fitted on each side of the camera. The effect of the number of LEDs onto the fit result has been investigated elsewhere [31]. It is $< 4''$ for seven LEDs, but can reach more than $20''$ for three LEDs.

Due to software problems, leading to occasional wrong fit results, the LED fit was newly implemented. At the same time a cut was introduced to remove spots with a maximum at the maximum count rate (2^{16}-1 for 16 bit resolution). If a CCD pixel reaches the maximum charge it can hold the excessive charge starts to leak into neighbouring pixels. This effect is known as *blooming*. The leakage is stronger in the readout direction of the CCD, thus converting the spots into lines. This leads to a wrong determination of the centre of gravity and therefore to bad fits of the camera centre.

3.2.2. Mechanical Model

The idea of modelling mis-pointings of an IACT was pioneered by the HEGRA collaboration [38, 39]. They used a mechanical model with 11 parameters for each telescope, which reduced the systematic pointing error after correction to about $25''$ [40]. Instead of an optical CCD the star spot was found by a time-consuming raster scan using the central pixel of the camera.

The H.E.S.S. mechanical model is almost identical to the one used by the HEGRA collaboration and was introduced by Gillessen [30]. In this subsection the mechanical model as it is currently implemented for the H.E.S.S. telescopes is discussed. The order of the discussion follows the order in which each of the effects is applied in the software.

Tracking Correction

The H.E.S.S. tracking system measures the nominal tracking position in azimuth (az_{SE}) and altitude (alt_{SE}) by means of shaft encoders (SE). They can measure the tracking relative to an absolute tracking direction very precisely. This absolute tracking direction needs to be calibrated and a wrong calibration would lead to a constant offset $\vec{c}_{\mathrm{SE}}$ compared to the true direction in azimuth and altitude. Furthermore, the shaft encoders can have non-linearities, which leads to a systematic error in the measured values. This effect can be parameterised by a sine function in each direction with an amplitude A_{SE} and a phase ϕ_{SE}. In total this gives six different parameters. The position corrected by tracking (tc) is therefore given by:

$$\begin{pmatrix} az_{\mathrm{tc}} \\ alt_{\mathrm{tc}} \end{pmatrix} = \begin{pmatrix} az_{\mathrm{SE}} \\ alt_{\mathrm{SE}} \end{pmatrix} + \vec{c}_{\mathrm{SE}} + \begin{pmatrix} A_{\mathrm{SE,az}} \cdot \sin(az_{\mathrm{SE}} + \phi_{\mathrm{SE,az}}) \\ A_{\mathrm{SE,alt}} \cdot \sin(alt_{\mathrm{SE}} + \phi_{\mathrm{SE,alt}}) \end{pmatrix}. \tag{3.2}$$

Non-vertical Azimuth Axis

The non-vertical alignment of the azimuth axis can be expressed as a two dimensional rotation λ and β. β describes the amplitude of the axis tilt and λ the direction of the maximum tilt. The calculations are best done in cartesian coordinates, where the tracking corrected position is given by:

$$\begin{pmatrix} x_{\mathrm{tc}} \\ y_{\mathrm{tc}} \\ z_{\mathrm{tc}} \end{pmatrix} = \begin{pmatrix} \cos alt_{\mathrm{tc}} \cos az_{\mathrm{tc}} \\ \cos alt_{\mathrm{tc}} \sin az_{\mathrm{tc}} \\ \sin alt_{\mathrm{tc}} \end{pmatrix}. \tag{3.3}$$

The two dimensional rotation then gives:

$$\begin{aligned} x_{\mathrm{true}} &= x_{\mathrm{tc}} \left(\cos^2\lambda + \sin^2\lambda \cos\beta\right) &&+ y_{\mathrm{tc}} \left(\sin\lambda\cos\lambda(1-\cos\beta)\right) &&- z_{\mathrm{tc}} \left(\sin\lambda\sin\beta\right), \\ y_{\mathrm{true}} &= x_{\mathrm{tc}} \left(\sin\lambda\cos\lambda(1-\cos\beta)\right) &&+ y_{\mathrm{tc}} \left(\sin^2\lambda + \cos^2\lambda\cos\beta\right) &&+ z_{\mathrm{tc}} \left(\cos\lambda\sin\beta\right), \\ z_{\mathrm{true}} &= x_{\mathrm{tc}} \left(\sin\lambda\sin\beta\right) &&- y_{\mathrm{tc}} \left(\cos\lambda\sin\beta\right) &&+ z_{\mathrm{tc}} \left(\cos\beta\right). \end{aligned} \tag{3.4}$$

Converting this back into altitude and azimuth results in:

$$alt_{\mathrm{true}} = \arcsin z_{\mathrm{true}}, \tag{3.5}$$

$$az_{\mathrm{true}} = \begin{cases} \arccos \frac{x_{\mathrm{true}}}{\cos alt_{\mathrm{true}}}, & y_{\mathrm{true}} \geq 0 \\ 360^\circ - \arccos \frac{x_{\mathrm{true}}}{\cos alt_{\mathrm{true}}}, & y_{\mathrm{true}} < 0 \end{cases} \tag{3.6}$$

The difference between $az_{\mathrm{SE}}/alt_{\mathrm{SE}}$ and $az_{\mathrm{true}}/alt_{\mathrm{true}}$ causes a shift $\overrightarrow{\Delta}_{\mathrm{NV}}$ between the Cherenkov camera centre relative to the nominal observation direction:

$$\overrightarrow{\Delta}_{\mathrm{NV}} = \begin{pmatrix} (az_{\mathrm{SE}} - az_{\mathrm{true}}) \cos alt_{\mathrm{true}} \\ alt_{\mathrm{SE}} - alt_{\mathrm{true}} \end{pmatrix}. \tag{3.7}$$

Global Camera Offset

A constant shift ($\overrightarrow{\Delta}_{\mathrm{GO}}$) between the centre of the Cherenkov camera and the optical axis of the telescope can originate if the mirrors are not exactly imaging the optical axis

into the centre of the Cherenkov camera. Another possibility is a misalignment during construction or an ageing of the telescope structure, which would result in a shift over timescales of years. It is not possible to disentangle the camera offset in altitude from a constant tracking offset in altitude, because only the sum can be measured. Therefore the tracking offset is fixed to zero.

Another effect is the rotation of the Cherenkov camera against the sky, which can also result from construction or during the built in of the camera. It is determined from independent measurements, by using fits of the camera centre with the LEDs (see Sec. 3.4.3).

Non-Perpendicular Axes

If the altitude axis is not exactly perpendicular to the azimuth axis this would lead to an additional shift. Let $90° - \delta$ be the angle between the two axes, then the shift can be parameterised as:

$$\overrightarrow{\Delta}_{\mathrm{NP}} = \begin{pmatrix} \arcsin(\sin\delta \sin alt_{\mathrm{true}}) \\ \arcsin(\cos\delta \sin alt_{\mathrm{true}}) \end{pmatrix}. \tag{3.8}$$

The shift in the vertical is very small and therefore neglected. In normal operation the H.E.S.S. telescope do not go into "reverse" mode, which means driving the telescope over zenith, so the camera would be upside down. This makes it difficult to disentangle δ from the tracking correction $A_{\mathrm{SE,alt}}$ and $\phi_{\mathrm{SE,alt}}$. The tracking corrections are therefore fixed to zero and only δ is fitted. This is a first difference to HEGRA, where reverse tracking was done and all parameters were fitted separately.

Bending

Bending, like it was demonstrated in Fig. 3.2, leads to an additional shift of the form:

$$\overrightarrow{\Delta}_{\mathrm{B}} = \begin{pmatrix} b_x \cos alt_{\mathrm{true}} \\ -b_y \cos alt_{\mathrm{true}} \end{pmatrix}. \tag{3.9}$$

The horizontal mast bending is neglected and fixed to zero.

Other Effects

All the terms discussed so far were also included in the HEGRA mechanical model. For H.E.S.S. it turned out that including another term which is modulated with $\sin 2az$ better reproduces the pointing data and leads to smaller residuals of the model. The correction corresponding to this effect is:

$$\overrightarrow{\Delta}_{2az} = A_{2az} \begin{pmatrix} \cos\Phi_{2az} \\ \sin\Phi_{2az} \end{pmatrix} \sin(2az_{\mathrm{true}} + \phi_{2az}), \tag{3.10}$$

where A_{2az} and ϕ_{2az} are the amplitude and phase respectively and Φ_{2az} is a mixing angle. There is no known geometrical or mechanical interpretation of this term. However, the low residuals for the H.E.S.S. telescopes show that the mechanical model is performing well.

Total Correction

The total pointing correction $\overrightarrow{\Delta}$ derived from the mechanical model is then given by:

$$\overrightarrow{\Delta} = \overrightarrow{\Delta}_{\mathrm{NV}} + \overrightarrow{\Delta}_{\mathrm{GO}} + \overrightarrow{\Delta}_{\mathrm{NP}} + \overrightarrow{\Delta}_{\mathrm{B}} + \overrightarrow{\Delta}_{2az} \tag{3.11}$$

3.2.3. Model Creation

All together the H.E.S.S. mechanical model has 17 parameters, from which 4 have been fixed to zero and one (the rotation of the Cherenkov camera against the sky) is determined from independent measurements. The remaining 12 parameters are determined by a Minuit χ^2 fit to the data from the pointing runs. The fitting is done iteratively and pointing runs where the residuals are larger than four standard deviations of a Gaussian fitted to the residuals in azimuth or altitude are discarded. Wrongly measured mis-pointings can result if the determination of the star or the camera centre is incorrect. New pointing models are typically created every two month or after hardware was changed or touched. This also allows to monitor the long-term stability of the system and to easily identify structural weaknesses. Fig. 3.4 shows an example of a pointing model that was fitted to three month of pointing data.

3.2.4. Systematic Uncertainties

The systematic uncertainties of the H.E.S.S. standard pointing have been studied in depth elsewhere [31] and here only a short summary of the findings is given. The width of a Gaussian fitted to the magnitude of the residuals between the pointing model and the measured corrections is typically of the order 4-8″ for the different telescopes and periods. However, an independent test of the pointing, where shower images from two different telescopes are compared, indicates a residual systematic error of 10-30″ [31], which is higher than what can be expected from the residuals of the model.

This discrepancy can be explained by various instrumental and methodical errors. It has been shown that for a single run and a single telescope the systematic error is of the order of 21-41″ [31]. These errors are reduced when the telescopes are combined, leading to a typical systematic error of $\sim 20''$ per axis.

3.3. Precision Pointing

In the last section the H.E.S.S. standard pointing was introduced, where the mechanical behaviour of the telescope is modelled. Pointing corrections for the data are then derived according to that model. One caveat of this approach is that the model is an average over a certain time period and the current mis-pointing can be different from the modelled one. The ideal solution would be to have pointing corrections simultaneously to the data taking, which is not possible with the H.E.S.S. standard pointing, because the Cherenkov camera lid is open during data taking and therefore no image of a star is available. The H.E.S.S. collaboration were the first to introduce a new concept, called *precision pointing*, to further improve the systematic pointing error [31, 41]. The main idea is to have a second CCD camera that monitors the sky during observation and to use this information

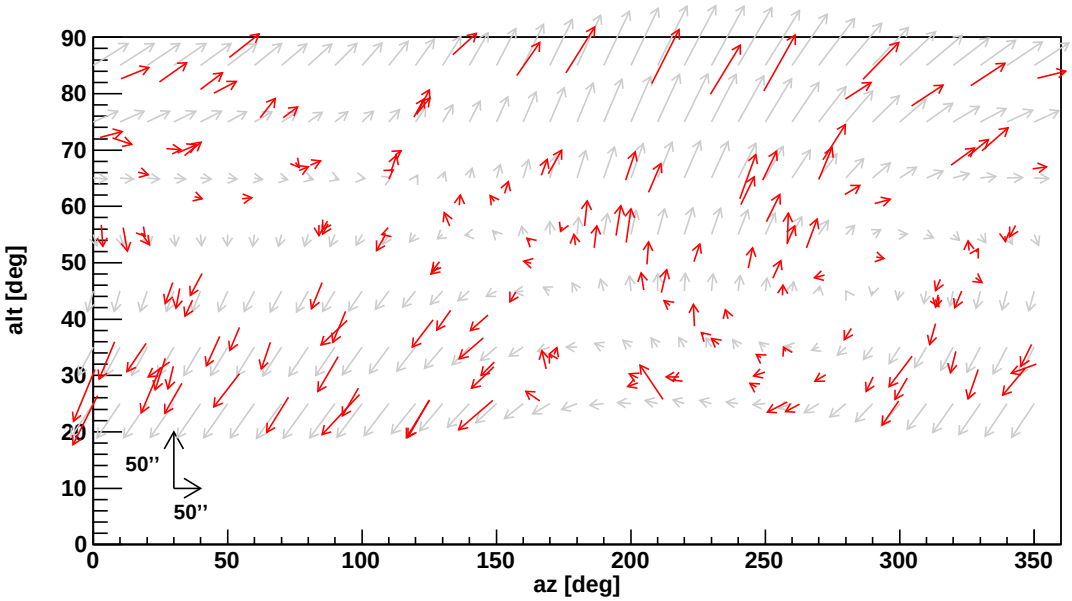

(a) The red arrows show the direction and magnitude of the telescope mis-pointing measured at the given sky position for 162 pointing runs. Grey arrows show the corrections that are derived from the fitted pointing model.

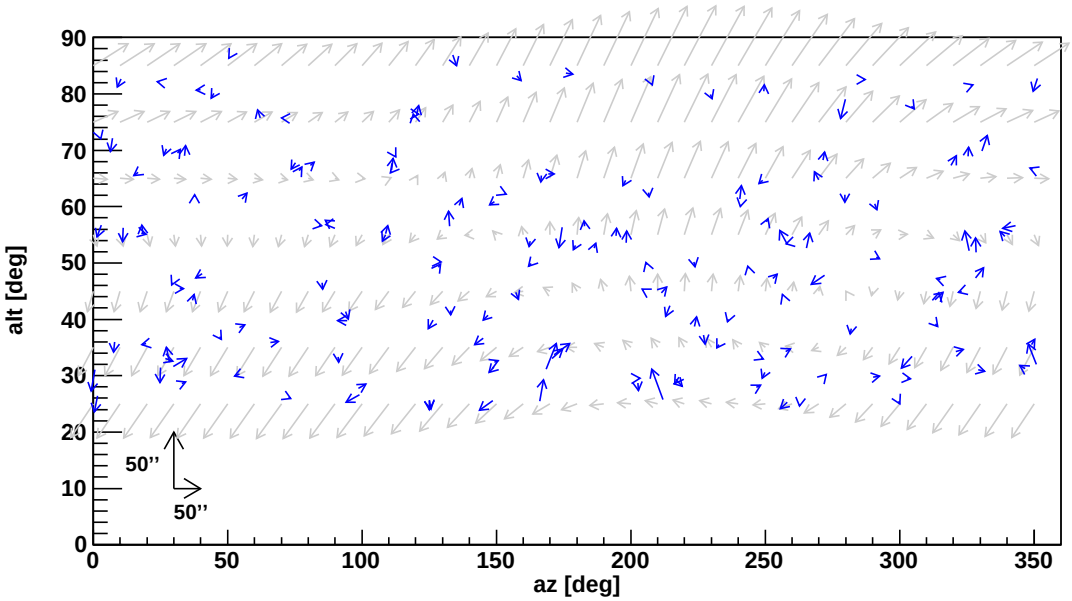

(b) Same plot as above, but now the blue arrows show the residuals between the pointing model and the measured corrections.

Figure 3.4.: Example of a pointing model for CT4 valid during P2011-08. For better visibility of details the mean pointing correction in azimuth (171″) and altitude (-73″) have been subtracted. The scale of the pointing corrections is enhanced with respect to the axes, so a mis-pointing of 5″ is represented by an arrow of 1° length (also indicated by the scale in the bottom left). The standard deviation of a Gaussian fitted to the magnitude of the residuals is 5.3″.

to predict where the stars observed by this CCD would have been on the lid if the lid was closed. For this prediction another mechanical model is needed, the so-called *SkyLid* model. Furthermore, images of the Cherenkov camera are recorded during data taking, to measure the actual displacement of the Cherenkov camera.

3.3.1. Data Collection

The data collection has two different levels. Firstly, the SkyLid model needs to be calibrated. This is done from the pointing runs as well because it requires to measure the star projected onto the closed camera lid and to see it directly with the second CCD at the same time.

The second stage is during data taking, where the two CCDs take images of the LEDs and the sky, respectively. Combining this information with the SkyLid model, it is possible to calculate a full pointing correction.

Hardware

The second CCD, called *SkyCCD*, is about 3 m offset from the LidCCD, so it has an unobscured view of the sky. It is supported by a stiff steel casing to minimise movement of the CCD. The first generation of SkyCCD is an Apogee Ap1E with a KAF-400E chip featuring 786x512 pixels. It is read out via a special PCI card. In order to transport the signal over 45 m the signal has to be boosted by a commercial boost unit. The readout is much faster than the LidCCD and takes only about 1 s for a full frame picture. The SkyCCD has a 800 mm Vixen NA120S refractor, which yields a very high angular resolution. This allows to measure the position of a single bright star with a very good statistical accuracy. Active cooling is done again with the help of Peltier elements to keep the CCDs at a constant temperature of -25 ° C.

Pointing Runs

During a pointing run the SkyCCD records ten images of the target star. They are used to calculate an average centre of gravity. The optimal exposure time is again chosen according to the magnitude of the target star. For Sirius the reference time is now $t_S = 5$ ms and therefore much lower than for the LidCCD (compare Sec. 3.2.1), which also reflects the much higher light collection capabilities of the optics.

Observation Runs

In observation runs the optimal exposure time is calculated in the same way as for pointing runs, but here the brightest star in the expected field of view is used. The exposure time is automatically adapted in case the stars are too bright or not bright enough and the maximum exposure time is limited to $t = 40$ s to minimise field rotations. Typically the Lid- and SkyCCD take $\sim$ 20 pictures per observation, which has a nominal length of normally $\sim$ 28 min. Due to the slow readout this corresponds to the maximum rate at which the LidCCD can take pictures.

Fitting the Star Image

The data reduction from the SkyCCD image to a list of spots is the same as already discussed for the standard pointing. Spots are identified as stars by looking up all stars in the field of view from a catalogue. The five brightest spots are then passed to a Minuit [37] based fitting algorithm that tries to minimise the summed square distances between the spots and the star positions. The spot list and the star list is permuted to find the best matching fit. Due to the number of combinations this method has to be limited to at most five spots, which also means that the fit accuracy does not increase further in case more spots are in the field of view. The transformation fitted is similar to the one for the LED fit:

$$\begin{aligned} x_{\mathrm{Spot}} &= S \cdot (x_{\mathrm{Star}} \cdot \cos\theta - y_{\mathrm{Star}} \cdot \sin\theta) + \Delta_x, \\ y_{\mathrm{Spot}} &= S \cdot (x_{\mathrm{Star}} \cdot \sin\theta + y_{\mathrm{Star}} \cdot \cos\theta) + \Delta_y. \end{aligned} \tag{3.12}$$

In case the permutations did not work a fallback mechanism can be applied that combines spots with the nearest stars. This only works if the offsets Δ are already small. To achieve this a second mechanical model (see Sec. 3.2.2) is fitted for the SkyCCD. It is only used as a help for the star fit, but plays no role for the calculation of the precision pointing correction. The mechanical model of the SkyCCD should be identical to the one derived in standard pointing, except for bending effects.

During this work a new algorithm has been implemented and tested that gets rid of the permutations and uses triangles between spots and stars to identify matching pairs of spots and stars [42]. If defined correctly, the properties of the triangles are insensitive to the scale S, the rotation θ and the shift Δ, so this fit always works, even if the transformation from equation 3.12 is not known at all. Therefore no mechanical model for the SkyCCD is required. Having a few star spot pairs it is possible to fix the transformation in equation 3.12 already accurately enough, so remaining star spot pairs can be added by finding close pairs of spots and stars. This has the advantage that all spots are used which reduces the statistical error. The method is not yet working reliable enough, which means that occasionally the algorithm is unable to solve the field of view. Therefore further investigations are needed.

3.3.2. SkyLid Model

The SkyLid model predicts for each position in the SkyCCD a corresponding position of the telescope optical axis in the LidCCD. Therefore, it is strictly speaking a "SkyCCDLidCCD"model because the transformations to the lid is done with the actual displacement of the Cherenkov camera. It is created from pointing runs in the following steps:

1. To first order the correlation between the position of the stars in the two CCDs is linear, thus a linear function is fitted in altitude and azimuth, which gives four parameters. The following corrections are then applied to the residuals of this fit.

2. The residuals in altitude and azimuth $\delta_{az/zlt}$ as a function of altitude alt can be fitted to a sine function of the form:

$$\delta_{az/alt} = \delta_{0,alt} + A_{\delta,alt} \sin(alt + \phi_{\delta,alt}) \tag{3.13}$$

This fit gives altogether six parameters.

3. The residuals as a function of azimuth az can also be fitted to a sine function of the form:

$$\delta_{az/alt} = \delta_{0,az} + A_{\delta,az} \sin(az + \phi_{\delta,az}) \tag{3.14}$$

   Also this fit gives six parameters.

4. A linear dependence between the residuals and the outside temperature is fitted. This adds another four parameters (two each for azimuth and altitude).

5. Finally, it turned out that the so far discussed model parameters do not change significantly over time, but only the average correction. Therefore, the aforementioned 20 parameters of the SkyLid model are typically created from four months of data. For each month the average corrections are calculated and added as two additional shift parameters. In other words, for a four month period each month has its own SkyLid model, where 20 parameters are equal and only the two shifts are different.

The fit to the residuals is done independently in each step and also the corrections are applied completely independently. Of course this neglects correlations between the different fits. However, the low residuals after applying precision pointing corrections indicate that such correlations cannot be very large. The fitting is again done iteratively and pointing runs where the residuals are larger than five standard deviation of a Gaussian fitted to the residuals in azimuth or altitude are discarded. Fig. 3.5 shows an example of a SkyLid model. More details and a demonstration of the different steps can be found elsewhere [31].

3.3.3. Systematic Uncertainties

Again, the systematic uncertainties of the precision pointing have been studied in depth elsewhere [31] and are only summarised here. Many of the instrumental effects of standard pointing cancel out here because both CCD cameras are affected in the same way. This is also the reason why the SkyLid model in Fig. 3.5 looks more homogeneous than the mechanical model in Fig. 3.4. The projection of the star onto the lid is still affected by deformations of the mirror support structure, which leads to a small bending effect than can also be seen in Fig. 3.5.

Taking into account various instrumental and methodical errors it has been shown that the systematic error of precision pointing is reduced to the order of $6''$ [31]. The pointing model has been applied to an analysis of the Galactic Centre, where the gamma-ray source has been localised with unprecedented accuracy [41].

3.4. Hardware Replacement

During this work a replacement of the Lid- and SkyCCDs has started. This was necessary for several reasons. Firstly, the current cameras show ageing effects, appearing as electronic problems when reading out the pictures. This resulted in artefacts in the images taken. Secondly, there is no spare hardware left for the CCDs and the boost units. Thirdly, a PC is needed that supports parallel ports for the LidCCDs and the special

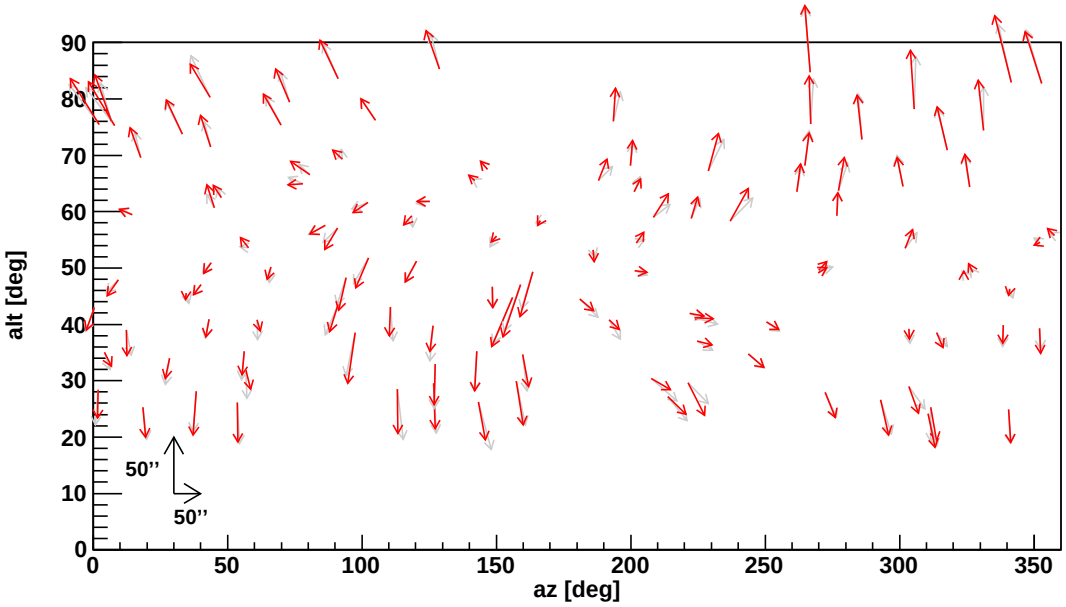

(a) The red arrows show the direction and magnitude of the shift between the star directly seen with the SkyCCD and projected on the lid for 116 pointing runs. Grey arrows show the shifts that are derived from the fitted SkyLid model.

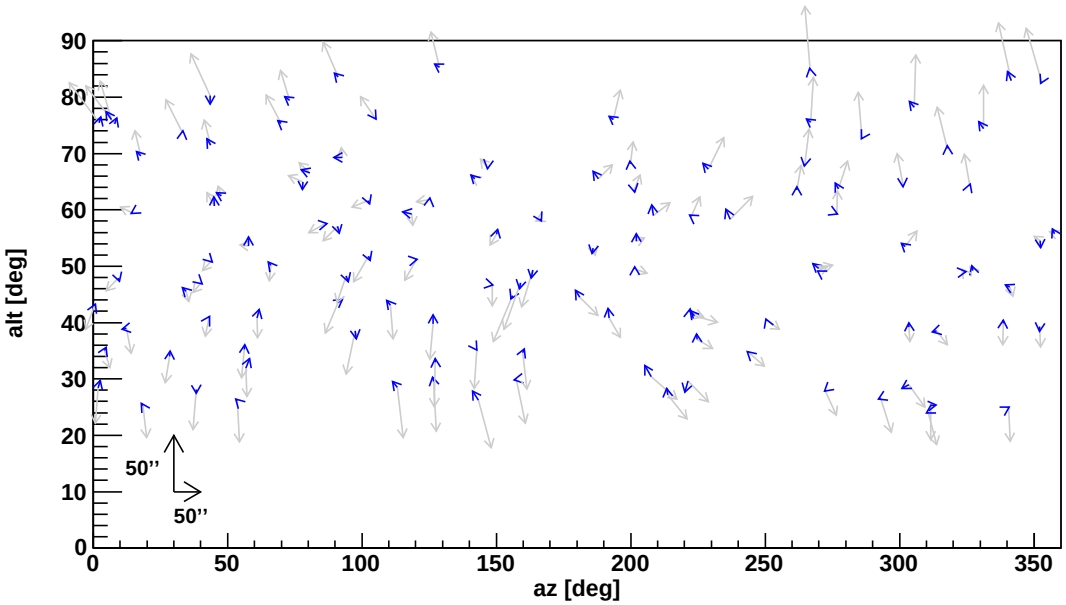

(b) Same plot as above, but now the blue arrows show the residuals between the SkyLid model and the measured corrections.

Figure 3.5.: Example of a SkyLid model for CT4 valid during P2011-04. The difference in the average shift compared to the next month is 3.6″ in azimuth and 3.7″ in altitude, however average shifts are not shown in this plot anyway. The scale of the pointing corrections is enhanced with respect to the axes, so a mis-pointing of 5″ is represented by an arrow of 1° length (also indicated by the scale in the bottom left).

PCI card for the SkyCCDs. Such machines are no longer commercially available and the current PCs are now almost 10 years old. It was therefore decided to exchange the CCDs, before a hardware failure in any of the components would cause a longer downtime. In order to have a long term test of the reliability and stability of the new system and to serve as a test bed for the CCD replacement it was decided to have a parallel installation of a new CCD along with the old ones. This test was combined with testing the SingleCCD concept that is described in Chapter 4.

The test of the new system was very successful, with only minor software problems to be solved and thus it was decided to proceed with the CCD exchange. In a first step the LidCCD on CT4 and two SkyCCDs (on CT1 and CT4) were exchanged. The exchange was organised and done by the University of Hamburg in November 2011. The last cameras are following shortly and then the SingleCCD is converted to a normal LidCCD.

In this section the new CCD cameras and the software that was developed during this thesis are discussed. Then the calibration of the new CCDs and the influence of the exchange on the pointing is shown.

3.4.1. Replacement Cameras

Cameras from the company *Apogee* were also chosen for the replacement due to the good experience with the previous cameras. A next generation Apogee camera featuring an ethernet interface was bought and tested. It turned out to work very smoothly and an ethernet interface is good because it provides a very easy way to get the signal out of the dish. Unfortunately, Apogee changed from the ethernet interface to an USB interface. The problem of USB is that the cable length is limited to 5 m, which is not enough to get the signal out of the dish.

A new concept for the CCD system has therefore been developed by the University of Hamburg [43]. In the original concept it was foreseen that the CCD is connected with a MiniPC in the telescope dish. There is a box with electronics close to the centre of the back of the mirror dish. This location, which could reach the Lid- and SkyCCD housing within the 5 m maximum cable length, is however problematic, because the electronic box has no active cooling. It was therefore decided to replace the MiniPC with a USB line extender. This allows to transport the signal from the dish to the ground. There a normal PC can be used that is more easily accessible than the MiniPC in the electronics box. The Apogee CCDs support USB 2.0, but only active line extenders, with a separate power supply, are able to handle this speed. It was decided to choose a passive line extender, which limits the maximum speed to USB 1.1. This is still much faster than the old cameras. For the choice of the replacement cameras it was important to get CCDs with the same chip size, so the same optics could be used. The LidCCD is replaced by an Apogee Alta U2, the SkyCCD by an Apogee Alta U1.

3.4.2. CCD Software

The main idea of the new CCD software is that clients (e.g. DAQ, mirror alignment software or test programs to take pictures) can use a hardware independent interface. The interface comprises a socket connection, so the clients can be completely decoupled from the machine where the hardware is connected. On the machine where the CCD is

plugged in, an ethernet server is running that connects to the low level camera drivers. The client/server connections are implemented using STCP (Simple TCP Communication), which was kindly provided by MIZZI Computer Software [44]. In case different cameras with different drivers are used in the future, a corresponding server has to be implemented that provides the same interface, but no change on the client side is needed. All software was designed keeping in mind that it should also be usable on the new H.E.S.S. II telescope. The testing on H.E.S.S. I lead to a very early readiness of the CCD system and it has also been tested with the H.E.S.S. II mirror alignment software.

Interface

A hardware independent interface for CCD cameras was first designed by Petz [45]. In a first step this interface has been adopted for the new CCDs [43]. However, this interface is not minimal and certain functions are overly complex, increasing the probability of software failures. Therefore a new interface has been developed in this thesis. The new interface is briefly described in the appendix. It significantly reduced the needed lines of code, while maintaining all hardware functionality.

One of the most important changes is removing the function threading. The advantage of threading is that several functions can be executed at the same time. However, for hardware that does not make sense, because hardware is in general single threaded, i.e. it can only execute one command at a time. Secondly, there were sophisticated software statuses for the camera. It is however much more logical to get the status directly from the CCD (e.g. if the camera is taking a picture), removing the necessity for a separate book-keeping. Finally, since the socket solution is by definition hardware independent, there is no need to have a second level of abstraction on the server side. In case new hardware is added, a new server is created using the low level drivers of the new camera.

DAQ Controller

The second piece of software that is needed for data taking is a controller for the H.E.S.S. data acquisition. It would have been possible to keep the old controller in case the old interface would have been used. However, the decision was taken to completely rewrite the controller because it was anyway foreseen to have a new controller for H.E.S.S. II. This also allowed to adopt the controller to recent changes in the DAQ. Due to optimisations, the code was also here reduced by more than a factor of two, while keeping all functionality. The functions of the new controller are briefly described in the appendix as well.

3.4.3. CCD Calibration

There are some calibration values that need to be known for each CCD to get correct pointing models. These are the pixel size, the effective focal length (f) and the rotation of the CCD against the sky (ϕ). Furthermore, for a correct pointing correction the rotation of the Cherenkov camera against the sky needs to be known (Φ), which can be extracted from the same measurements. For the pixel size the nominal values ($9\,\mu m$) are used. The effective focal length is typically expressed as the number of pixels that one degree of the Cherenkov camera is mapped onto (using a nominal distance between LidCCD and LEDs

of 15 m). This value allows a very easy conversion between CCD pixels and the (angular) distance on the camera lid.

The calibration was also repeated for the old CCDs, which was first done directly after the installation of the CCDs [30]. Φ was a parameter fitted separately during the creation of the pointing models, however it turned out that the value is constant and so it was fixed to a constant in June 2010. At that time two periods appeared to be necessary for CT4.

It can be seen in Table 3.1 that some of the calibration values currently in use had to be modified. Furthermore, it also turned out, that the calibration had to be divided into different calibration periods, probably due to work on the CCD cameras. For the CT1 SkyCCD a change is seen in October 2007 and October 2008, for the CT2 SkyCCD in September 2005 and for the CT3 SkyCCD in September 2006. The last period for the CT1 SkyCCD and the periods for the CT4 Lid- and SkyCCD correspond to the time before and after the CCD replacement in November 2011. In the following it is explained how the calibration values are obtained and why some values differ significantly. The impact of the changes is investigated in Sec. 3.4.3.

	CT1		CT2		CT3		CT4	
	Old	New	Old	New	Old	New	Old	New
$\phi_{\text{Lid}}\,[^\circ]$	0.002239	0.60	-0.00632	0.03	180.564	180.37	179.432	179.41 178.75
$f_{\text{Lid}}\,\left[\frac{\text{pixel}}{^\circ}\right]$	271.6	269.3	271.1	269.4	272.4	269.2	271.8	268.9 268.0
$\Phi\,[^\circ]$	-0.22	0.25	0.51	-0.62	-0.57	0.68	1.27 1.9	-1.73
$\phi_{\text{Sky}}\,[^\circ]$	0	-0.25 -0.44 -0.13 270.47	180	179.43 179.72	90	91.32 89.05	269.112	269.04 269.54
$f_{\text{Sky}}\,\left[\frac{\text{pixel}}{^\circ}\right]$	1544.62	1545.1 1545.1 1546.0 1547.4	1547.33	1547.5 1547.5	1546.83	1547.0 1547.0	1546.63	1546.7 1548.0

Table 3.1.: Comparison between the old and new calibration values for the different CCDs and telescopes. More than one value in a column indicates that more than one calibration period (e.g. before and after a hardware change or replacement) was used.

LidCCD Rotation against Sky

The angle between the LidCCD and the sky (ϕ) is important in order to have the correct transformation between them. In pointing runs there is occasionally a second star on the Cherenkov camera lid that is bright enough to be detected. It is possible to determine the searched rotation from a fit to these two stars. The point spread function of the telescope gets larger for bigger offsets from the optical axis, where the second star is. However,

the widening is mostly in the radial direction so that the angle between the stars is less affected. Using the SingleCCD it is possible to cross-check whether or not the method with the two stars is working (see Sec. 4.3).

Fig. 3.6 shows the distribution of the residual rotation after applying the calibration values for the different periods from Table 3.1. It can be seen that the residuals scatter around zero. This means that the calibration is correct for all periods because a wrong calibration would emerge as a second peak in the distribution.

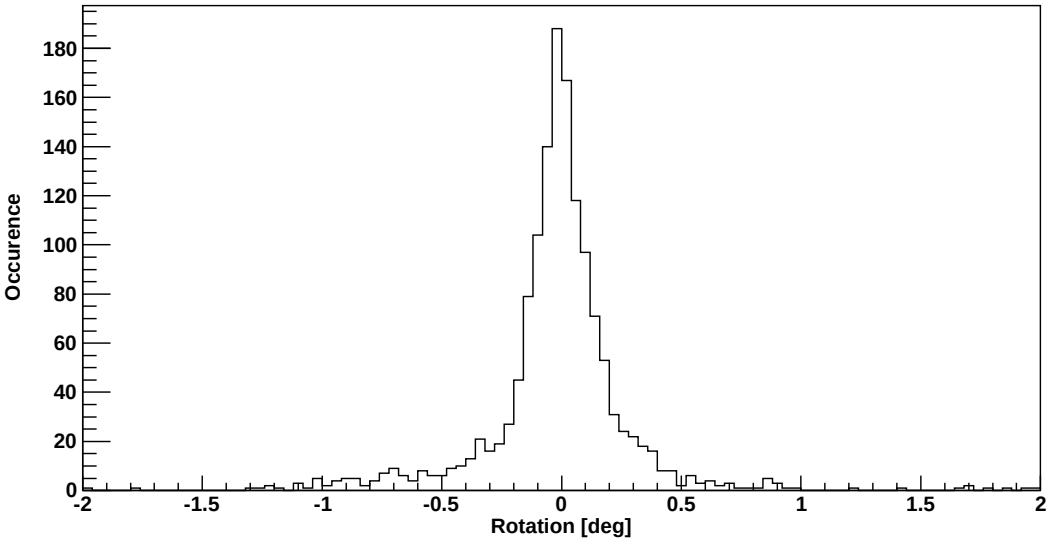

Figure 3.6.: Distribution of the residual rotation of the CT4 LidCCD against the sky after applying the calibration values. 1430 pointing runs since 2005 have been used, where a second star on the lid could be detected. Occasionally the stars are wrongly fitted or assigned, which leads to some outliers from the distribution.

LED Fit

The rest of the calibration values for the LidCCD can be obtained from a fit to the pictures with the LEDs. As it can be seen in Eq. 3.1, the fit gives back a rotation and a scale, of which the latter one can be converted to an effective focal length for the LidCCD.

If the LidCCD is correctly aligned with the sky, the fitted rotation gives the rotation of the Cherenkov camera against the sky (Φ), which is the parameter needed for an accurate pointing correction. It turns out that the fits show occasional jumps that seem to be related with maintenance work on the camera. In order to work on the drawers the funnel plates have to be removed (see Fig. 2.4), to which also the LEDs are attached. Once the plates are screwed back this can lead to small shifts, an effect which has also been observed before [31]. The jumps are of the order of $0.1\,^{\circ}$. This effect could be corrected by using different calibration periods for Φ. However, the effect of wrongly calibrated rotations seems to be small, as discussed now.

A comparison with the previous calibration values of Φ reveals that the old rotation has the wrong sign, i.e. the rotation was done in the wrong direction. This has been corrected. Furthermore, the two periods for CT4 do not appear to be necessary and both

periods can be described well with a constant value. This indicates a systematic error in the determination of the old values. The influence of the wrong sign on the data analysis has been investigated by Krüger [46]. For data taken in wobble mode only a percent level effect on the sensitivity was found and the effect on the position of sources or the point spread function is well below the systematic uncertainties.

Fig. 3.7 shows the fitted scale for CT4 for all LidCCD pictures with LEDs since 2005 ($\sim 350,000$ pictures). It shows a nice seasonal variation, which can also be seen with the same strength and temporal behaviour for the LidCCDs on the other telescopes. Since the CCD chip itself is cooled, the reasons for this has to be thermal expansion in some external part. Possible explanations are the lens, the CCD mount or the telescope structure itself. A cross-correlation with the SingleCCD indicates that thermal expansion of the telescope structure should be the dominant effect (see Sec. 4.3). The scale has a minimum in Namibian winter. This could be explained by a shorter distance between CCD and LEDs, which is the expectation for thermal expansion.

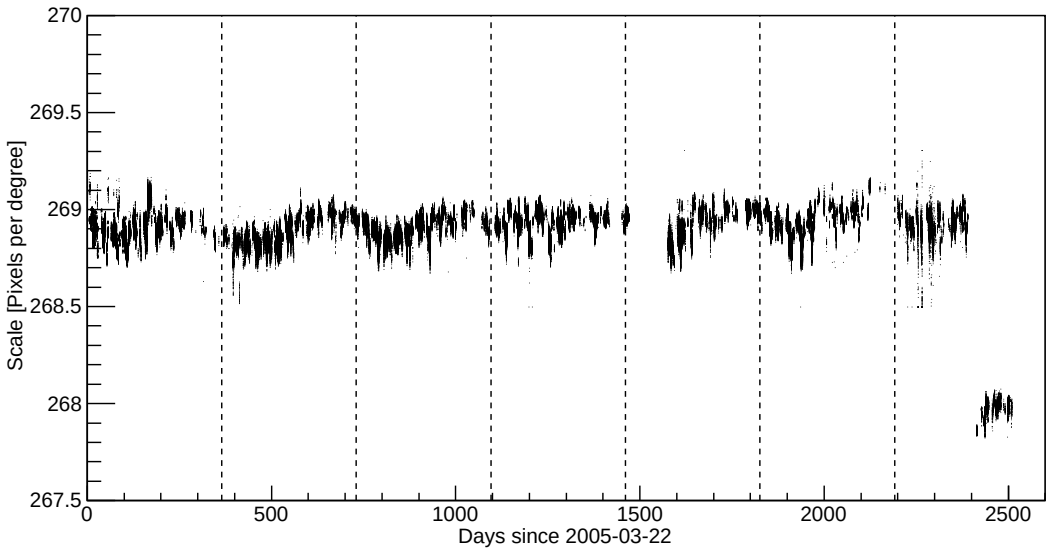

Figure 3.7.: The scale, which expresses the effective focal length, for the CT4 LidCCD in $\sim 350,000$ images since 2005, where the dotted lines indicate a time period of one year. A clear indication of seasonal variations can be seen. The last 100 days correspond to the time after the CCD replacement and it can be seen that the scale has changed. Since the lens is the same, this effect must arise from the camera focus.

SkyCCD

The calibration values for the SkyCCD can be very easily obtained by fitting the images with stars. Due to the large number of SkyCCD images (typically $> 120,000$ images) it does not matter if single images are not fitted correctly, so the new star finder (compare Sec. 3.3.1) can be used. No mechanical model or correction for atmospheric refraction needs to be applied, because the new star finder can identify the sky independent of

shifts. From a fit according to equation 3.12 the scale and the rotation are obtained, which directly give the searched calibration values.

LidCCD Tilt

In the original work [30] there were two other calibration values, namely a tilt (in two directions) of the LidCCD with respect to the Cherenkov camera lid. Possible tilts of the LidCCD, the chip inside the LidCCD or the Cherenkov camera lid haven been investigated by Krüger [47] and the results are summarised here.

A tilt of the LidCCD leads to two different effects: it adds a global translation of the coordinates and creates a so-called keystone effect, that makes a rectangular image look like a trapezoid. However, the tilt of the LidCCD is implemented separately for the two directions, which correctly reproduces the translations, but not the keystone effect.

It was necessary to tilt the LidCCD when it still had the 180 mm lens, so that three LEDs are in the field of view. After the lens was replaced with the 135 mm one, a large translation is no longer observed, meaning that the centre of the lid is more or less in the centre of the CCD chip. Thus, the tilt has to be much smaller than what is currently used.

The reason that this wrong tilt was not noticed before is the fact that translations cancel out in the pointing correction. For standard pointing, only the relative difference between the Cherenkov camera centre and the star projection onto the lid is important. In the SkyLid model, which maps the SkyCCD onto the LidCCD, the average correction changes by the translations. This does however not effect the precision pointing correction, because again only the difference relative to the camera centre is important. It was therefore decided to fix the tilt values to zero.

There can be two additional sorts of tilts, namely of the Cherenkov camera lid or the CCD chip. They would lead to an additional scaling effect because due to the tilt distances on one side of the image appear smaller than they actually are. This is however not important for pointing, because it does not influence the fit of the camera centre. Both tilts are not easy to distinguish, because the results are similar. The tilts have been fitted for all CCDs and are of the order of $\sim 0.5 - 2.0°$ [47], which is in good agreement with an earlier measurement using differences in the spot appearance in different corners of the CCD chip [31]. However, it looks like the effect on pointing due to chip tilt is smaller than what has been estimated earlier [31]. For a typical wobble offset of 0.5 ° the effect on the position is smaller than 1″ [47], thus this effect is negligible and it has not been added as a further correction.

Exposure Times

For the new CCDs the exposure times for the star images had to be newly calibrated. The exposure time t for the image of a star with apparent magnitude m is calculated by $t = t_0 \cdot 2.512^{m-m_0}$. For the new LidCCD $m_0 = 2$ and $t_0 = 6\,\mathrm{s}$ and for the new SkyCCD $t_0 = 0.06\,\mathrm{s}$. Comparing these values with the old calibration on Sirius it can be seen that the new CCDs are a factor of $\sim 2 - 3$ more sensitive. This gain can mostly be attributed to the higher quantum efficiency of the new CCD chip compared to the old one.

3.4.4. Influence on Pointing

In this subsection the influence of the exchanged CCD cameras and the re-calibration of the CCDs on the H.E.S.S. standard pointing is investigated.

Table 3.2 compares the mean spot size of the LEDs seen by the LidCCD and the stars seen by the SkyCCD. The spot size is given by the two dimensional root mean square of the pixel distribution and was computed with the stable algorithm described in [32] (compare also the discussion in Sec. 3.2.1). This algorithm has a remaining systematic error of about 0.1 pixel. It can be seen that the spot size increased for CT4, which means that the focus is not as good as it was before (the change in focus can also be observed in Fig. 3.7). It is desirable to have the optics slightly defocussed, so the spots are distributed over several CCD pixels, which allows a precise determination of the centroid. However, if the defocussing is too strong, the determination gets worse again. The decreasing size for CT1 can be explained with an electronic problem the old SkyCCD was experiencing. It lead to clipping of the spots, so the central parts of the spots were not as bright compared to their edges, which lead to an increase in the apparent spot size. However, also the new mean size value is higher than the other two on the unchanged telescopes.

	CT1		CT2		CT3		CT4	
Size	Before	After	Before	After	Before	After	Before	After
LidCCD [pixel]	1.9	—	1.9	—	2.1	—	2.3	2.8
SkyCCD [pixel]	4.2	3.6	2.7	—	3.0	—	3.1	3.7

Table 3.2.: Comparison of the mean spot size before and after the corresponding CCD exchange, using CCD images from pointing runs between 64813 and 69155.

Another problem after the replacement is that the SkyCCDs are not as accurately aligned with the optical axis of the telescope than before, so the star in a pointing run is no longer in the centre of the chip. This could lead to systematic effects due to spherical aberrations.

CCD Replacement

Figure 3.8 shows the first pointing model after the LidCCD exchange on CT4. It looks very similar to the one in Fig. 3.4, which means that the model creation with the new CCD works as expected. In order to make changes better visible the differences between the previous and current model have been evaluated for fixed positions on the AltAz grid. Figure 3.9 shows that the mean correction has changed by more than 200″. This difference can be attributed to the mirror exchange on CT4 that was done at the same time, which means that the optical axis of the telescope has changed by this amount. There is a slight change in model shape, which is not unusual, because it is observed for all telescopes when comparing the temporal evolution of pointing models. In conclusion, the new mechanical model after the LidCCD replacement of CT4 looks as good as the old one. This also means that the focussing can only have a minor impact on the model.

The same is also true for the mechanical model of the SkyCCD. Here the mean correction has changed significantly ($> 1000''$ for CT1) because the CCDs are not so accurately aligned with the optical axis. For the residua of the SkyCCD mechanical model this

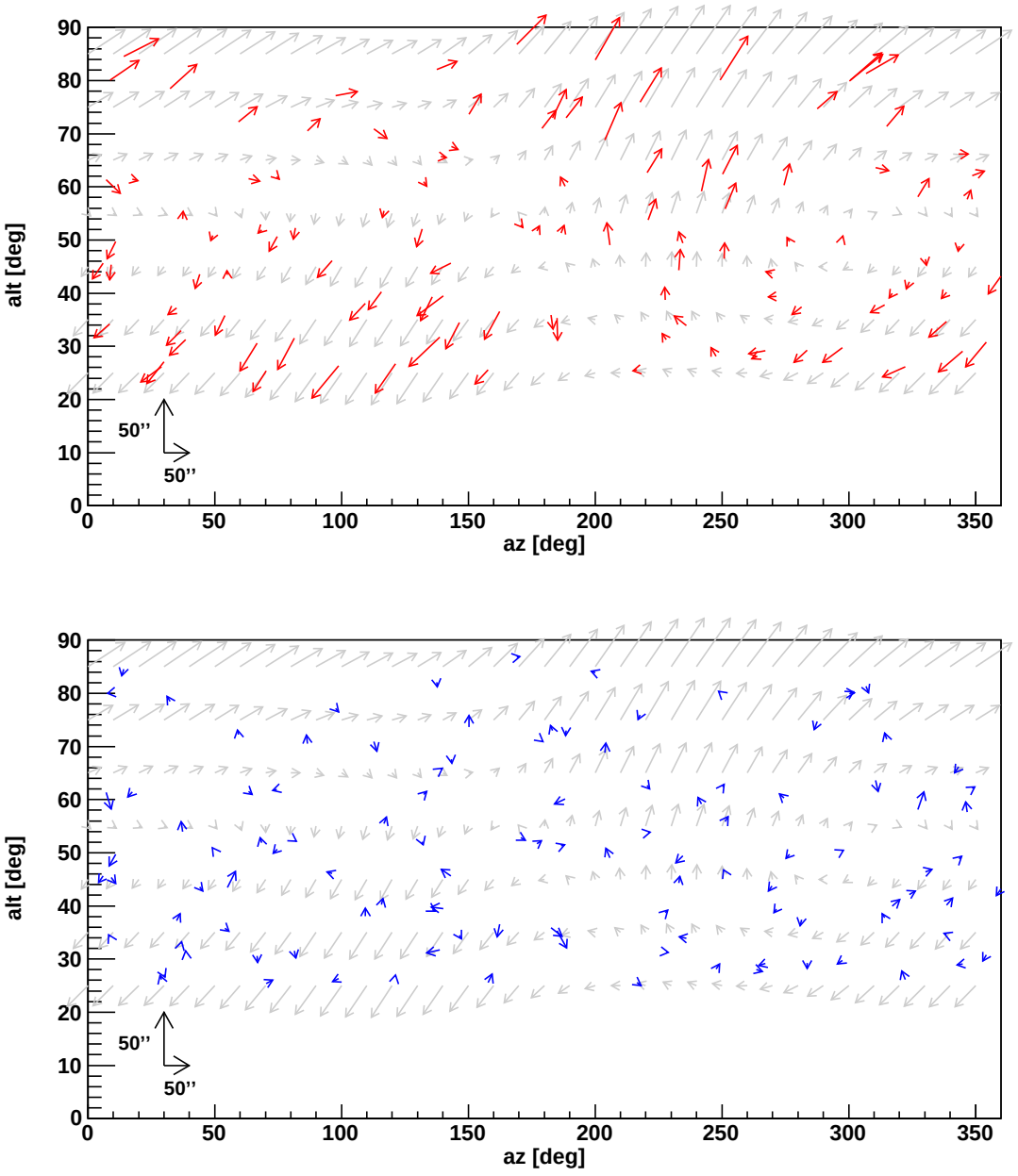

Figure 3.8.: Same plot as Fig. 3.4, but now for the first pointing period after the replacement of the LidCCD on CT4. The model has very small residuals, the standard deviation of a Gaussian fitted to the magnitude of the residuals is only 4.2″.

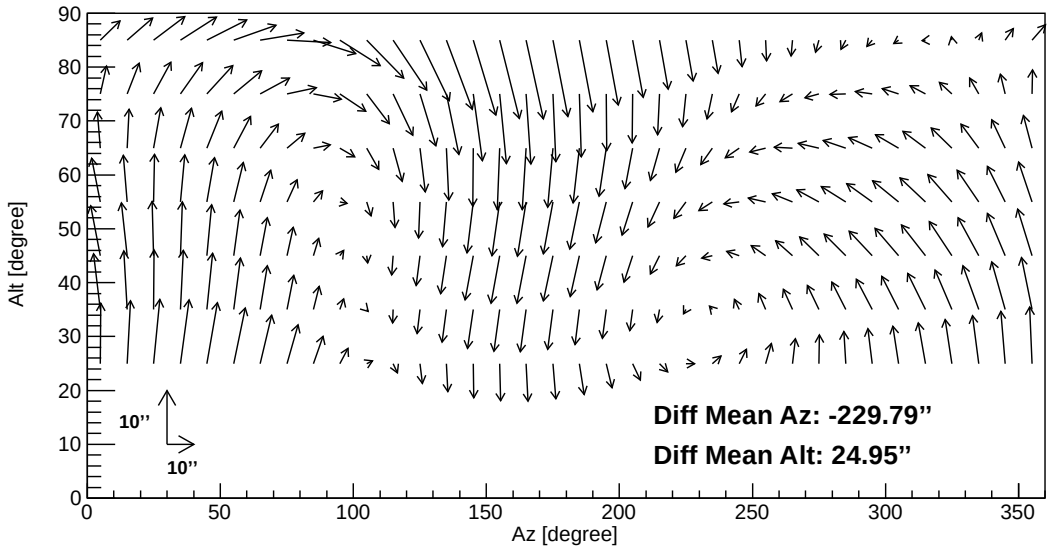

Figure 3.9.: The differences between the pointing correction evaluated at each point for the CT4 mechanical models in P2011-11 and P2011-08. There are some small differences in shape. However, similar changes are also observed when looking at the temporal evolution of other pointing models.

has no impact, but it remains to be seen if there is a systematic effect for the precision pointing correction.

Re-calibration of CCDs

Now it is discussed, what the influence of the new calibration of the old CCDs (before the exchange) is. For the mechanical model of the camera only the difference between the star and the Cherenkov camera centre is important, so removing the tilt (which gives a translation) and fixing the calibration should only have a minor effect. The differences between the new and old models are indeed small and the models do not change significantly in shape. The mean of the distribution of the amplitude of the differences is of the order of $\sim 5''$, which is small compared to the standard deviation of the Gaussian fitted to the residuals or the systematic error of standard pointing. Therefore the new models are as good as the old ones. Occasionally a model differs slightly more in the magnitude of the differences and the shape. This may indicate a very broad minimum or two nearby minima, where Minuit has problems. However, even there the differences are still much smaller then the systematics so a further study does not appear to be necessary at the current time.

For the mechanical model of the SkyCCD large differences in the mean correction are seen. This is because in pointing runs only one star is in the field of view, so the rotation cannot be fitted. Therefore, a change of the rotation also changes the corresponding model. This is not a major problem, because the wrong shift is reverted once the correct rotation is fitted from the sky.

Also the SkyLid models show large differences in the mean correction. This is because the tilt and therefore a large translation of the lid is removed. This does however not

indicate a problem, because again, for the precision pointing correction only the difference to the Cherenkov camera centre is important, which is shifted by the same value when removing the tilt. The newly calibrated rotation leads to slightly smaller residuals after the SkyLid model fit, which indicates that the new calibration is better than the old one. The corresponding SkyLid model changed by $1 - 2''$, which should further reduce the systematic error for precision pointing.

3.5. Summary

This chapter has introduced the H.E.S.S. standard and precision pointing. During this thesis various improvements have been made, like the re-calibration of CCDs and the newly implemented LED fit. Furthermore, the software necessary for using CCDs for the H.E.S.S. II pointing has been implemented and successfully tested in a replacement of the H.E.S.S. I CCD cameras. The replacement was organised and conducted by the University of Hamburg. Unfortunately, the exchanged cameras are slightly less focussed and the SkyCCDs are not as accurately aligned with the optical axis of the telescopes as before. In this work the impact on standard pointing has been evaluated and was found to be small. It remains to be seen if the same is also true for precision pointing.

Chapter 4

The SingleCCD Concept

In the last chapter the H.E.S.S. standard and precision pointing have been introduced, where two optical CCD cameras are used to monitor the position of the Cherenkov camera and the sky. A so-called SkyLid model is used to connect the information from the two CCDs in order to model a pointing correction simultaneously to the data taking. One source of systematic uncertainty is that the two CCDs can have unpredictable movements relative to each other.

This is avoided with the SingleCCD concept, where the two CCDs are replaced by one camera that observes the Cherenkov camera and the sky in parallel. Another obvious advantage is that only one CCD is needed, which saves cost, complexity and maintenance. This is especially interesting for the next generation of Imaging Atmospheric Cherenkov Telescopes, e.g. CTA, which will comprise a large number of telescopes ($\mathcal{O}(100)$). However, the SingleCCD has also disadvantages because the measured spots are larger and the resolution is lower than for the current CCDs (further details can be found in Sec. 4.1).

The main aim of this chapter is to test and evaluate the feasibility of the SingleCCD concept and to compare the performance to the H.E.S.S. precision pointing. In a first step laboratory measurements were done, before a SingleCCD test camera was installed in addition to the normal CCDs on a telescope in Namibia (Sec. 4.2). Section 4.3 shows the calibration of the SingleCCD and interesting cross-calibrations that can be done when comparing to the normal CCDs. The last section shows that the SingleCCD concept works in principle. However, due to technical problems further work is needed to directly compare to the H.E.S.S. precision pointing.

4.1. Challenges

In the SingleCCD concept a single CCD is used to monitor both the movement of the Cherenkov camera and the sky. This brings some obvious challenges compared to the traditional approach with the two CCDs, which are described in detail in the current section.

4.1.1. Focus

If the focus of an ideal camera is changed is such way that a point-like object produces a point-like image, the object is said to be in focus. It is obvious that the SingleCCD cannot have the Cherenkov camera and the sky in focus at the same time. If an object is moved out of the focus, the image it produces is blurred and the diameter of the blurred spot is called the circle of confusion (C).

For real cameras a point-like object in focus always produces an image of a certain size. This means that the object can be moved in distance around the focus within certain limits without appearing to get out of focus. The distance range around the focus where the image still appears to be acceptably sharp is called the depth of field (DoF). If one changes the focus of the CCD such that the DoF extends to infinity, the corresponding focus lies at the so-called hyperfocal distance (H). At the hyperfocal distance the DoF has the maximum extend from half the hyperfocal distance to infinity.

A plausible solution to observe the LEDs and the stars at the same time is to bring both planes equally out of focus. In other words this means that the circle of confusion for LEDs and stars is identical. Since the stars are at an infinite distance and the LEDs on H.E.S.S. I are at a distance of 15 m this aim is reached when the focus of the CCD lies on the hyperfocal distance of 30 m.

It is possible to influence the circle of confusion and thereby the spot size because it is directly proportional to the aperture D of a lens with focal length f:

$$C = D\frac{f}{H - f} \tag{4.1}$$

So in principle the blurring of the spots can be controlled by sufficiently closing the aperture, which, however, means longer exposure times. The main aim of the laboratory tests in the Sec. 4.2.1 was to find out if the spot sizes are still controllable for reasonable apertures.

4.1.2. Resolution

In the SingleCCD concept, the sky can only be seen beyond the edges of the Cherenkov camera. This means that a large field of view is needed. For example for the H.E.S.S. I telescope the Cherenkov camera has a diameter of 1.6 m. However, there is some support structure around, which increases the total blocked diameter to 2.2 m. For realistic chip sizes this means that the resolution of the current SkyCCD (which is 2.3″ per pixel) cannot be reached.

One possibility to compensate for the loss of resolution compared to the SkyCCD is to use more stars in the fit, which come with a larger field of view. However, if the aperture D is closed to reduce the circle of confusion, less stars are detected for a given exposure time. The main goal of the test setup in Namibia is to check whether or not sufficiently small spots can be generated while still having enough stars for an accurate fit.

4.1.3. Spherical Aberrations

Since the sky is only seen beyond the edges of the Cherenkov camera, the stars are always far off the optical axis of the CCD. This could introduce systematic effects like e.g. optical aberrations. Such effects might cancel out if stars are observed around all sides of the Cherenkov camera (like for the LEDs on the Cherenkov camera, see Sec. 3.2.1). In the SingleCCD test setup installed in Namibia this was not the case because the CCD had to be installed additionally on the telescope and the central spot is blocked by the LidCCD. Thus stars are only observed beyond one side of the camera (see Sec. 4.2.2).

4.2. Preparatory Work

In the first part the influence of LEDs on and off focus on the spot size has been investigated in a laboratory test. The test were encouraging and therefore a SingleCCD has been installed in Namibia (Sec. 4.2.2).

4.2.1. Laboratory Tests

In order to understand the relationship between the circle of confusion and the root mean square of the pixel distribution (spot size) and to verify the relation between the circle of confusion and the aperture (Eq. 4.1) a series of laboratory tests were carried out by Herpich [32]. Here only the most important results are summarised.

Data Taking

The investigation was done for a H.E.S.S. II like telescope with a focal length of 36 m, using a 135 mm lens, the same that is currently also in use in the optics of the LidCCDs. However, the results can easily be adapted for the H.E.S.S. I telescopes. Three LEDs were attached to a board in 36 m distance. They are in LED housings with a pinhole blind and a diffusor, similar to the ones seen in Fig. 2.4.

Two series of images were taken. In the first series the camera was focussed to 36 m and pictures of the LEDs were taken over a long time in order to test the H.E.S.S. spot extraction algorithm. The LEDs lose brightness over time and thus provide a set of pictures with decreasing intensity of the LEDs. The spot size should be independent of the spot brightness.

For the second series of images, the LED plane was put out of focus. Due to insufficient space in the lab it was not possible to focus the camera on the hyperfocal distance for H.E.S.S. II, which is 72 m. By focussing the camera on 24 m instead, an equally large circle of confusion can be achieved. The LEDs are now at the end of the depth of field, while for 72 m they would be at the beginning (consecutive fields of view). The spot size was investigated as a function of aperture and for each aperture forty pictures were taken. The exposure times were adjusted for each aperture to get a comparable signal.

Results

From the first series of images it was seen that the H.E.S.S. spot extraction algorithm (see details in Sec. 3.2.1) returns inconsistent values for the spot size because they depend on the intensity of the LEDs. The algorithm was modified to minimise this effect as much as possible (see description in [32]). The spot size has a remaining systematic error of about 0.1 pixel.

Figure 4.1 compares the spot size of the LEDs in and out of focus. It can be seen that the spot size shows a nice linear behaviour for the larger apertures as expected from Eq. 4.1. The size settles to a more or less constant value for smaller apertures, which must correspond to the intrinsic size either the used lens creates or the pinhole blinds have themselves. Furthermore, already for a relative aperture of four the spots are even smaller than the LEDs on focus, which were taken with a relative aperture of two. Using

Eq. 4.1 an aperture of four corresponds to a circle of confusion of ~ 7 pixels. The spot size (root mean square of the pixel distribution) is much smaller than the circle of confusion.

One of the results obtained after the replacement of the CCDs discussed in Sec. 3.4 is that the focussing of the CCDs appears to have only a minor impact on the pointing model. This means larger circle of confusions might still be acceptable, so it might not be necessary to reduce the aperture at all. However, this knowledge was obtained much later than the investigations described in this chapter.

4.2.2. Test Setup in Namibia

As discussed in Sec. 3.4 a replacement of the Lid- and SkyCCDs has started during this work. In order to have a long term test of the reliability and stability of the new CCD system a parallel installation was done. This test bed was used to evaluate the feasibility of the SingleCCD concept. The SingleCCD is identical to one of the LidCCDs used in the replacement and is later converted to a LidCCD as the replacement proceeds.

Optics

For the SingleCCD a 85 mm lens was bought, for which the chip size yields a nominal field of view of 9.3 ° times 6.2 °. Due to the size of the Cherenkov camera and the support structure, 8.4 ° times 8.4 ° of the field of view are blocked, so stars are only visible beyond the longer side of the chip. In order to accommodate the SingleCCD in the central part of the telescope, it was placed 42 cm below and 9 cm right from the LidCCD (see Fig. 4.2). The SingleCCD observes the stars below the Cherenkov camera because the Cherenkov camera gets hot and the heat is dissipated with air cooling. The hot air might disturb the pictures of the stars above the camera. The small displacement yields a total unblocked field of view of about thirteen square degrees, which is about eighty times larger than the field of view of the current SkyCCDs. The nominal resolution is 21.9 ″ per pixel, which is about a factor ten worse than the resolution of the current SkyCCDs (2.3 ″ per pixel).

Installation

The SingleCCD was installed in Namibia in April 2011. The focussing to the H.E.S.S. I hyperfocal distance was done inside the control building by minimising the black white transition of a stripe pattern at a distance of 29.6 m from the CCD. For the lens an aperture of four was chosen, which according to Eq. 4.1 corresponds again to a circle of confusion of ~ 7 pixels. This is the value that was found to be undistinguishable from LEDs on focus in the laboratory test.

Data Taking

The SingleCCD takes data simultaneously and independently of the other two CCDs on the telescope. During observation runs the SingleCCD alternates subframes that have the Cherenkov camera or the sky in the frame. For the sky a constant exposure time of 10 s is used, which is automatically lowered in case a star is too bright. During a pointing run an additional subframe with the pointing star on the lid is taken. The exposure time t for a star with apparent magnitude m is calculated by $t = t_0 \cdot 2.512^{m-m_0}$, where $m_0 = 2$

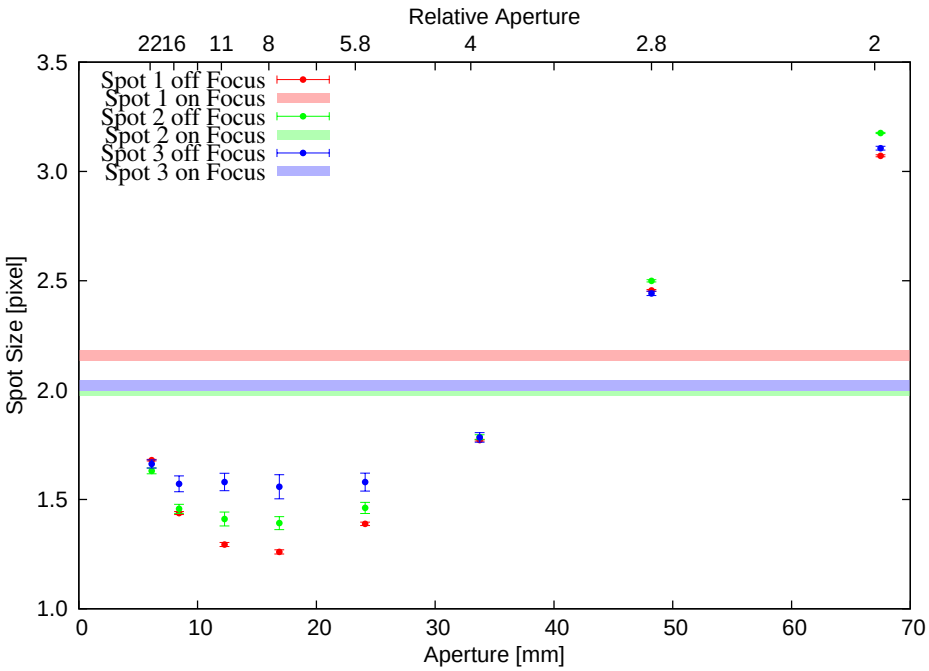

Figure 4.1.: Comparison of the spot size as a function of aperture [32]. The solid lines correspond to the one sigma range of the spot size for the LEDs on focus with a relative aperture of two. The points correspond to the spot size with LEDs out of focus as a function of the aperture. The last three points show a nice linear behaviour between spot size and aperture.

Figure 4.2.: The picture shows the LidCCD in the central part of the CT2 dish and the SingleCCD in the bottom right part.

and $t_0 = 16\,\mathrm{s}$. As expected, the exposure time is larger than for the replaced LidCCDs (see Sec. 3.4.3) because the aperture is smaller. The data reduction is identical to the one that is done for the Lid- and SkyCCDs (see Sec. 3.2.1).

4.3. Calibration

The SingleCCD needs to be calibrated in the same way as the other CCDs (see Sec. 3.4.3). The techniques and fits are the same as previously described. However, having only one CCD has the advantages that ϕ_{Lid} and ϕ_{Sky} and f_{Lid} and f_{Sky} should be identical. Obtaining the values with different methods allows some interesting cross-calibrations, which will be discussed in this section. The first part compares the spot sizes of stars and LEDs with the expectation from the laboratory tests.

4.3.1. Size Analysis

Fig. 4.3 compares the spot size of the LEDs and the stars in the SingleCCD images. It can be seen that the LEDs appear slightly larger than in the laboratory test. A possible explanation could be that the intrinsic size of the LEDs appears large, because the CCD is closer to the lid, however the values are still in good agreement. The spots of the stars are slightly larger than those of the LEDs. One reason is the so-called seeing that blurs only the images of the stars. However, assuming $2''$ seeing for the stars would lead to a 0.1 pixel difference, thus also other effects must play a role. The most plausible explanation is that the focus is not exactly at the hyperfocal distance. It was chosen by hand and the closer the focus is to infinity the harder it is to set it accurately.

However, the spot size for LEDs and stars are still in reasonable agreement. The spot size should not be a major issue, also given the fact that the focussing of the CCD appears to have only a minor impact on the pointing model (see Sec. 3.4).

4.3.2. Camera Centre

Fig. 4.4 shows the absolute position of the Cherenkov camera centre as pixel number in the SingleCCD chip. It can be seen that the camera centre appears to be moving. This is not seen by the LidCCD during the same period, so the reason must be that the SingleCCD housing is not attached firmly enough to the telescope. The horizontal camera centre exhibits a discrete jump of approximately one pixel for large zenith angle observations. There is a hint of a similar behaviour for the old LidCCD, assuming that it would always appear along the same orientation of the chip. This points to an effect that is related to the way the chip is fixed internally inside the camera.

Unfortunately, absolute position plots, like the Cherenkov camera centre as a function of altitude as seen in Fig. 3.3 or a comparison between the fitted camera centre between the Single- and LidCCD are not straightforward to make, because they would always be superposed by the movement of the SingleCCD. One could try to correct for this effect, e.g. by fitting straight lines to the drifts. Furthermore, the jump of the horizontal camera centre for observations with zenith angle larger than $45\,^\circ$ needs to be corrected, or the plots restricted to lower zenith angles. However, the gap between the two levels does not seem to be constant with time. In any case will the informative value of the plots strongly

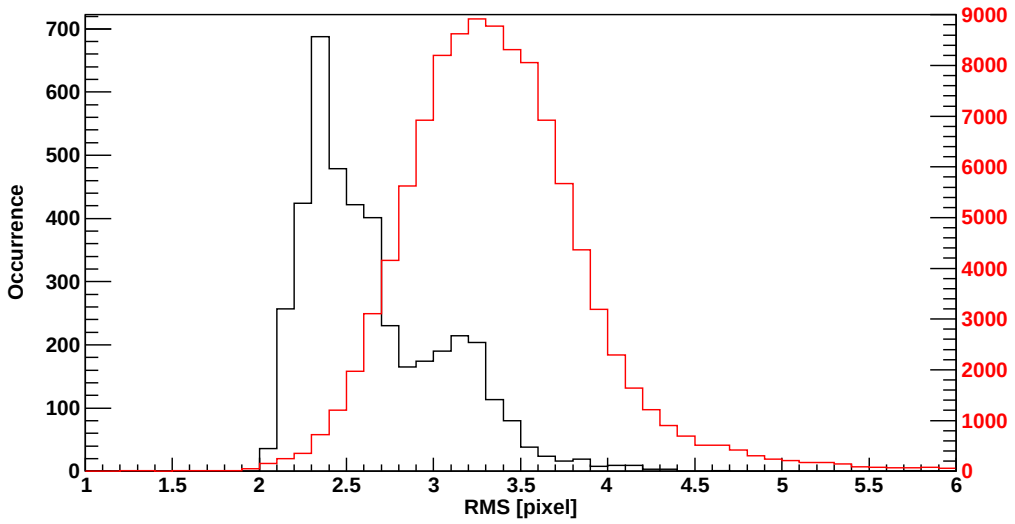

Figure 4.3.: Comparison between the spot sizes of the LEDs (black) and stars (red) both seen by the SingleCCD (pointing runs between 66395 and 68305, corresponding to the pointing model period P2011-08). The statistics for both is different because one exposure of the sky can contain more than one hundred stars while a picture of the Cherenkov camera can contain at most eight LEDs. Two LEDs appear larger and produce a second peak in the distribution. A possible explanation is a bigger intrinsic size of the corresponding diffusors.

depend on the quality of the corrections, which will introduce additional systematics, that need to be carefully studied.

4.3.3. Rotation

The rotation of the SingleCCD against the sky (ϕ) can be derived by two different methods. Firstly, the SingleCCD sees the sky directly, so the rotation can directly be derived from the images of the sky. Additionally, also the method using two stars on the lid that has been introduced in Sec. 3.4.3 can be used. This allows one to verify if the method with the two stars is working accurately.

The direct fit from the sky images reveals that ϕ is very stable over time and obviously not affected by the movement of the SingleCCD (see Fig. 4.5). A cross-check with the two star method shows that the same value for the rotation is found (see Fig. 4.6), so no systematic effect or bias is observed. Thus, the two star method is accurate to a level of $0.1\,^{\circ}$.

Furthermore, also the rotation of the Cherenkov camera against the sky (Φ) can be cross-checked. The comparison of the values derived with the SingleCCD and the LidCCD (after the re-calibration) shows that both values are identical within $0.02\,^{\circ}$, which is smaller than the effect that is seen when work on the Cherenkov camera is done. Thus the rotation of the Cherenkov camera has been confirmed independently with two different CCD cameras.

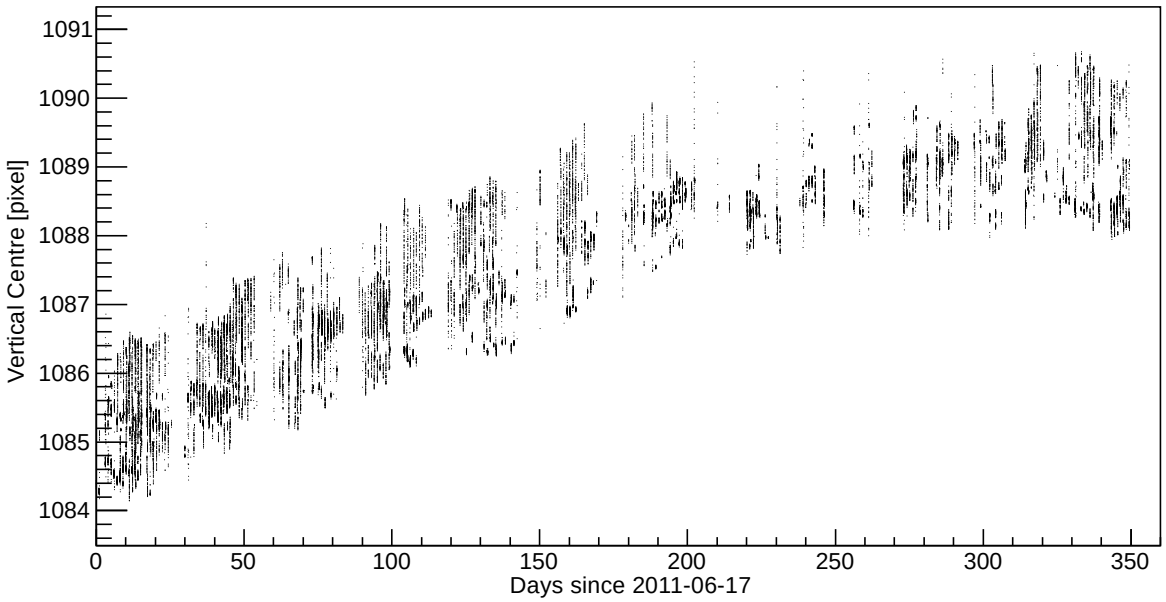

(a) Vertical camera centre as a function of time. The spread in the values originates from runs taken at different zenith angles and the resulting gravitational pull on the camera. It can be seen that the SingleCCD stopped moving down after about 220 days after the installation.

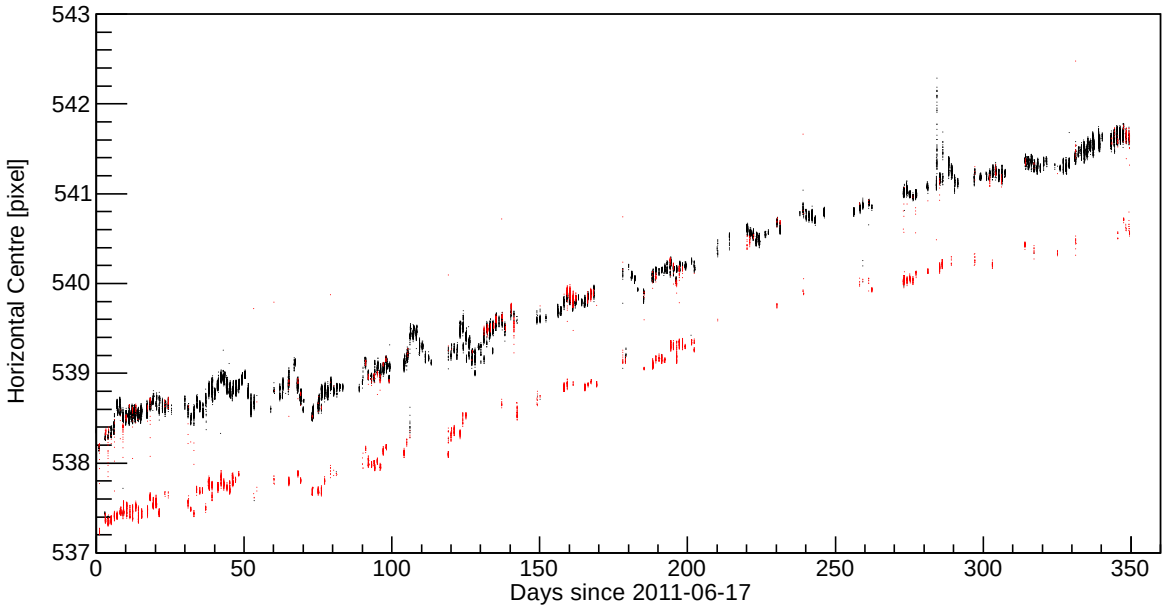

(b) Horizontal camera centre as a function of time. The red points correspond to runs taken at zenith angles larger than 45°.

Figure 4.4.: Position of the Cherenkov camera centre as seen by the SingleCCD as a function of time (observation runs between 64700 and 72428). Each point corresponds to one determination of the camera centre. One pixel corresponds to a movement of 9 μm of the SingleCCD chip.

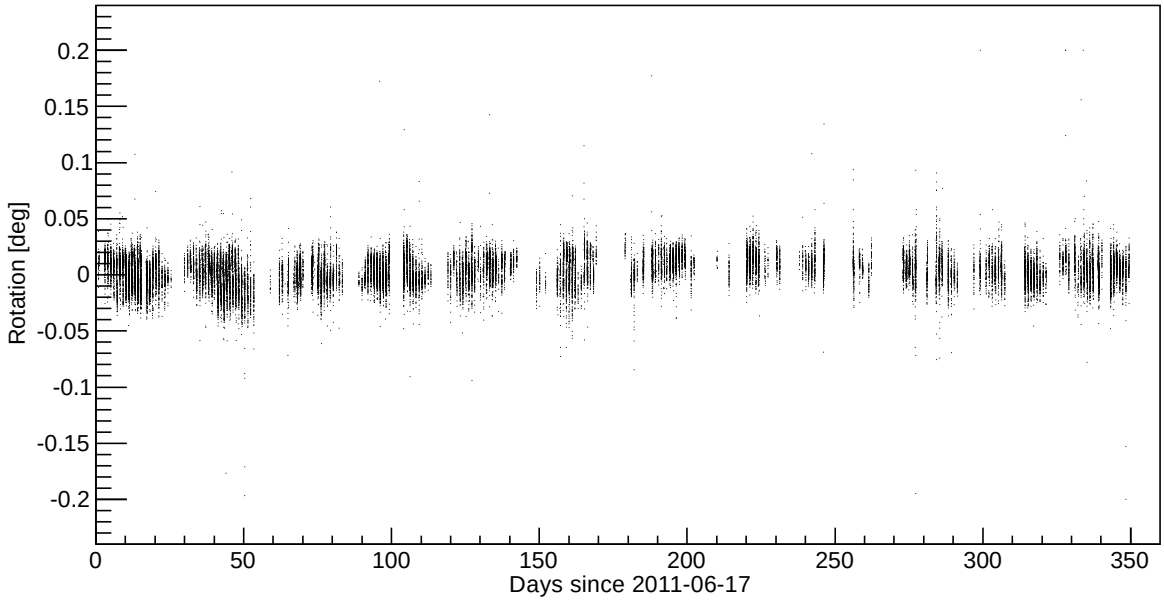

Figure 4.5.: Residual rotation of the SingleCCD against the sky fitted directly from the sky as a function of time after applying the best fit calibration value of -0.05 °. Each point corresponds to one fit of the sky using observation runs between 64700 and 72428.

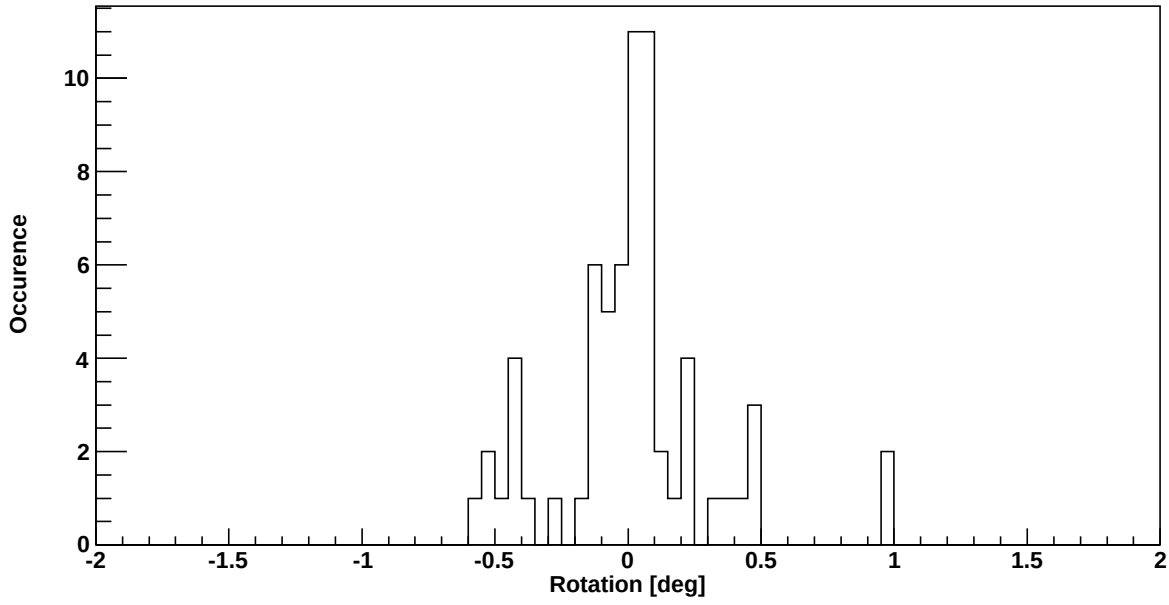

Figure 4.6.: Rotation of the SingleCCD against the sky derived with the method using two stars on the lid using pointing runs between 64700 and 72428 after applying the best fit calibration value from the direct sky fit of -0.05 °.

4.3.4. Scale

For the SingleCCD the scale, which is the effective focal length, can be derived separately from the fit of the LEDs on the Cherenkov camera and the images of the sky. This allows various cross-checks. Firstly, the scale from the LED fits from the SingleCCD and LidCCD can be compared. Both fits show identical variations, as expected if thermal expansion in the telescope structure is the reason for the change.

Secondly, for the SingleCCD the scale from the LED and the star fit should be identical because they use the same optics. However, the fitted scales are not identical (see Fig. 4.7), but differ by approximately one pixel per degree which indicates that the nominal distance of 15 m is not correct. The difference can be explained if the SingleCCD chip is only 14.92 m from the LEDs. This is plausible because the CCD is inside a housing and only the base of the housing is in the nominal centre of the dish.

Thirdly, it can be seen in Fig. 4.7 that the scale from the sky fit shows muss less signs of seasonal variations than the scale from the LED fit. This strongly indicates that the seasonal variations arise mostly from outside the CCD system, e.g. due to thermal expansion of the masts or the camera lid itself.

4.4. Verification of the SingleCCD Concept

This section discusses various ways to verify that the SingleCCD concept is working (Sec. 4.4.1). Unfortunately, due to the movement of the SingleCCD not all of them are feasible, because only relative differences, e.g. the relative difference between Cherenkov camera centre and the star on the lid, are independent of the camera movement. The results of two of the verifications that are feasible, the mechanical model of the SingleCCD (Sec. 4.4.2) and the accuracy of the star fit (Sec. 4.4.3) are presented.

4.4.1. Verification Methods

The aim of the verification is to derive quantities that allow to evaluate the performance of the SingleCCD. It would be ideal to have quantities that can be directly compared to the same values obtained from the two CCDs.

Mechanical Model

An obvious cross-calibration is to create a mechanical model with the SingleCCD (see Sec. 3.2.3) and to compare it with the mechanical model that is obtained with the LidCCD during the same period from the same pointing run data. The mechanical model takes pointing corrections from pointing runs as input, which are calculated from the differences between the pointing star projected on the lid and the Cherenkov camera centre extracted from the LED fit. Both coordinates are affected in the same way by the movement of the SingleCCD, but the difference between two chip positions stays constant.

This verification does not include the fit of the sky. It can only evaluate whether or not the SingleCCD is suited for standard pointing, but not what the performance with respect to the combination of Lid- and SkyCCD is.

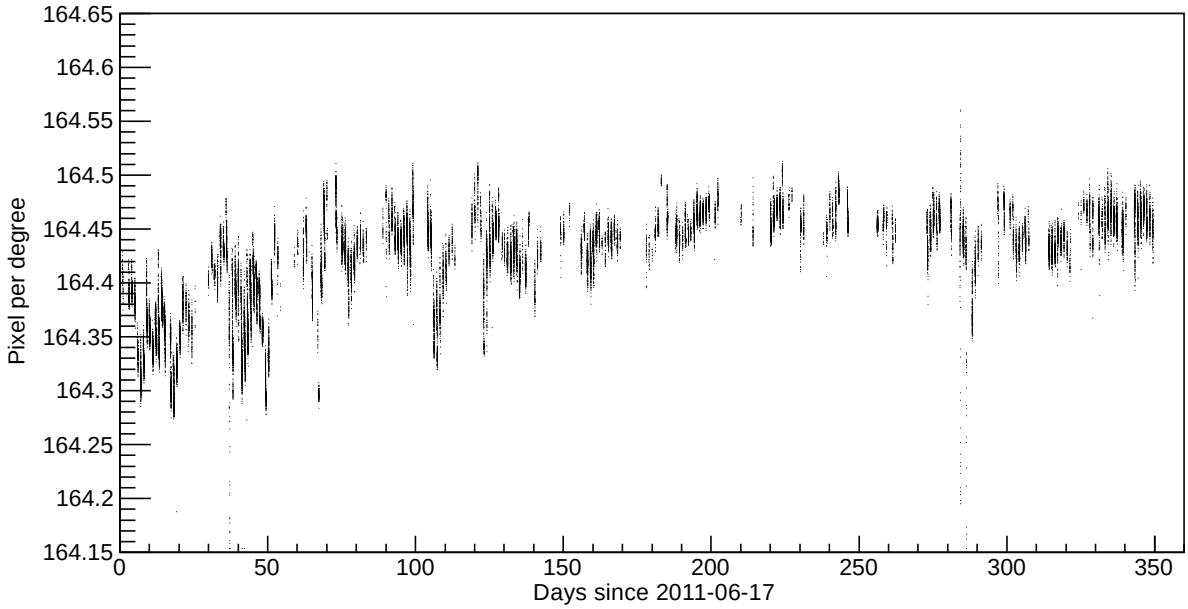

(a) Scale determined from the LED fit.

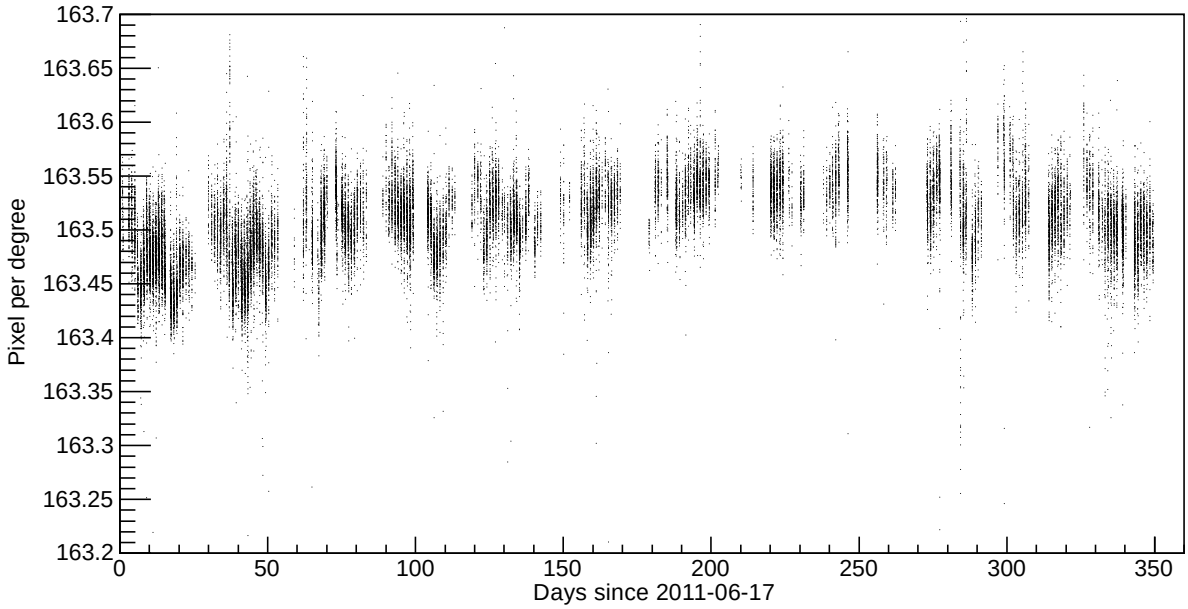

(b) Scale determined from the sky.

Figure 4.7.: Scale (effective focal length) of the SingleCCD as a function of time (observation runs between 64700 and 72428). Each point corresponds to one determination of the scale either from the sky or the LEDs.

Mechanical Model Sky

As discussed in Sec. 3.3.1 it is also possible to fit a mechanical model for the SkyCCD. This model compares the nominal sky with the actual view and the resulting mechanical model should be identical to the one derived in standard pointing, except for bending effects. However, due to the movement of the SingleCCD this does not work without further modelling, because it includes the sky imaged onto the CCD chip in absolute coordinates, which is a function of time.

Modified Mechanical Model Sky

A possibility to counteract the movement of the SingleCCD would be to compare the actual view of the sky with the Cherenkov camera centre, which would again be a relative relationship. The mechanical model would include the bending of the Cherenkov camera, but no effects of the mirror dish. Only with the SingleCCD it is possible to separate these two effects. Unfortunately, it is not straightforward how to compare the results with known quantities from the two CCDs.

SkyLid Model

The ultimate aim to verify the performance of the SingleCCD would be to calculate pointing corrections simultaneously to data taking and compare with the corrections modelled with the two CCDs. This would require a SkyLid model that relates the sky with a position on the lid. A first verification would be to compare the residuals of the SingleCCD SkyLid model to the one derived with the two CCDs.

Unfortunately, the movement of the SingleCCD prevents the creation of a SkyLid model. The reason is that the positions derived from the sky and from the lid are anti-correlated with each other. This means that if e.g. the azimuth axis is tilted the sky and the projection of the star on the lid are affected in opposite directions. Thus also the movement of the SingleCCD affects both in opposite directions and the residuals grow larger with time. The same is also true for the horizontal camera centre jumps for zenith angle observations higher than $45\,^{\circ}$.

Accuracy of Star Fit

All verifications discussed so far that include the fit of the sky are either not straightforward possible due to the movement of the SingleCCD or lack something it can be compared to. However, it is still possible to evaluate the accuracy of the star fit itself, e.g. by looking at the distribution of the residuals of the star positions after applying the fit. The width of this distribution characterises the error of the fit. If the fit of the sky works accurately and the fit of the star on the lid works it can be assumed that also the connection between the two works in principle.

4.4.2. SingleCCD Mechanical Model

Fig. 4.8 shows the mechanical model obtained with the SingleCCD using the same procedure and software that is also used for the LidCCDs. The model reproduces the pointing data nicely. A Gaussian fitted to the residuals in azimuth and altitude has a width of $8\,''$,

which is only marginally larger ($\sim 0.5''$) than the values for the model obtained by the LidCCD.

Figure 4.9 compares the mechanical models obtained by the Lid- and SingleCCD in P2011-08. It can be seen that the differences are very small (on average $2''$). The mean correction is slightly different, which is however expected because the Lid- and SingleCCD are in different positions in the dish. Thus the SingleCCD model is nicely consistent with the LidCCD model obtained with the same data. The lower resolution ($23''$ per pixel compared to $13''$ per pixel) has a negligible influence on the model, as have the bigger spot sizes. This confirms the finding of the CCD replacement that the spot sizes have no major impact on the pointing model.

4.4.3. Accuracy of Star Fit

Figure 4.10 shows a histogram of the distribution of the residuals of the star positions after applying the fit. The width in vertical and horizontal deviation is 0.17 pixels and 0.15 pixels, respectively. This corresponds to an accuracy of $\sim 3.5''$. This value is higher than the corresponding value for the SkyCCD, where the offset can be fitted more accurately than one pixel, which corresponds to $\sim 2.3''$. However, given the systematic uncertainties of precision pointing, which is $6''$ per telescope (see Sec. 3.3.3) it looks like the achieved accuracy should be sufficient.

4.5. Summary

In this chapter a new approach for the H.E.S.S. pointing, the SingleCCD concept, has been introduced and tested. Its main idea is to observe the sky and the Cherenkov camera in parallel with a single CCD camera. Unfortunately, the SingleCCD was not attached firmly enough to the telescope, which leads to a drift of the SingleCCD over time. This further complicates the analysis and precision pointing corrections cannot be calculated straightforwardly.

It has been shown that for the SingleCCD fitting the star on the lid and creating a mechanical model from the pointing runs works to an accuracy of $\sim 2''$. Also the fit of the sky should be accurate to a level of $\sim 4''$. Since the SkyLid model is essentially the connection of these two, it can be expected that also this should work in principle to an accuracy which is not much worse than the accuracy of the H.E.S.S. precision pointing ($6''$) and it may be even better. However, the SingleCCD might have additional systematics that are not yet apparent, so further analysis is needed. Hence, it is not possible to come to a final conclusion on the feasibility of the SingleCCD yet. However, none of the investigations indicated that the SingleCCD concept should not work.

A future analysis could try to correct for the movement of the SingleCCD and the jump of the horizontal camera centre for observations with a zenith angle larger than $45°$. While fitting straight lines to the drift seen in Fig. 4.4 is straightforward, the jump is harder to correct, because the gap between the two levels does not seem to be constant with time. The corrections of these effects will introduce additional systematics and it needs to be seen if they are small enough to still draw final conclusions on the pointing accuracy that can be reached with the SingleCCD.

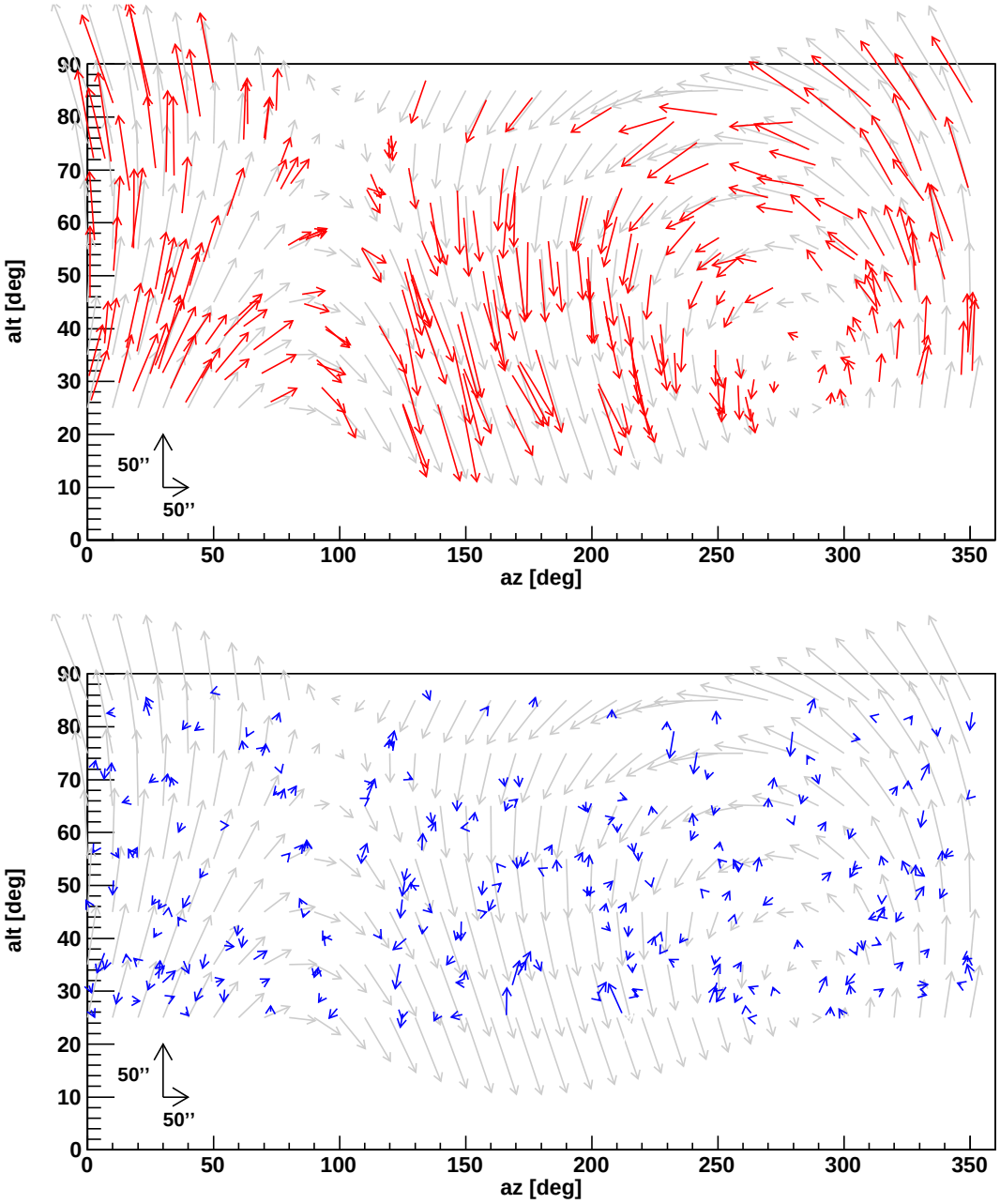

Figure 4.8.: Same plot as Fig. 3.4, but now for P2011-08 and the SingleCCD. The model has very small residuals, the standard deviation of a Gaussian fitted to the magnitude of the residuals is only 5.4″.

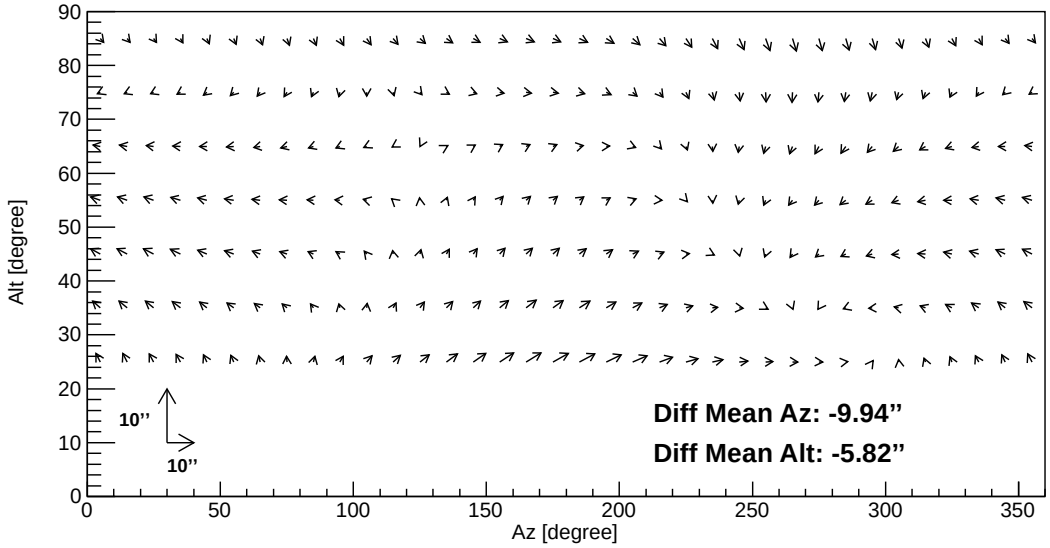

Figure 4.9.: The differences between the pointing correction evaluated at each point for the mechanical models obtained by the Lid- and SingleCCD in P2011-08. Differences are very small, at the level of 2″.

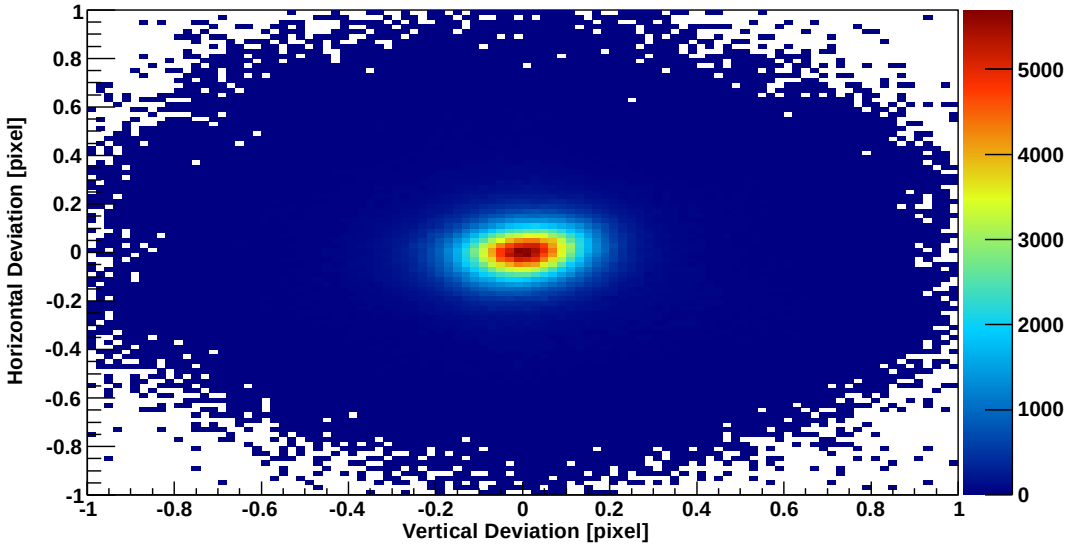

Figure 4.10.: Histogram of the distribution of the residuals of the star positions after applying the fit. All stars lie typically within 0.2 pixels, which shows that the fit is in general accurate.

Chapter 5

Supernovae

In the current and next chapter transient events are investigated for signs of VHE emission. A supernova (SN) explosion marks the spectacular end of a massive star or a stellar remnant and is one of the most energetic phenomena in the known universe. Section 5.1 gives a short introduction to SNe. In the analysis described in this chapter young SNe, within one year after the explosion, are analysed for signs of VHE gamma-ray emission. As a motivation for this search, models in which SNe are capable of producing this emission are discussed in Sec. 5.2. The main idea of the conducted analysis is to compare the H.E.S.S. observation positions to a catalogue of known SN explosions in order to find SNe that are accidentally in the H.E.S.S. field of view during the observation of other targets. To this end a newly published, unified supernova catalogue is used. It will be introduced in Sec. 5.3 together with the results of the comparison to the H.E.S.S. data. The last section discusses the results obtained from the H.E.S.S. analysis and the constraints it sets on the models.

5.1. Overview

The following section starts with a short overview of the standard SN classification scheme. Then the SN explosions mechanisms are briefly discussed as a basis for the models in Sec. 5.2.

5.1.1. Supernova Classification

A systematic search for SNe was initiated by Fritz Zwicky in 1932. It became successful with a newly built 18" Schmidt telescope at Palomar Observatory, when he and his collaborators detected the first SNe. The growing number of detections enabled the classification of SNe, which was an important step towards understanding the physics involved. Minkowski was the first who concluded that there are at least two types of SNe [48]. Classification of SNe is mostly done according to their spectra and started with the presence of hydrogen lines: SNe of type I have no hydrogen lines, while they are strong in SNe of type II. In later years the categories were refined and the currently accepted taxonomy is (see e.g. [49]):

- **Ia**: additional lines of silicon,
- **Ib**: no silicon, additional lines of helium,
- **Ic**: neither silicon nor helium lines.

Also SNe of type II can be further classified by either their spectrum or the light curve, which is the development of the SN brightness over time:

- **IIL**: light curve declines linearly after the maximum,
- **IIP**: light curve exhibits a plateau after the maximum,
- **IIb**: spectrum evolves from a normal type II to that of a type Ib in few weeks,
- **IIn**: very narrow spectral lines.

Some SNe are not typical of their subtype, but show individual peculiarities. Those are marked as peculiar. It is obvious that a detailed SN classification can only be done if the spectrum and light curve are recorded. In many cases this is not the case, typically for distant SNe where a very long exposure is needed to get the spectrum.

5.1.2. Supernova Explosion Mechanisms

Unfortunately the SN taxonomy does not translate directly into a physical classification. The fact that the late time emission of SN of type II can be similar to that of type Ib/c indicates a similar explosion mechanism. The current belief is that all SNe originate from just two explosions mechanisms. SNe of type Ia are thought to originate from thermonuclear reactions of stellar remnants, while SNe of type Ib, Ic and II are believed to explode due to the gravitational collapse of a massive star.

Stellar Evolution

Stars are gravitationally bound plasmas that shine due to the energy released in thermonuclear fusion. They are in hydrostatic equilibrium between the gravitational force and the pressure generated by the energy released in the fusion. In the first stage of their life hydrogen is converted to helium in the so-called hydrogen burning phase. The helium accumulates in the centre of the star, which stops the outward pressure and contracts the core. Hydrogen burning continues outside the core causing the outer layers of the stars to expand, forming a so-called red giant. If the star is more massive than ~ 0.5 solar masses ($M_\odot$), the pressure in the central region will at some point be high enough to start the fusion of helium, which will then again halt the collapse.

For massive stars ($\sim 9M_\odot$) this process repeats several times. In each step the core collapses due to the accumulation of already converted elements in the core and is stabilised by the ignition of a new burning process. Each burning phase creates more massive nuclei and requires higher temperatures and pressures. The burning phases go through hydrogen, helium, carbon, neon, oxygen and silicon burning. This will result in onion like layers, where lighter elements are produced further outwards. The burning ends with the fusion of silicon to ^{56}Ni because the fusion to heavier elements does not release more energy. A further collapse of the material will lead to core-collapse SNe, described below.

Less massive stars will end their lives as so-called white dwarfs. These are objects where the gravitational collapse is prevented by the electron degeneracy pressure. The vast majority are so-called carbon-oxygen white dwarfs that are created if the mass of the initial star is not large enough to start the neon burning. They expel their outer layers,

creating a so-called planetary nebula, until only the core is left. A white dwarf cannot exceed a characteristic mass (called Chandrasekhar limit) of about $1.4\,M_\odot$, because the electron degeneracy pressure will be insufficient to compensate gravity. The white dwarf would have to undergo further gravitational collapse, then evolving e.g. into a neutron star.

Thermonuclear Supernovae

The current consensus is that thermonuclear supernovae are violent explosions of white dwarfs and all models share the same underlying mechanism (first discussed by Hoyle & Fowler [50], more information can be found elsewhere [51]). A carbon-oxygen white dwarf accretes matter, e.g. from a companion in a binary system of stars, and gains mass. The current view is that the white dwarf cannot reach the Chandrasekhar limit, but will experience a phase of runaway carbon and oxygen fusion. Within a few seconds a large fraction of the carbon and oxygen will undergo fusion and the enormous energy release will completely disrupt the star. The astrophysical situation is similar to a classical nova, where a white dwarf also accretes matter from a companion star. However, in the case of a nova, the accreted matter is consumed in a hydrogen fusion on the surface that does not disrupt the star.

This models explains a lot of the observational facts, like the apparent lack of neutron stars in the centre of historical galactic type Ia SNe, the absence of hydrogen in the spectra, because the white dwarf has no hydrogen of its own and the high correlation of their light curves. The correlated light curves led to the introduction of type Ia SNe as "standard candles" into cosmology. An empirical relation was found between the magnitude at maximum and the width of the light curve, the so-called *stretch parameter* or *stretch factor*. The absolute magnitude at maximum was calibrated from nearby SNe in parent galaxies with known distance. When applied to distant SNe, evidence for an accelerated expansion of the universe was found [52].

Core-Collapse Supernovae

During the silicon burning phase a core of nickel and neighbouring elements is produced. Like for white dwarfs it is stabilised by the electron degeneracy pressure until the mass reaches the Chandrasekhar limit. Beyond that limit the pressure in the core is reduced by two processes, causing the collapse of the core to accelerate. Electrons are captured by free protons, which creates neutrons and deleptonises the core. This reduces the degeneracy pressure and the produced electron neutrinos reduce the energy and thereby the temperature in the core. At the same time heavy nuclei are disintegrated by photons, which also requires energy and reduces the temperature in the core. The collapse is halted once the core reaches densities comparable to that of an atomic nucleus by the neutron degeneracy pressure.

Once the inner core has stabilised, the infall of stellar material comes to an abrupt end and further infalling matter bounces off the solid core. This sends a pressure wave outward, which will turn into a shock once it exceeds the local speed of sound. The explosion can be triggered if such a shock goes through the entire star and disrupts it.

Not all details of the shock mechanism are yet uncovered. The initial shock is weakened on its way out because it loses energy by dissociating the nuclei of the infalling material. It

is thus very likely that the prompt shock gets stuck before it can reach the surface. During the deleptonisation copious amounts of neutrinos are produced. Densities are high enough that neutrinos can heat the material sufficiently to revive the shock. Also hydrodynamical instabilities, destroying the spherical symmetry of the star, might play a major role in the explosion. More information on the explosion mechanisms of core-collapse SNe can be found elsewhere [53].

5.2. Scenarios of VHE Emission

This section describes two theoretical predictions for VHE gamma-ray emission from young SNe. First an "internal" acceleration model is described, where cosmic rays are accelerated inside the SN shell. When these particles interact with the expanding SN envelope they should create secondary particles that can decay into VHE photons. The second model considers an "external" acceleration that does not happen inside the shell. Circum-stellar material creates an additional shock and the acceleration might be more efficient than diffusive shock acceleration at a single shock. This could give rise to VHE gamma rays.

The analysis described in the current chapter is mostly exploratory and the models discussed below should serve only as a motivation for the upcoming analysis. They have large theoretical uncertainties and the unknown input parameters can change the flux expectations by orders of magnitude. It is therefore reasonable to conduct the analysis to search for unexpected results.

5.2.1. Inelastic Proton-Proton Collisions

When high energy cosmic rays, e.g. protons, interact with ambient matter the protons can scatter inelastically and produce charged or neutral pions. The neutral pions decay into two photons:

$$\begin{gathered} \mathrm{p} + \mathrm{p} \rightarrow \mathrm{p} + \mathrm{p} + \pi^0 \quad \text{or} \quad \mathrm{p} + \mathrm{p} \rightarrow \mathrm{p} + \mathrm{n} + \pi^+ \\ \pi^0 \rightarrow \gamma + \gamma. \end{gathered} \tag{5.1}$$

In general the kinetic energy of the protons needs to exceed $\sim 280\,\mathrm{MeV}$ for the production of pions. At higher energies also more than one pion can be produced or the protons can be exited and gamma rays are produced in the decay of kaons and hyperons.

From the threshold the cross section for inelastic proton-proton collisions rises quickly with the energy, but then increases only logarithmically above $\sim 2\,\mathrm{GeV}$ so at higher energies it is almost energy-independent. This means in particular that a power-law cosmic-ray spectrum gives a gamma-ray spectrum with approximately the same index. In each interaction the photon carries roughly 10% of the initial energy of the proton. Thus the gamma-ray spectrum follows the proton spectrum, but about a decade lower in energy.

5.2.2. Inner Acceleration

As a result of a core-collapse SN a compact object, like a pulsar or a black hole forms at the centre. These objects are capable of accelerating particles to relativistic energies. It

was first discussed by Berezinsky and Prilutsky in 1977 that the interaction of accelerated protons with the expanding SN envelope can give rise to secondary particles like neutral or charged pions that result in VHE photons and neutrinos [54]. While neutrinos can immediately leave the shell, once the density is low enough for the pions to decay rather than re-interact, transparency for gamma rays sets in at a later stage. The initial idea has been further elaborated by Sato, Silberberg and Shapiro in 1977 [55, 56] and Cavallo and Pacini in 1980 [57]. A lot of attention was drawn to the inner acceleration model after SN 1987A [58, 59, 60, 61, 62]. SN 1987A is special because it exploded in the Large Magellanic Cloud, one of the two satellite galaxies of the Milky Way, and was thus the closest observed SN in modern times. No galactic SN has been observed in the last almost 300 years.

Particle Acceleration

As an introduction the most simple acceleration by a pulsar is discussed, however other acceleration processes (e.g. with a black hole) are also possible. Pulsars are rapidly rotating magnetic neutron stars. They emit magnetic dipole radiation if the spin and dipole axes are misaligned. This radiation can accelerate particles, which was first discussed by Gunn and Ostriker in 1969 [63]. It will carry off angular momentum and cause the pulsar to brake. The energy loss of the pulsar that goes into particle acceleration is given by:

$$L(t) = \lambda L_0 \left(1 + \frac{t}{\tau}\right)^{-2} \quad , \tag{5.2}$$

where λ is the fraction of the total magnetic dipole luminosity L_0 (in erg/sec) that is transferred to accelerated particles and τ the characteristic pulsar braking time. The braking time is characteristic for the pulsar and depends on the initial angular velocity of the pulsar at birth. A well studied pulsar is the one inside the Crab nebula with $\tau \approx 0.4\,\text{years}$. However extremely long time scales ($> 100\,\text{years}$) are also possible. A typical value is $\tau = 1\,\text{year}$.

The frequency of the magnetic dipole radiation can be so low that the acceleration occurs in times that are short compared to the period of the wave. Thus acceleration happens basically at constant phase and since the field strength is high ($\sim 10^6\,\text{G}$) it is highly efficient. Gunn and Ostriker estimate a maximum energy of $1.6 \times 10^{15}\,\text{eV}$ for protons accelerated by the Crab pulsar, but according to their calculations $\sim 1 \times 10^{21}\,\text{eV}$ could also be possible. The cutoff in the proton spectrum is typically so high that it has no influence on the gamma-ray spectrum in the H.E.S.S. energy range. Hence, the cutoff in the proton spectrum will not be further discussed.

A more realistic model of particle acceleration has e.g. been considered in connection with SN 1987A by Gaisser, Harding and Stanev [60]. After the SN explosion the pulsar is surrounded by dense stellar material that should stop the electromagnetic dipole wave. This would create a relativistic, magnetohydrodynamical wind that is separated by a termination shock from the stellar material. At this shock first order Fermi acceleration of electrons and protons can take place.

Pure magnetic dipole radiation would lead to *monochromatic acceleration*, where all particles are accelerated to the same energy. The power-law spectrum of the observed cosmic rays could be formed during the long period of pulsar braking. The other possibility

is *spectral acceleration*, where particles are accelerated directly to a power-law spectrum, e.g. by first order Fermi acceleration. In the following a power-law spectrum of the accelerated protons with an index of -2 is assumed.

Particle Interaction

Three time scales are important for the interaction of the accelerated protons with the SN envelope:

- the moment t_γ from which on the shell becomes transparent for gamma rays,
- the time t_c at which it becomes more likely that accelerated particles lose energy via adiabatic processes instead of nuclear collisions, i.e. when the production of secondary pions starts to cease,
- the time t_π at which the charged pion decay time (depends on their relativistic Lorentz factor γ) becomes less than the time between two nuclear collisions.

The time t_π is only important for the generation of neutrinos from charged pions because neutral pions have a significantly shorter lifetime and decay almost instantly after their creation.

The particle interaction can be most easily understood in a simple analytical model by Sato [55]. The gamma-ray light curve is given by:

$$L_\gamma(t) = \lambda L_0 \left(1 + \frac{t}{\tau}\right)^{-2} \frac{1}{1 - \frac{\sigma_\gamma}{\sigma_n}} \cdot \left[\exp\left(-\frac{\sigma_\gamma}{\sigma_n}\left(\frac{t_c}{t}\right)^2\right) - \exp\left(-\left(\frac{t_c}{t}\right)^2\right)\right] \tag{5.3}$$

where λ is the fraction of the total (proton) energy release L_0 (in erg/s) that is transferred to accelerated particles, τ the characteristic pulsar braking time and σ_γ and σ_n the gamma-ray and nucleon interaction cross section. The terms can be understood as followed:

- Nuclear interactions decrease the proton flux I_p in the envelope. At early times the protons are completely absorbed, but then the envelope becomes more and more transparent:
  $I_p(t) \propto \exp\left(-\left(\frac{t_c}{t}\right)^2\right)$.
- If the proton had an interaction, mesons are created that result in secondary particles, for example neutrinos:
  $I_\nu(t) \propto 1 - I_p(t)$.
- At early times the gamma rays are absorbed, so their flux I_γ is different from the corresponding neutrino flux:
  $I_\gamma(t) \propto \exp\left(-\frac{\sigma_\gamma}{\sigma_n}\left(\frac{t_c}{t}\right)^2\right) - I_p(t)$.
- For the neutrino light curve another modification is needed that takes into account that when the envelope is very dense, the mesons re-interact before they can decay:
  $I_\nu(t) \propto (1 - I_p(t))\left(1 + \left(\frac{t_\pi}{t}\right)^3\right)^{-1}$.

The characteristic times are given by:

- $t_c(M_e, \xi) \approx 10^{6.5} M_e^{1/2} \xi V_9^{-1}$ s from [55],
- $t_\gamma(M_e) = 2.4 \times 10^6 M_e^{\frac{1}{2}}$ s from [54],
- $t_\pi(\gamma, M_e, V_9) = 10^{2.2} \gamma^{1/3} M_e^{1/3} V_9^{-1}$ s from [55],
  $t_\pi(\gamma, M_e, V_9) = 1.9 \times 10^2 \gamma^{1/3} M_e^{1/3} V_9^{-1}$ s from [54],

where M_e is the mass of the ejecta in units of solar masses, V_9 the expansion velocity in units of $10^9 \frac{\text{cm}}{\text{s}}$ and ξ a parameters that describes the deviation from a homogeneous density in the SN envelope. For a uniform density function ξ is about 1, for a centrally condensed distribution ξ has a larger value.

Fig. 5.1 shows the gamma-ray and neutrino light curve for a set of typical parameters ($M_e = 3M_\odot$, $V = 0.1c$, $\xi = 1$, $\tau = 1\,\text{year}$, $\gamma = 1 \cdot 10^6$, $\frac{\sigma_\gamma}{\sigma_n} = 0.2$). It can be seen that the neutrino light curve rises to a plateau, while the gamma-ray light curve starts later due to absorption. Then both curves decay with the same slope. The parameter γ only influences the gamma-ray light curve. It can be seen that this models predicts gamma rays within the first months after the explosion. In the simple analytical model the transparency for gamma rays sets in a little bit earlier than the estimate of t_γ from [54].

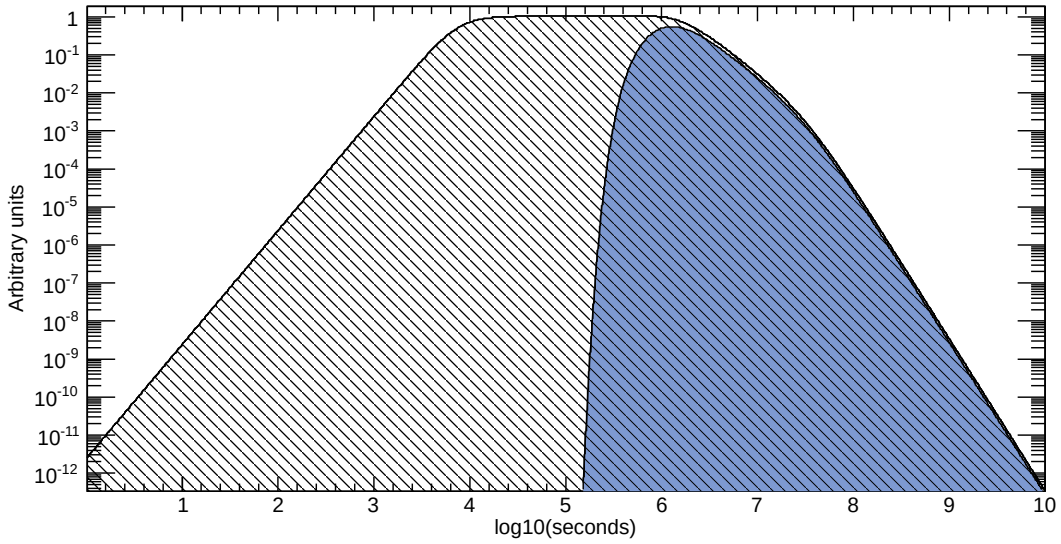

Figure 5.1.: Comparison between the gamma-ray (solid blue) and neutrino (stroked black) light curve for a set of typical parameters in a simple analytical model of inner acceleration. After gamma-ray transparency sets in, emission within the first months after the explosion is expected.

Flux Prediction

The flux prediction for neutrinos is straightforward because it includes only nuclear interactions and photo-pion production. For gamma rays the situation is however more complicated and model-dependent because of absorption. Furthermore, additional photons can also be produced by radiation of accelerated electrons and positrons.

For SN1987 A a flux estimate was made, including only photons from decay of neutral pions and assuming that the nebula is optically thin to the produced photons [60]. For a spectral index of -2 for the power-law spectrum of parent protons the predicted flux is:

$$F(>1\mathrm{TeV}) = 3.5 \cdot 10^{-10} \left(\frac{\lambda \mathrm{L}_0}{10^{40}\ \mathrm{erg\ s^{-1}}} \right) \left(\frac{\mathrm{d}}{50\ \mathrm{kpc}} \right)^{-2} \mathrm{cm^{-2} s^{-1}} \tag{5.4}$$

This is in reach for H.E.S.S. even for an extragalactic SN at a distance d ∼Mpc, if the pulsar is powerful enough. In case the protons have a softer spectrum (e.g. an index of -3) the flux above 1 TeV becomes significantly smaller.

5.2.3. Outer Acceleration

The second model considers SNe that explode into a dense circum-stellar medium. It was first discussed by Berezinsky and Ptuskin [64, 65] that the interaction of the expanding SN envelope with this circum-stellar material could give rise to VHE gamma-ray emission. The acceleration mechanism is less effective for the production of VHE gamma-radiation, than the previously discussed inner acceleration. However, since the production is now at the outer part there is less absorption of gamma rays than if the radiation is produced inside the envelope.

Stellar Winds

All stars emit particles in the form of so-called "stellar winds". Stellar winds are characterised by the mass loss rate ($\dot{M}$) and the asymptotic velocity the wind reaches at a large distance from the star. Luminous, but cool stars (like red giants or supergiants), have slow stellar winds (∼ 10 km/s), but lose large quantities of mass (∼ $10^{-4}\,\mathrm{M_\odot}$/year). Stars initially more massive than $25\,\mathrm{M_\odot}$ will for some time become so-called Wolf-Rayet stars. These stars have lower mass loss rates (∼ $10^{-5}\,\mathrm{M_\odot}$/year), but with much higher velocities (∼ 1000 km/s) [66]. Stellar winds create a so-called planetary nebula in form of a circum-stellar shell. A realistic picture of the surrounding of a star has to be more complex because stellar evolution can have various stages with different sorts of stellar winds. This may cause collisions in the winds and a varying density profile with distance. If a star with a large stellar wind evolves to a core-collapse SN it might have blown away a considerable fraction of the outer hydrogen layer. This can explain the lack of hydrogen lines for type Ib and type Ic SNe.

Particle Acceleration

After the SN shock has left the stellar envelope it will start to interact with the circum-stellar medium and continue as an external shock through the wind region. The compression of the gas at the shock front will create a reverse (or internal) shock. It is travelling inward, however shortly after the explosion it is still dragged outside by the outflowing SN envelope. Between the two shocks a shell forms, which is thin compared to the radius. It contains shocked wind and SN envelope material, separated from each other by a contact discontinuity [67]. The specific feature of this model is that particles can be very effectively accelerated in the thin shell between the two shock fronts.

This model has very successfully reproduced the radio emission of several SNe [68, 69]. Radio supernovae might indicate that the process is particular powerful and are therefore prime targets to search for VHE emission. However, only a handful of radio supernovae have been observed to date and for most SNe the information whether or not it is a radio SN is not available.

The acceleration predicts an E^{-2} spectrum up to a maximum energy and an E^{-1} spectrum beyond that falls of sharply at a break energy [64, 65]. The maximum energy depends on the magnetic field, but is expected to be typically beyond the H.E.S.S. energy range. The change in spectral shape can therefore be neglected in the current analysis.

Flux Prediction

For SN1987 A the flux as a function of observation time t and distance d was estimated [70]:

$$F(>1\text{TeV}) = 2\cdot 10^{-14}\frac{\phi}{f}\left(\frac{\dot{M}}{1\cdot 10^{-5}\ \mathrm{M_\odot year^{-1}}}\right)^2\left(\frac{v_s}{2\cdot 10^4\ \mathrm{km\ s^{-1}}}\right)\left(\frac{v_w}{500\ \mathrm{km\ s^{-1}}}\right)^{-2} \left(\frac{t}{1\ \mathrm{year}}\right)^{-1}\left(\frac{d}{55\ \mathrm{kpc}}\right)^{-2}\mathrm{cm^{-2}s^{-1}}\ , \tag{5.5}$$

where $\frac{\phi}{f} \simeq 1$ is an efficiency factor, $\dot{M}$ the pre-supernova mass loss, v_s the velocity of the external shock driving into the wind region and v_w the velocity of the pre-supernova wind. It can be seen that the flux gets higher if the density of the target material surrounding the star is higher, which can either be achieved by a higher mass loss rate or a lower velocity of the wind. Wolf-Rayet stars are therefore disfavoured for this model because of their high wind velocity. The above estimate is in rough agreement (factor $\sim 4-5$ lower) with the estimates in the original work [64, 65], if one accounts for the difference in the assumed wind speed and distance and sets $\frac{\phi}{f} = 1$.

It was already pointed out for SN 1993J in [70] that a nearby SN (at Mpc distance) with a massive and slow stellar wind ($\dot{M} = 1\cdot 10^{-4}\ \mathrm{M_\odot year^{-1}}$ and $v_w = 10\ \mathrm{km\ s^{-1}}$) might be marginally detectable for H.E.S.S. in an optimistic scenario within the first year after the explosion.

5.3. H.E.S.S. Observations

In this section suitable H.E.S.S. observations that have a SN in the field of view within one year after the SN discovery are selected. To this end a newly published supernova catalogue is used that will be briefly introduced in the first part. In the next part the identified SNe are shown.

5.3.1. A Unified Supernova Catalogue

The work on a new and unified supernova catalogue was triggered by a search for high-energetic neutrinos from young SNe with the AMANDA neutrino telescope [71, 72] and the

result has been recently published [73]. A first reason for a new catalogue was that nearby SNe are most interesting for the analysis, which is also true in the current one. However, especially for these ones the redshift provides a bad distance estimate due to the local flow of galaxies. This can also be seen in Fig. 5.2, which compares the redshift-independent distance to the SN host galaxy and the redshift of the host galaxy. The unified supernova catalogue includes journal-refereed distances, e.g. derived from Cepheid variables or the Tully-Fisher relation, of the host galaxies and therefore allows a more realistic signal estimate. The distances are taken from the NASA/IPAC Master list of galaxy distances[1] (NED-D, version 4.1), which contains 36 411 distances to 9193 galaxies.

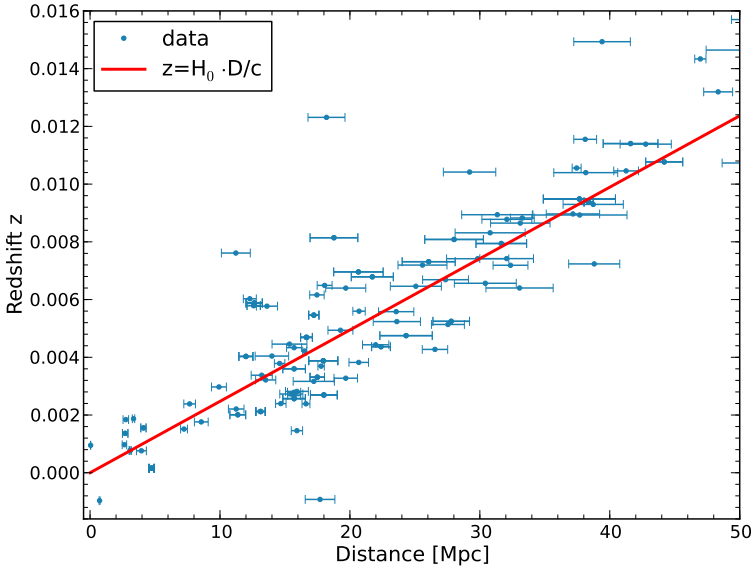

Figure 5.2.: Comparison between the redshift-independent distance to the SN host galaxy and the redshift of the host galaxy, where the red line corresponds to the linear Hubble law ($H_0 = 74.2 \mathrm{km\,s^{-1}\,Mpc^{-1}}$) [73]. Only distances with an absolute error smaller than 10% have been selected for the plot. It can be seen that for nearby SNe the redshift provides only a very rough estimate for the distance.

A second reason for the unified catalogue was that a comparison between the major running SN catalogues available online revealed significant inconsistencies in the listed information. The three major catalogues are the list of SNe maintained by the Central Bureau for Astronomical Telegrams (CBAT)[2], the electronic version of the Asiago SN catalogue (ASC) [74, 75][3] and the electronic version of the Sternberg Astronomical Institute (SAI) SN catalogue (SSC) [76, 77][4]. The differences range from simple typographical errors, to qualitative differences in the data. The unified supernova catalogue tries to resolve inconsistencies in the listed information and adds a flag in case of differences. This allows to use the unified supernova catalogue as a meta-catalogue of the current SN

[1] http://nedwww.ipac.caltech.edu/Library/Distances/
[2] http://www.cbat.eps.harvard.edu/lists/Supernovae.html
[3] http://web.oapd.inaf.it/supern/cat/
[4] http://www.sai.msu.su/sn/sncat/

catalogues and a subset of high-quality SNe with more reliable information can easily be selected with the meta-data.

5.3.2. Comparison to H.E.S.S. Data

The data from the unified supernova catalogue are compared to all pointings of the H.E.S.S. telescopes. An observation is selected based on the following selection criteria:

- SN within 2.5 degree of the nominal H.E.S.S. pointing direction,
- observation time within one year after the SN discovery date,
- SN with known redshift z and $z < 0.01$.

Table 5.1 contains all SNe found with the search criteria and the relevant information listed in the unified SN catalogue. It is striking that the closest SN has a distance below 5 Mpc. This SN has therefore the highest flux estimation and will provide the most stringent limits on the model parameters.

The list contains also two SNe of type Ia. According to the models discussed before, no VHE emission can be expected from them, because SNe of type Ia do not produce a pulsar or are expected to have a large circumstellar envelope. However, since the analysis in this chapter is exploratory the two SNe are investigated as well to search for possible unexpected results.

It should be noted that the SN discovery date is in general not the explosion date, which would be the relevant time scale for the models above. The date of the maximum of the optical SN lightcurve is typically 15-20 days after the explosion. However, for none of the SNe here the date of the optical maximum is known. This indicates that the SNe were discovered after the optical maximum. In the following it is assumed that gamma-ray transparency has already set in at the SN discovery date, so no additional time cut between discovery date and time of the observation is done.

SN	Host galaxy	RAJ2000	DECJ2000	Dist. [Mpc]	Type	Disc. date
2004cc	NGC 4568	$12^{\mathrm{h}}36^{\mathrm{m}}34.40^{\mathrm{s}}$	$+11°14'32.8''$	25 ± 3	Ic	2004-06-10
2004cx	NGC 7755	$23^{\mathrm{h}}47^{\mathrm{m}}52.86^{\mathrm{s}}$	$-30°31'32.6''$	26 ± 5	II	2004-06-26
2004gk	IC 3311	$12^{\mathrm{h}}25^{\mathrm{m}}33.21^{\mathrm{a}}$	$+12°15'39.9''$	17 ± 3	Ic	2004-11-25
2004gn	NGC 4527	$12^{\mathrm{h}}34^{\mathrm{m}}12.10^{\mathrm{s}}$	$+02°39'34.4''$	12.6 ± 0.5	Ic	2004-12-01
2006mr	NGC 1316	$03^{\mathrm{h}}22^{\mathrm{m}}42.84^{\mathrm{s}}$	$-37°12'28.5''$	12.6 ± 0.6	Ia	2006-11-05
2007cj	IC 2531	$09^{\mathrm{h}}59^{\mathrm{m}}55.76^{\mathrm{s}}$	$-29°37'03.3''$	29 ± 6	Ia	2007-05-03
2008bk	NGC 7793	$23^{\mathrm{h}}57^{\mathrm{m}}50.42^{\mathrm{s}}$	$-32°33'21.5''$	4.0 ± 0.4	IIP?	2008-03-25
2008bp	NGC 3095	$10^{\mathrm{h}}00^{\mathrm{m}}01.57^{\mathrm{s}}$	$-31°33'21.8''$	29 ± 6	IIP	2008-04-02
2009js	NGC 918	$02^{\mathrm{h}}25^{\mathrm{m}}48.28^{\mathrm{s}}$	$+18°29'25.8''$	16 ± 3	IIP?	2009-10-11

Table 5.1.: List of nearby SNe that were observed serendipitously by the H.E.S.S. telescopes and relevant data from the unified SN catalogue [73]. A type followed by a question mark means that the type is uncertain.

5.4. Results

The calibration and data preparation of the H.E.S.S. data was already discussed in Sec. 2.4.

Data Quality

The criteria from which suitable observations and telescopes are selected have been described in Sec. 2.4.1. Two separate lists of observations have been prepared, one with good hardware status and one that passes additionally the good weather cut. The first list is used for the detection analysis because the weather has no impact in case signal and background are extracted from the same field of view. For the spectral analysis only the observations taken under good weather conditions are used. This explains differences in the exposure time and average offset for both analysis. For SN 2009js, SN 2007cj and SN 2004gn all data with good hardware status pass the weather cuts as well.

Detection and Spectral Analysis

For each SN a point source analysis with the standard H.E.S.S. analysis software[5] is performed (see Sec. 2.4). The Hillas parameters are used for event reconstruction. For both models an E^{-2} spectrum can be expected and the expected flux is very low. Thus the hard cuts are used for gamma hadron separation with the enhancement of the multivariant cut according to the boosted decision trees [24]. The background is estimated using the reflected background method. Table 5.2 shows the results of the analysis of all available H.E.S.S. data with good hardware status. It can be seen that no significant emission from any individual SN is observed.

It is striking that except for SN 2006mr, which is a type Ia SN and therefore no VHE emission is expected according to the models discussed before, all SNe have a positive significance. Figure 5.3 shows the significance distribution for the core-collapse SNe and a comparison to a Gaussian with mean zero and width one indicates a slight offset between the two.

In order to enhance the sensitivity of the analysis the individual core-collapse SNe (so without SN 2006mr and SN 2007js) are stacked, using also those where the significance cannot be calculated. For this N_{ON} and N_{OFF} are summed and an average α is calculated, taking into account the different exposure time and offsets of the individual observations. The analysis of the stacked sample yields a significance of 3.2, which hints at the indication of emission.

A cross-check analysis using the H.E.S.S. standards cuts for gamma hadron separation with the enhancement of the multivariant cut according to the boosted decision trees [24], which should be less sensitive than the hard cuts used before, has been conducted. A large contribution to the possible signal comes from SN 2004cx and SN 2004gn. In the cross-check analysis the significance drops to 2.2 for SN 2004cx and -0.3 for SN 2004gn. Stacking the results of the analysis of all SNe with standards cuts yields a total significance of 1.5. Furthermore, the result have also been cross-checked with a completely independent

[5] version hap-12-03-pl02

SN	Exp. [h]	Offset [°]	Delay [d]	N_{ON}	N_{OFF}	α	N_{excess}	Signi-ficance
2004cc	26.0	1.9	287	79	3860	0.019	4	0.5
2004cx	68.8	2.2	176	85	4237	0.015	20	2.4
2004gk	26.0	1.4	119	114	3764	0.027	11	1.1
2004gn	7.5	1.5	127	44	1175	0.024	15	2.6
2006mr	17.8	1.2	320	24	669	0.043	-5	-0.9
2007cj	4.3	2.4	143	3	133	0.014	1	—
2008bk	10.7	1.9	142	14	588	0.020	3	0.7
2008bp	4.8	2.1	277	4	222	0.017	0.3	—
2009js	3.8	2.1	14	8	359	0.016	2	—

Table 5.2.: Results of the search for excess photons for the H.E.S.S. SN observations. The column "Exp." gives the deadtime corrected livetime of the used observations, the columns "Offset" and "Delay" the average offset of the SNe from the nominal observation position and the average number of days between the observations and the discovery date of the SN. N_{on} is the number of gamma-ray candidates in the signal region around the SN position and N_{off} the background estimate. When scaled by the normalisation factor α they yield the number of excess events $N_{\mathrm{excess}} = N_{\mathrm{on}} - \alpha N_{\mathrm{off}}$. The significance is only estimated when there are at least 10 counts in the signal region.

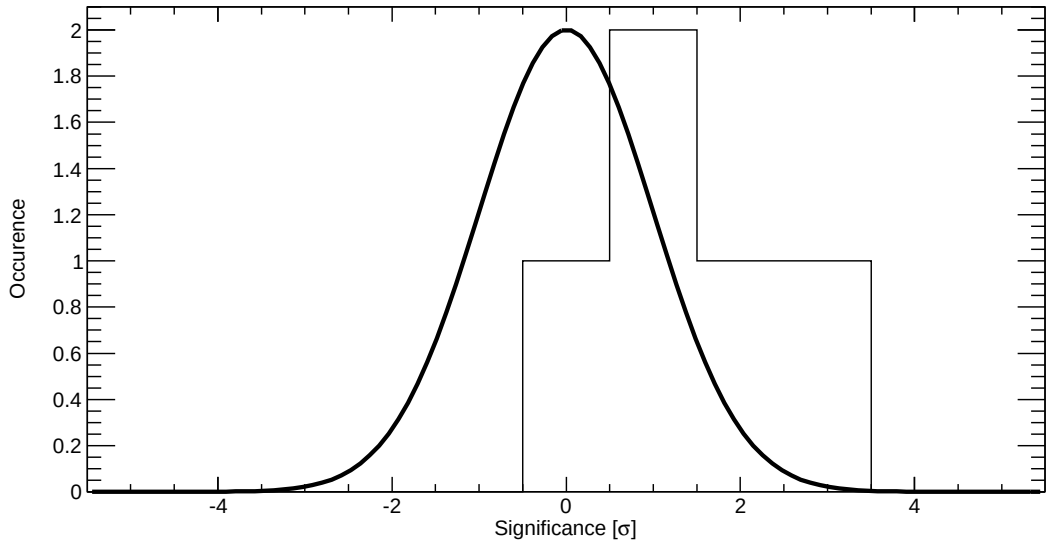

Figure 5.3.: Significance distribution obtained from the number of excess photons for the H.E.S.S. SN observations of core-collapse SNe. To guide the eye a Gaussian with mean zero and width one is added. The two distributions are slightly offset from each other.

calibration and analysis chain of the H.E.S.S. data. In this analysis the significance for SN 2004cx and SN 2004gn is 0.2 and -0.6, respectively.

Given the results of the cross-check analysis it appears that the indication of emission seen in the current analysis is most likely a statistical fluctuation and the results are still compatible with the assumption of no signal. Following the individual non-detections, upper limits on the fluxes are calculated for an E^{-2} spectrum, using the method discussed in Sec. 2.4.7. Table 5.3 shows the spectral results that are obtained.

SN	Exp. [h]	Offset [°]	Delay [d]	E_{th} [TeV]	Flux ULs > 1 TeV $[10^{-13}\mathrm{cm}^{-2}\mathrm{s}^{-1}]$
2004cc	21.8	1.9	288	0.62	1.8
2004cx	42.1	2.3	197	0.42	2.3
2004gk	21.8	1.4	120	0.62	1.7
2004gn	7.5	1.5	127	0.46	4.1
2006mr	2.0	2.0	334	0.51	4.9
2007cj	4.3	2.4	143	0.62	12.0
2008bk	8.1	1.9	136	0.51	4.2
2008bp	4.1	2.1	276	0.46	7.9
2009js	3.8	2.1	14	1.00	12.0

Table 5.3.: Integral flux upper limits for a confidence level of 95 % derived from the H.E.S.S. spectral analysis for an E^{-2} spectrum together with the energy threshold (E_{th}) of the used analysis. The column "Exp." gives the deadtime corrected livetime of the used observations taken under good weather conditions, the average offset of the SNe from the nominal observation position and the average number of days between the observations and the discovery date of the SNe.

Constraints on Models

A strong constraint on the VHE emission from young SNe comes from the non-detection of SN 1987A, which gave a limit of $F(> 3\mathrm{TeV}) = 6.1 \cdot 10^{-12}\mathrm{cm}^{-2}\mathrm{s}^{-1}$ [78]. Fuelled by the non-detection of SN 1987A there has been later work indicating that the flux estimate of the inner acceleration might be too optimistic [79]. However, to date there has been no detection of the pulsar inside the remnant of SN 1987A and a possible explanation is that ejecta falling back on the pulsar converted it to a black hole [80]. The progenitor star of SN 1987A had a strong stellar wind and the non-detection is well in agreement with the flux estimate given for the outer acceleration mechanism. This means that for both acceleration models SN 1987A might not be the typical case and that extragalactic SN might still be brighter in VHE, despite their higher distance.

The flux upper limits from the H.E.S.S. analysis can be used to derive limits on the model parameters. The strongest limits on the model parameters come from SN 2008bk because due to the larger distances the other SNe are less constraining. In the following only the limit for SN 2008bk is discussed using a distance of 4 Mpc and limits for the other SNe can be calculated by simple scaling with the different distances and upper limits.

For the internal acceleration model with a pulsar, the flux upper limit of SN 2008bk yields $\lambda L_0 < 8 \cdot 10^{40}$ erg s^{-1}. This limit is for a young pulsar and the typically observed spin-down luminosity of current pulsars are $4 \cdot 10^{35} - 5 \cdot 10^{38}$ erg s^{-1} [81] for typical pulsar ages of ~ 1000 years. For the Crab pulsar the spin-down luminosity is $4.7 \cdot 10^{38}$ erg s^{-1} and the age of the pulsar is very precisely known from the date of the corresponding SN explosion in 1054 AD, yielding an age of ~ 950 years. Using Eq. 5.2 and a characteristic pulsar braking time of 0.4 years the spin-down luminosity of the young Crab pulsar would be significantly higher than the limit derived here, even if one would assume an efficiency λ of only 0.01. However, Eq. 5.2 might not be appropriate to use in case the pulsar loses energy also via other means than magnetic dipole radiation. Of course the limit is only valid for an assumed spectral index of -2 for the power-law spectrum of the parent protons and a Crab like pulsar cannot be excluded if the spectral index is softer. A definite conclusion on the model needs a detection and measurements of the pulsar properties inside the SN remnant.

There has been a previous analysis searching for neutrino radiation with data from the AMANDA neutrino telescope, where no indication of a signal has been seen [71, 72]. The limit derived in the present analysis on internal acceleration is about three orders of magnitude better than the limit obtained in the previous analysis. However, in the neutrino analysis the limit is obtained from a stacking of sources and a specific model of the lightcurve had to be assumed. So for the analysis of a single source, like the limit presented here, the difference would be even larger.

Using the flux prediction of SN 1987A for the outer acceleration the flux upper limit of SN 2008bk can be expressed as the following limit on the model parameters:

$$\frac{\phi}{f}\left(\frac{\dot{M}}{1 \cdot 10^{-4}\ \mathrm{M_\odot year^{-1}}}\right)^2 \left(\frac{v_s}{2 \cdot 10^4\ \mathrm{km\ s^{-1}}}\right)\left(\frac{v_w}{10\ \mathrm{km\ s^{-1}}}\right)^{-2} < 0.4. \tag{5.6}$$

The given wind parameters can be reached e.g. for asymptotic giant branch stars during the superwind stage [82]. Thus the current limit is only marginally constraining for a very special subclass of progenitor stars and further knowledge about the pre-supernova wind speed and mass loss would be needed to draw definite conclusions on the model.

Summary

The current analysis shows no significant signs of emission for extragalactic SNe observed serendipitously by the H.E.S.S. telescopes, so young SNe cannot be unexpectedly strong emitters of VHE gamma-ray radiation. The derived limits can be interpreted in the proposed models, however without further observational input it is not possible to draw a final conclusion on them. The next generation of Cherenkov telescopes like CTA have a better sensitivity and therefore better chances to detect VHE emission from young SNe. Even for the current generation of Cherenkov telescopes the models could be tested in case a galactic SN would happen.

Chapter 6

Gamma-Ray Bursts

Gamma-ray bursts (GRBs) are transient phenomena of incredibly bright radiation that peaks in the gamma-ray band. They happen randomly in the sky, are to our current knowledge not recurrent and outshine every other gamma-ray source in the sky for the brief time they last. In Sec. 6.1 an overview of the most important observational facts of GRBs is given. The analysis described in the current chapter searches for VHE gamma-ray emission from GRBs. In Sec. 6.2 the currently accepted model for GRBs and in Sec. 6.3 the possibilities for VHE emission are discussed. Section 6.4 describes the H.E.S.S. GRB programme and the GRBs that H.E.S.S. has observed in the last years. In the last section the results of the analysis of this H.E.S.S. data are given.

6.1. Overview

The following section discusses the observational progress in GRB science. Since many key results were obtained with the launch of new satellites, the discussion follows the main missions. In the last part of this section some objects are briefly discussed that are very easily confused with GRBs.

6.1.1. The Early Times

Following the discovery of GRBs in 1967 and the publication in 1973 (see Chapter 1) a lot of dedicated instruments were built to study this exciting new phenomenon and within the next 20 years hundreds of GRBs were discovered. Already with the *Vela* satellites it was possible to triangulate the location of the bursts by comparing differences in the arrival times of widely separated satellites, which showed that they originate from outside of the solar system. Due to their extreme brightness it was hotly debated whether GRBs are galactic or extragalactic phenomena. The bursts are highly individualistic in their time profile and no two GRB are completely alike. They show single or multiple peaks in the light curve that may be clearly separated or overlap. It was already pointed out very early that the duration of the bursts might be used to distinguish different populations of bursts [83].

6.1.2. Burst and Transient Source Experiment

The next major step was the Burst and Transient Source Experiment (BATSE) on board of the *Compton Gamma Ray Observatory* (*CGRO*) flown in 1991. It monitored the sky with an unprecedented sensitivity in the 20 to 1000 keV band and measured about 3000

GRBs at a rate of a about one burst per day. The most important results obtained from the BATSE data are:

Spatial Distribution Due to the high number of GRBs, BATSE could prove with a high confidence level that GRBs are isotropically distributed over the sky [84]. This is very hard to explain if sources in the Milky Way are responsible for the outbursts.

Duration BATSE established the fact that GRBs can be divided into two rough categories [85]. The majority of bursts ($\sim 70\%$) last more than two seconds and are called *long* and those that are shorter are called *short*. The duration of a burst is typically measured by T_{90}, which is the middle time in which 90 % of the counts above background are measured.

Variability BATSE discovered rapid variability on the millisecond scale [86], which indicates that the emission must originate from a very compact region $\leq 1000\,\mathrm{km}$. This is a severe constraint for the modelling (compactness problem, discussed below) because a compact region is highly opaque.

Spectrum The time-integrated spectrum of the GRBs can be characterised by two smoothly connected power laws, known as the Band function [87]:

$$N(E) = \begin{cases} N_0 \left(\frac{E}{E_{\mathrm{ref}}}\right)^{\alpha} \exp\left(-\frac{E}{E_0}\right) & \text{, for } (\alpha-\beta)E_0 \geq E, \\ N_1 \left(\frac{E}{E_{\mathrm{ref}}}\right)^{\beta} & \text{, for } (\alpha-\beta)E_0 \leq E, \end{cases} \tag{6.1}$$

If one multiplies the photon flux with E^2 this function produces a peak at E_{p}, which is directly related to E_0 via: $E_0 = E_{\mathrm{p}}/(\alpha+2)$. The Band function is only an empirical description of the spectra and the shape cannot be deduced from theoretical arguments.

6.1.3. Energetic Gamma-Ray Experiment Telescope

Another instrument on board of the *CGRO* was the Energetic Gamma-Ray Experiment Telescope (EGRET) operating between 20 MeV and 30 GeV. It detected emission from five GRBs above 100 MeV. A spectacular burst was GRB 940217 [88], where the high-energy emission lasted longer than 5400 s (compared to the prompt emission that stopped after $\sim 150\,\mathrm{s}$). Unfortunately the burst was occulted by the Earth for $\sim 4000\,\mathrm{s}$. The highest energy photon (18 GeV) arrived about one hour after the prompt phase was over.

A very interesting burst was GRB 941017, which exhibited a hard high-energy component in addition to the Band function [89]. It is temporally extended and continues after the low-energy component has faded into the background. This rules out explanations by a single spectral component.

6.1.4. BeppoSax

The question about the origin of GRBs was only solved in 1997 with the *BeppoSax* X-ray satellite. Beside a gamma-ray burst monitor it had a narrow-field X-ray telescope. This provides the possibility to promptly slew the telescope and observe the GRB location with

the X-ray telescope. *BeppoSax* discovered a fading X-ray source on longer times scales than the prompt emission from GRB 970228. This emission was called *X-ray afterglow*. The accurate position at the arcmin level was good enough for follow-up observations in the optical and also an *optical afterglow* was discovered [90]. Later the first radio afterglow was detected for GRB 970508 [91], confirming that the afterglow spectrum covers many decades in energy.

GRB 970508 was also interesting because finally spectroscopic observations of the optical counterpart enabled the first redshift measurement [92]. This revealed that the GRB originated at a cosmological distance, ending all discussion about a galactic origin. With the distance the typical energy release in a GRB can be estimated to be $10^{50} - 10^{54}$ erg. The equivalent mass of this energy and the compactness of the source region indicate neutron stars or black holes as candidates for GRB progenitors.

The observation of GRB 980425 was another watershed because the supernova (SN) 1998bw was coincident in time and place [93]. It is interesting to notice that even before the discovery of GRBs it has been suggested that intense emission of prompt gamma rays could occur during the initial stages of the development of a supernova [94]. SN 1998bw was a peculiar, energetic SN of type Ic. The first solid confirmation of the SN-GRB connection was made with GRB 030329 and its associated SN 2003dh. After the optical afterglow of the GRB faded away, broad spectral features of the SN emerged very clearly. These observations might be one of the keys to the explanation of GRB progenitors.

Another open question at the time was whether or not the emission of gamma-ray bursts is isotropic or strongly beamed in our direction. This has important implications, not only for the energetics of the burst, but also for the involved physics of the sources. The observation of GRB 990123 was an important step towards the answer of this question. It was a very bright burst and the energy budget is hard to explain in case of isotropic emission. Furthermore, the afterglow showed spectral breaks in the decay [95]. Such a spectral steepening is expected due to a purely geometric effect, if a beamed emission region continues its radial expansion. Thus this GRB provided the first indication of beamed emission, which today is widely accepted.

6.1.5. Swift

The *Swift* satellite was launched in 2003 and provides excellent multi-wavelength coverage of GRBs. It consists of three main instruments: the wide-field detector for X-ray bursts (Burst Alert Telescope, BAT), the narrow-field X-ray Telescope (XRT) and the UV and Optical Telescope (UVOT). BAT has five times the sensitivity of BATSE and it is used to automatically repoint the space craft in case of a GRB. This provides fast X-ray and optical follow-up observations. The XRT has the capability to pinpoint GRB locations to a few arcseconds.

The fast repointing capability of *Swift* has greatly enhanced the sample of GRBs with known redshift, which can be directly derived from the afterglow spectra. *Swift* was also the first instrument to unambiguously detect the X-ray afterglow from a short GRB, which enabled the accurate localisation of the burst [96]. This enabled more detailed studies of the GRB host galaxies. Together with other follow-up observations this provides important knowledge of GRB progenitors, which will be discussed in more detail in Sec. 6.2.3. Furthermore, *Swift* has shown that the prompt X-ray emission has a smooth

transition into the decaying afterglow. A canonical light curve, an example can be seen in Fig. 6.3, shows a steep and bright afterglow immediately after the prompt emission, followed by a shallow slope, where the flux varies little, but the power-law index of the spectrum changes. Then the so-called classical afterglow follows, where the flux decays with no change in spectral shape. However, not all X-ray afterglows exhibit every of the features.

6.1.6. Fermi

The latest results come from the *Fermi Gamma-ray Space Telescope*. It features two detectors, the Gamma-Ray Burst Monitor (GBM) and the Large Area Telescope (LAT). Both of them are highly relevant for the H.E.S.S. GRB programme, so the detectors are discussed in some more detail in the following.

GBM has 12 NaI scintillators, covering energies between 10 keV and 1 MeV, each looking in different directions. Compton scattering is the dominant interaction process for gamma rays at theses energies, but photoelectric absorption and pair production are also possible. Each scintillator totally absorbs the products of the interaction and produces light from the charged secondary particles. This light is converted with a photomultiplier tube into an electric signal. In order to extend the energy range, two bismuth germanium oxide (BGO) detectors (150 keV to 30 MeV) have been added. Each of them surveys one half of the sky, but they are insensitive to the direction. By combining the signal from different detectors the direction can be reconstructed. The angular resolution is about 3° using sophisticated analysis methods that can only be run on ground-level and not on the spacecraft itself. The limited positional accuracy is a major problem for H.E.S.S. (see discussion in Sec. 6.6).

The LAT is pair production telescope and pair production is the dominant interaction process at energies above $\sim$ 1 MeV. The signature of a pair production, two ionising particles originate from a common point of origin, is relatively easy to detect. However, the electron trajectory is hard to measure precisely, because it will undergo Coulomb scattering, so a better angular resolution is achieved at higher energies. The detector has to be vetoed against charged particles so it is equipped with an anti-coincidence shield. The energy of the gamma ray can be measured by measuring the energy of the electron positron pair and all the secondary particles in a calorimeter. The LAT consists of a silicon strip tracker to reconstruct the particle tracks and a calorimeter which measures energies up to 300 GeV. The angular resolution is about 4° at 30 MeV and 0.2° at 1 GeV.

GBM detects about $\sim$ 250 GRBs per year, however only a very energetic subset of bursts is also detected by the LAT. Both long and short bursts have been seen and preliminary analysis indicates that most bursts show a delayed onset of the high-energy emission (e.g. for GRB 110328B the highest energetic photon arrived more than 500 s after the trigger). Furthermore, the emission seems to be temporally-extended, so the high-energy emission can reach up to 800 s after the burst [97]. For GRB 090902B the highest energetic LAT photon had an energy of 33.4 GeV. Since this burst was at a redshift of 2 this means that $\sim$ 100 GeV photons must be present at the production site. This measurement is important for the GRB modelling (compactness problem, discussed below).

The spectral characteristics of the LAT bursts can be quite diverse (for a summary see e.g. [98]). For some GRBs (e.g. GRB080916C [99]) the emission is a spectral extension of

the keV emission to the 100 MeV range described by a Band function (see Eq. 6.1). Since the Band function is just an empirical description of the spectra this is highly remarkable. Other bursts show an additional hard power-law at high-energies and what appears to be a blackbody thermal component [100, 101]. In the following these bursts will be referred to as "super-bursts". It is yet unclear if these indicate a different subset of bursts or if they originate from differences in the radiation mechanisms.

6.1.7. Source Confusion

There are certain galactic objects that can be easily confused with GRBs. One of them are soft gamma repeaters (SGRs), because they emit bright and repeating flashes of lower energetic gamma-radiation at irregular intervals. It was proposed that SGRs are highly magnetised neutron stars called magnetars. Unlike GRBs, SGR bursts are recurrent from the same position and show a softer spectrum. It took a couple of years to recognise SGRs as a distinct source type and in original literature they are often covered a the same time as "classical" GRBs. The most prominent one is GRB 790305 in the Large Magellanic Cloud, which was known already at the time of discovery to be recurrent. In the following SGRs are not further discussed.

Gamma-ray bursts are often identified by a burst at X-ray energies (e.g. BATSE). This makes them prone to be confused with so-called X-ray bursts [102]. These are X-ray binary stars in our Galaxy that show a recurrent increases in luminosity peaked in the X-ray regime. They are composed of an accreting compact object, which can be a neutron star or a black hole, and a companion star. Depending on the mass of the companion star the system is either categorised as high or low mass X-ray binary (HMXB or LMXB respectively). The bursts are distinguished into two types. A type I burst has a sharp rise time (1-10 s) followed by a slow ($\sim$ 10 s to minutes) decline with spectral softening. This behaviour is similar to the signature a GRB exhibits for an X-ray telescope.

X-ray flashes (XRFs) are a completely different kind of object. They are similar to GRBs, also extragalactic and appear to be correlated with supernova explosions. However, their emission peaks in the X-rays and they have a lower luminosity. Current suggestions are that they might have the same origin as GRBs and are either a lower energetic subset of the same phenomena or the differences are due to their orientation relative to our line of sight [103].

6.2. Gamma-Ray Burst Modelling

After almost 50 years of intensive research, astronomers have started to converge on a model that can successfully explain and predict most of the emission at different wavelengths. There are however still observations, especially for short bursts, that are not yet understood and challenge the currently accepted models.

At the beginning of this section an important constraint to GRB modelling is discussed. Then the today accepted standard model, the so-called fireball model, is briefly presented. In the last part the currently best motivated candidates for GRB progenitors are discussed.

6.2.1. The Compactness Problem

The GRB spectra are of non-thermal origin and photons with energies $\sim 100\,\mathrm{GeV}$ must exist at the production site. This means that a certain fraction of the photons is above the pair-production threshold. The threshold lies always above $2m_\mathrm{e}$ and depends slightly on the mass of the nucleus where the electron positron pair is created. It rises rapidly at the threshold and becomes dominant at about 10 MeV. Then it rises slowly to an asymptotic value, which means that the cross section is energy independent at high energies.

The rapid variability on the millisecond scale indicates that the emission must originate from a very compact region $\leq 100\,\mathrm{km}$. Packing the typical energy released by a GRB into such a small region results in a huge pair-production optical depth. This would immediately thermalise the photons and gamma rays of higher energies would already have been attenuated in the source [104].

A solution to this so-called compactness problem is a relativistic motion of the emitting plasma, e.g. in a jet-like outflow. It is characterised by the Lorentz factor Γ. It eases the compactness problem for two reasons. Firstly, the energy in the photon rest frame is reduced by Γ, so less photons are above the pair-production threshold. Secondly, due to relativistic beaming, the real physical size of the emission region is bigger by a factor Γ^2. The observation of high-energy photons requires an optically thin source and therefore allows to set a lower limit on Γ. This is why observations at the highest energies are particularly interesting to understand GRB modelling.

6.2.2. The Fireball Model

A good review on the fireball model can be found elsewhere [105] and here only the basic ideas are discussed. A fireball is a large concentration of radiative energy in a small region of space caused by an ultra-relativistic outflow. It requires an inner or central engine that starts the fireball. The nature of this central engine is closely related to the question of the GRB progenitors and will be further discussed afterwards. It is only secondary for the discussion here, as long as the central engine is capable of creating the ultra-relativistic outflow.

Most of the GRBs show non-thermal emission, however, also GRBs with a blackbody component exist (see results of *Fermi* above). One possible scenario is that the non-thermal GRB spectra arise from shocks that convert the energy of the fireball into non-thermal radiation, after the fireball has become optically thin (fireball shock scenario, first suggested in [106]). The complicated light curves of the prompt emission are explained by shells of different velocities that collide and dissipate their relative kinetic energy through shock waves. Each collision results in an observed pulse of gamma rays, which requires the central engine to be active and highly variable over some time. In the shock front particle acceleration takes places and high magnetic fields can be realised e.g. due to plasma instabilities. This allows the observed spectra to be explained by synchrotron emission (see also Sec. 6.3.1).

Only a fraction of the kinetic energy of these shells can be converted to radiation. Once the fireball ejecta run into the circum-stellar medium, which could be the interstellar medium or the progenitor wind, an external and reverse shock forms. This is analogous to a supernova explosion as it was discussed in connection with the outer acceleration mechanism in Sec. 5.2. The broad-band multi-wavelength spectrum of the afterglow can

be explained by synchrotron radiation. As the fireball sweeps up material, the external shocks decelerates thus lowering the Lorentz factor. This will result in subsequent softer and longer lasting afterglows.

In summary, the most widely-discussed model that seems to describe the majority of bursts foresees the following steps:

1. central engine creates fireball with ultra-relativistic energy outflow,
2. GRB prompt emission from internal shocks in outflow,
3. GRB afterglow emission from external shocks.

This generic model predicts the GRB radiation to evolve from the burst in gamma rays to the afterglow in X-ray, then UV, optical, IR and radio, which is in good agreement with the observations.

6.2.3. Progenitor Candidates

A lot of effort has been put into the question what the central engine in the fireball model could be. It must be capable of producing the extremely energetic outflow and account for the duration, high variability and complex time structure of some bursts. This suggests that the central engine must be active during some time and disfavours singular explosions.

Swift has shown that the redshift distributions of short and long burst are not consistent [107], which fuels the theory that at least two different source classes are responsible for GRBs. A strong hint to the possible progenitors might come from the associated host galaxies. While long bursts are associated with star-forming regions, short bursts seem to be associated with regions of low star formation, either inside a galaxy or a low star-forming elliptical galaxy. This strongly suggests old stars or stellar remnants as the progenitors of short bursts.

Long Bursts

The connection between SNe and long GRBs has led to the so-called collapsar model [108]. In the original work the collapse of a single Wolf-Rayet star with a high rotational speed to a black hole was considered. The infalling stellar material produces a rotating disk of matter around the black hole. An open question is how the energy from the rotating black hole is extracted and used to create the fireball. One possibility is the Blandford-Znajek process [109], where the energy is extracted by a purely electromagnetic mechanism. Another possibility is the annihilation of neutrino and antineutrino pairs that are created when material falls into the black hole and heats up very strongly.

For rapidly rotating stars the fireball is collimated towards the magnetic field poles and subsequently ejected as highly relativistic jets. The jet can only break through the star surface if it has striped off enough material. This is more likely for massive stars with a high metallicity, like e.g. Wolf-Rayet stars.

Not all SNe and not even all of the most energetic ones (hypernovae) produce GRBs. This could be explained by the requirements on metallicity and rotational speed or by the fact that the jet is not pointing towards Earth. It is yet unclear if all long GRB are

accompanied by a SN. For example for GRB 060614 the limits on a coincident supernova is > 100 fainter than previous detections. This may indicate different populations of long GRBs.

Short Bursts

Short bursts are typically explained by the double degenerate merger scenario [110], e.g. the mergers of white dwarfs, neutron stars or black holes. In a close binary system of massive objects the distance between the objects gets smaller, which is thought to be caused by the radiation of gravitational waves. Eventually the stars become so close that matter can be transferred between the two objects. One of the objects could be disrupted into a accretion disk around the companion. In the final stage the disk falls onto the remaining massive objects within a few seconds, which accounts for the very short duration. A problem for this model are late X-ray flares that have been reported for some short GRBs. They cannot be accounted for in the merger scenario because they happen long after the merge was completed. There has been no detection of a SN associated with a short burst. Again the limits are > 100 times fainter than previous detections.

6.3. Very-High-Energy Emission from Gamma-Ray Bursts

The current section discusses production mechanisms of VHE gamma rays and the prospects of detecting VHE gamma-ray radiation, also taking into account the latest results of the LAT.

6.3.1. Synchrotron and Inverse Compton Emission

Charged particles, e.g. electrons, emit radiation in the interaction with magnetic fields. The characteristic photon energy E_γ of the emission is related to the magnetic field strength B and the energy of the electron E_e by [111]:

$$E_\gamma \simeq 0.2 \left(\frac{B}{10^{-5}\mathrm{G}}\right) \left(\frac{E_\mathrm{e}}{1\mathrm{TeV}}\right)^2 \mathrm{eV}. \tag{6.2}$$

It becomes immediately obvious that high-energy gamma rays cannot by produced with synchrotron radiation. However, it plays nevertheless an important role in astrophysics because it can produce non-thermal emission from radio to X-ray energies in many astrophysical sources (e.g. the prompt the afterglow emission in GRBs as discussed before).

Compton scattering describes the interaction of an electron and a photon, where a certain amount of energy and momentum is transferred after the photon is absorbed and a new photon is emitted. Inverse Compton emission arises when a high-energy electron scatters a low-energy photon to higher energies. It turns out that for many astrophysical objects this is an important production mechanisms of gamma rays around 1 TeV. Here the characteristic photon energy E_γ of the emission is related to incident photon energy E_0 and the energy of the electron E_e by [111]:

$$E_\gamma \simeq 5 \left(\frac{E_0}{10^{-3}\mathrm{eV}}\right) \left(\frac{E_\mathrm{e}}{1\mathrm{TeV}}\right)^2 \mathrm{GeV}. \tag{6.3}$$

The general cross section for this process has to be obtained from relativistic quantum mechanics and is known as the Klein-Nishina formula. It decreases roughly as one over the photon energy. The Klein-Nishina cross section reduces to the constant Thomson cross section ($\sigma_T = 8\pi r_0^2/3$ with $r_0 = e^2/(m_e c^2)$ being the classical electron radius) if the photon and electron energy can be neglected against the electron mass.

Synchrotron self-Compton

An important production mechanism of VHE gamma rays is the combination of synchrotron radiation and the inverse Compton effect, the so-called synchrotron self-Compton (SSC). High energetic electron can first produce photons via synchrotron radiation and then scatter this radiation to TeV energies by the inverse Compton process. Using Eq. 6.2 and 6.3 one can connect the characteristic energies of synchrotron ($E_{\rm sync}$) and inverse Compton photons ($E_{\rm IC}$) produced by the same electrons [111]:

$$E_{\rm sync} \simeq 0.07 \left(\frac{B}{10^{-5}{\rm G}}\right) \left(\frac{E_{\rm IC}}{1{\rm TeV}}\right)^2 {\rm keV}. \tag{6.4}$$

SSC models have also been invoked to explain the prompt emission of some GRBs.

6.3.2. Extragalactic Background Light

An important constraint for the observation of VHE gamma rays comes from the absorption of two gamma rays by photon-photon pair-production. In order to create two particles, each of mass m, for two gamma rays of energy E_1 and E_2 with an angle θ between their trajectories (in the laboratory frame), the energy E_1 has to be above a threshold energy E_{th}, which is:

$$E_{th} = \frac{2m^2c^4}{E_2(1-\cos\theta)}. \tag{6.5}$$

Considering the creation of electrons and head-on collision, the cross section peaks when $E_1 E_2 \sim 2m_e^2c^4 = 0.52\,{\rm MeV}^2$. In an astrophysical setting one is typically interested in the case of few photons of high energy and a high density of lower energetic photons. Depending on the energy of the high-energy gamma ray, different photon fields have to be considered. For a 100 MeV gamma ray, absorption is highest on X-rays (mean energy 1 keV). Apart from the immediate vicinity of X-ray sources, the interstellar and intergalactic X-ray photon densities are small, so absorption can be neglected unless extreme cosmological distances are considered. There is no important radiation field at energies above the X-ray regime, so the mean free path length for gamma rays of lower energies becomes bigger than the Hubble radius, meaning that the universe is effectively transparent.

The situation changes dramatically when going into the 1 TeV energy range, where the cross section peaks at a target photon energy of 0.5 eV. At these energies the universe is full of the so-called extragalactic background light (EBL), which is an accumulated, diffuse radiation coming mostly from star formation. The EBL leads to a significant attenuation over typical extragalactic distances. Since the EBL is energy dependent, the attenuation of a source spectrum is also energy dependent. Figure 6.1 shows the attenuation of the

source flux as a function of energy for the example of an astrophysical sources at a distance corresponding to a redshift of $z \sim 0.5$. It can be seen that at this distance the universe is practically opaque at energies above a few TeV.

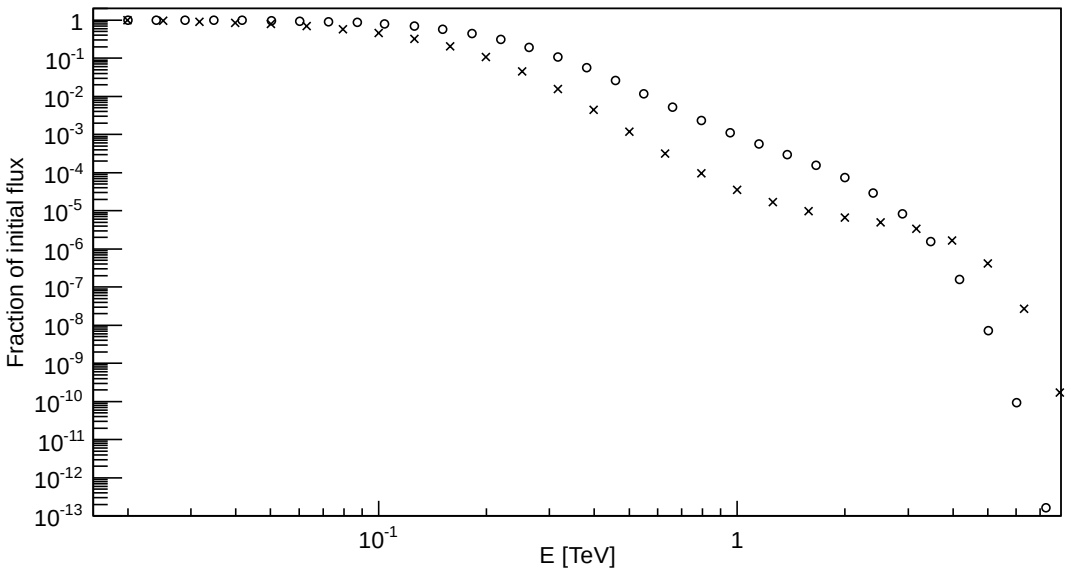

Figure 6.1.: EBL attenuation as a function of energy for an exemplary redshift of $z \sim 0.5$. The open circles show a model calculation by Franceschini et al. [112], while the crosses give an upper limit derived from the observation of distant sources in VHEs (from Aharonian et al. [113]).

Unfortunately, the EBL is difficult to measure directly, so it has to be modelled. One approach is to use the current population of stars in the galaxy and extrapolate their emission backwards in time [112]. A complementary approach is to derive upper limits to the EBL from the observation of high energetic photons from distant sources, assuming a certain intrinsic source spectrum [113].

Since GRBs happen at cosmological distances the absorption due to EBL is severe. It limits the detection of VHE radiation to nearby ($z \ll 1$), powerful GRBs. Observations with a low energy threshold are desirable because EBL absorbtion is more severe at higher energies. This limits observations of IACTs to low zenith angle that have a low energy threshold.

6.3.3. Detection Prospects

In the prompt phase inverse Compton scattering on the prompt GRB radiation, which could have originated from synchrotron emission, SSC or some other mechanism, should give rise to an (additional) inverse Compton peak at higher energies. The peak of the synchrotron emission depends on the Lorentz factor of the relativistic electrons. In the internal shocks the typical synchrotron emission is at 100 keV and the Lorentz factor of the electrons is of the order of a thousand (due to the compactness problem). This would create a second peak in the spectral energy distribution by the SSC mechanism at around

a few hundred GeV [114]. If the afterglow emission is due to synchrotron emission one also expects the afterglow to be accompanied by inverse Compton emission. In some scenarios the energy output in X-ray and VHE radiation should be at a comparable level (e.g. [115]).

GRBs have also been suggested as sources of the highest energy cosmic rays. The accelerated protons could also contribute to a possible VHE signal. Synchrotron radiation by protons is an efficient mechanism of producing TeV photons [116]. When the accelerated protons interact they might produce neutral and charged pions that can decay in VHE gamma rays and neutrinos (see also Sec. 5.2.1). However, recent results show that the neutrino production is much lower than what has been predicted before [117]. This indicates that hadronic scenarios might not be the dominant process for the majority of GRBs.

An empirical estimation of the expected flux in the VHE regime, after applying a suitable EBL model, can be obtained in two different ways. If the Band function is indeed a single spectral component with no cut-off, the simplest approach is to extrapolate the Band function to VHEs. However, such an extrapolation over typically several orders of magnitudes in energy yields a large uncertainty on the estimated flux. Furthermore, the observations of Cherenkov telescopes typically do not cover the prompt phase, but start on the order of $\sim$ 100 s later. The LAT has however shown that most burst have a delayed high-energy onset and that high-energy emission can still be detected on these timescales. Secondly, if the energy output in X-rays and VHE is at a comparable level, a flux estimate can be obtained by comparing with the energy output in X-rays. This has the advantage that VHE data can be recorded during the X-ray afterglow, so both values are obtained simultaneously.

6.3.4. Observation of Gamma-Ray Bursts at Very-High-Energies

It is important to extend the energy range of GRB observations to the VHE regime to further characterise the acceleration mechanisms. For the LAT GRBs that show an extension of the Band function into the high-energy regime, the important question is whether the Band function continues also into the TeV range or if there is a high-energy cut-off. The cut-off would be another parameter for the Band function, which would strongly disfavour it as the correct description. For the LAT super-bursts there has to be a cut-off for the additional hard component due to conservation of energy. Since the cut-off is not in the LAT energy range it has to be in the VHE regime.

Using the empirical flux estimations (e.g. for GRB 100621A, see below), the current generation of IACTs such as H.E.S.S, MAGIC and VERITAS are sensitive enough to detect GRBs under the used assumptions. However, up to now only upper limits on the VHE emission have been reported so far [118, 119, 120]. One reason for this is that nearby and powerful bursts are rare and the observational constraints for IACTs that limit the number of observable bursts.

6.4. H.E.S.S. GRB Programme

IACTs are pointed instruments with a limited field of view and since GRBs happen randomly on the sky the telescopes typically have to be repointed quickly to get VHE

data simultaneously to the prompt and afterglow emission. To date there has been only one completely simultaneous observation with IACTs (GRB 060602B), where the GRB was by chance in the current field of view [121]. No signal was found, neither in the prompt nor afterglow phase. GRB 060602B was an unusually soft burst and there is strong indication that it was indeed a type I X-ray burst [122]. This suggestion is also based on the Galactic position of $l = 1.15°$ and $b = -0.3°$.

6.4.1. Observing Strategy

H.E.S.S. uses triggers for GRB observations provided by the GRB Coordinates Network (GCN)[1] that was established in 1993. It was created for two purposes. First, real time distribution of GRB locations detected by space missions (GCN notices) and second to serve as a platform for the distribution of follow-up observation reports (GCN circulars). The fast distribution of the locations is important to allow rapid follow-up observation. There are various distribution methods, of which the most important ones are TCP/IP based socket connections and e-mail.

The H.E.S.S. data acquisition system is directly connected to the GCN. The notices are received via socket connection and automatically processed on site in Namibia. Currently H.E.S.S. accepts notices on GRBs detected by *Swift*-BAT and *Fermi*-LAT. However, in its three years of operation LAT has only sent out one trigger so far, which was not observable in Namibia. Filtering is applied to select only triggers that are incompatible with known source positions and have a reasonable positional uncertainty and significance. Depending on whether or not the trigger is received during dark time (i.d. night and no moon) and the GRB position can be observed with a zenith angle below 45° to ensure a reasonable low energy threshold, observations are started. Triggers that immediately meet the dark time and zenith criteria are called *prompt* triggers, and all others are called *afterglow* (not to be confused with the prompt and afterglow emission of GRBs). Observations are only started when more than thirty minutes of dark time at good zenith angle are available in that night.

The shift crew on site, which is responsible for the data taking, is alerted of any new GRB trigger in real-time. For prompt triggers the observations should start immediately without delay. Before April 2011 the shift crew had to manually stop the current run, schedule the GRB as new target and start a new run. This human-in-the-loop process was replaced with an automated repointing that automates the necessary steps (more information can also be found in Sec. 6.6). Afterglow observations are only undertaken if the observations would not start too long after the trigger. The delay time for observations after the trigger is redshift dependent, so a longer delay is acceptable for nearby bursts. This is due to EBL absorption because for a nearby burst a lower flux after the initial burst might still be detectable. Therefore, H.E.S.S. is very interested in timely determinations of redshifts. For each trigger per default four observations (runs of nominal length of 28 min) in wobble mode are taken. In case the online analysis shows a hint of a significant signal ($> 3\sigma$) further observations are started.

[1] http://gcn.gscfc.nasa.gov

6.4.2. H.E.S.S. GRB observations

Table 6.1 shows all prompt and afterglow GRB observations of H.E.S.S. since the last publication [118]. GRB 091018 was a prompt alert, but the sky was covered at the beginning of the night so observations could not start immediately. This burst is therefore listed in the afterglow section.

GRB	Trigger number	Trigger time [UT]	RAJ2000 DECJ2000	Error [″]	Fluence [erg cm^{-2}]	T90 [s]	z
120328A	518792	03:06:19 [123]	$16^h06^m27.30^s$ $-39°20'08.3''$	1.9 [124]	$(4.7 \pm 0.6)10^{-7}$ [125]	24.2 ± 6.7 [125]	~ 3.2 [126]
100621A	425151	03:03:32 [127]	$21^h01^m13.12^s$ $-51°06'22.5''$	1.7 [128]	$(2.1 \pm 0.0) \cdot 10^{-5}$ [129]	63.6 ± 1.7 [129]	0.542 [130]
081230	338633	20:36:12 [131]	$02^h29^m19.53^s$ $-25°08'51.8''$	1.8 [132]	$(8.2 \pm 0.8) \cdot 10^{-7}$ [133]	60.7 ± 13.8 [133]	...
080804	319016	23:20:14 [134]	$21^h54^m40.12^s$ $-53°11'05.4''$	1.5 [135]	$(3.6 \pm 0.2) \cdot 10^{-6}$ [136]	34 ± 16 [136]	2.20 [137, 138]
080413A	309096	02:54:19 [139]	$19^h09^m11.59^s$ $-27°40'41.1''$	2.3 [140]	$(3.5 \pm 0.1) \cdot 10^{-6}$ [141]	46 ± 1 [141]	2.43 [142, 143]
070805	287088	19:55:45 [144]	$16^h20^m13.8^s$ $-59°57'26''$	90 [145]	$(7.2 \pm 0.8) \cdot 10^{-7}$ [145]	31.0 ± 1.0 [145]	...
110625A	456073	21:08:28 [146]	$19^h06^m55.85^s$ $+06°45'19.2''$	2.1 [147]	$(2.8 \pm 0.1) \cdot 10^{-5}$ [148]	44.5 ± 10.1 [148]	...
100418A	419797	21:10:08 [149]	$17^h05^m27.18^s$ $+11°27'40.1''$	1.9 [150]	$(3.4 \pm 0.5) \cdot 10^{-7}$ [151]	7.0 ± 1.0 [148]	0.624 [152, 153]
091018	373172	20:48:19 [154]	$02^h08^m44.61^s$ $-57°32'53.7''$	1.7 [155]	$(1.4 \pm 0.1) \cdot 10^{-6}$ [156]	4.4 ± 0.6 [156]	0.971 [157]
090201	341749	17:47:02 [158]	$06^h08^m12.48^s$ $-46°35'25.6''$	1.4 [159]	$(3.0 \pm 0.1) \cdot 10^{-5}$ [160]	83 ± 4 [160]	...
081221	337889	16:21:11 [161]	$01^h03^m10.20^s$ $-24°32'53.1''$	1.4 [162]	$(1.81 \pm 0.03) \cdot 10^{-5}$ [163]	34 ± 1 [163]	2.26 [164]
070920B	291728	21:04:32 [165]	$00^h00^m31.27^s$ $-34°51'10.2''$	8.0 [166]	$(6.6 \pm 0.5) \cdot 10^{-7}$ [167]	20.2 ± 0.2 [167]	...

Table 6.1.: Prompt (upper) and afterglow (lower part) GRB observations by H.E.S.S. between August 2007 and March 2012 after triggers from *Swift*. The given fluence (15-150 keV) and T90 (15-350 keV) is measured by BAT, the position is typically the XRT position. An estimation for the redshift z is not obtained for all GRBs.

Not all possible alerts are actually followed up by H.E.S.S. due to various reasons. Due to weather conditions that did not allow observation two prompt bursts opportunities (GRB 120327A and GRB 100425A) and five afterglow opportunities (GRB 090306B, GRB 090205, GRB 081112, GRB 080218B and GRB 080207) were missed. Some bursts are found in a *Swift* ground analysis and therefore no online trigger is issued, preventing observation of GRB 080702B (prompt) and GRB 101204A, GRB 100203A, GRB 091117 (afterglow). For some bursts no BAT trigger is issued (possible afterglows for GRB 080802 and GRB 110206A, the later one was triggered by *INTEGRAL*). Technical problems, e.g. because the internet connection to the site is interrupted and therefore the trigger is not received, prevented the observation of GRB 080605 (prompt) and GRB 090926B, GRB 090628 (afterglow). The nearby burst GRB 071227 ($z < 0.4$) was missed because no

shift crew was on site to take data. For H.E.S.S. this burst would have been the nearest prompt burst with known redshift. For the afterglow alerts of GRB 100316D (z=0.059) and GRB 090424 (z=0.544) the redshift information was not available before the data taking started that night. GRB 100316D was particularly interesting because the burst was associated with SN 2010bh. Afterglow observations for GRB 081028A were started, but immediately stopped due to bad weather.

6.5. Results

This section presents the results of the analysis of the H.E.S.S. GRB observations. For GRB 100621A a dedicated analysis was done because it was the nearest and brightest burst and therefore the most interesting one from the ensemble. This analysis is presented in the first part. The second part shows the results for the other GRB observations. The calibration and data preparation of the H.E.S.S. data was already discussed in Sec. 2.4.

6.5.1. GRB 100621A

GRB 100621A is in certain aspects the most interesting GRB observed by H.E.S.S. so far. First of all the burst had a very bright prompt phase and it is the brightest X-ray source so far observed by the XRT [168]. Secondly, this burst was the closest prompt burst observed so far by the H.E.S.S. telescopes. It is possible to detect VHE gamma-ray sources even at redshifts above 0.5 so this burst lies within the VHE gamma-ray horizon [169].

Data

H.E.S.S. received the online trigger for GRB 100621A in Namibia at 03:04:01 UT which is 29 s after the *Swift* satellite trigger. However, human intervention delayed the start of the observations to 03:14:55 UT which is 683 s after the trigger. The end of the dark time due to moon rise allowed only two runs with a nominal duration of 28 min. Both runs are taken in wobble mode (see Sec. 2.4.6). The first run was displaced by $-0.5°$ in declination and started at a zenith angle of 31.7°, reaching a final position of 34.6° in the end (mean 32.7°) with a deadtime corrected livetime of 1576 s. For the second run (displaced 0.5° in declination) the zenith angle range was 34.1–37.3° (mean 36.1°) with a livetime of 1574 s. All data were taken during good weather conditions with good hardware status and passed the data quality selection described in Sec. 2.4.1.

The spectrum is an important input for the spectral analysis and can also be used to get an empirical flux estimate in the VHE regime. GRB 100621A was also detected by the Konus instrument on board of the *Wind* satellite. Konus-*Wind* has an extended energy range compared to *Swift* of 20 keV–2 MeV. The extended energy range is better for the extrapolation into the VHE energy range because it reduces the systematic uncertainties. Konus-*Wind* found a fluence of $(3.6 \pm 0.4) \times 10^{-5}$ erg/cm^2 within 74 seconds after the trigger [170]. The time-integrated spectrum of the burst is best fit by a Band function (Eq. 6.1) with the low-energy photon index $\alpha = -1.69^{+0.08}_{-0.07}$, high-energy photon index $\beta = -2.46^{+0.13}_{-0.45}$ and peak energy of the spectral energy distribution $E_\mathrm{p} = 95^{+9}_{-8}$ keV [171]. The quoted errors are at the 68% confidence level.

The redshift of GRB 100621A was derived with the ESO VLT and the X-shooter spectrograph from bright emission lines of the host galaxy [130]. The GRB afterglow shows extreme reddening, which is in strong contrast to the blue host galaxy. This suggests that GRB 100621A exploded in a more dusty environment than what could be expected from the average properties of the host galaxy [172].

Detection and Spectral Analysis

The GRB is analysed using a point source analysis with the standard H.E.S.S. analysis software[2] (see Sec. 2.4). The Hillas parameters are used for event reconstruction. The EBL absorption is estimated using the model by Franceschini et al. [112]. It is interpolated to the GRB redshift and the resulting absorption has already been shown in Fig. 6.1. Figure 6.2 shows the time-integrated Konus-*Wind* spectrum extrapolated into the H.E.S.S. energy range after applying the EBL model. The resulting spectrum is very soft, thus the loose cuts are used for gamma hadron separation with the enhancement of the multivariant cut according to the boosted decision trees [24]. The background is estimated using the reflected background method.

The results of the analysis of the H.E.S.S. data associated with GRB 100621A are shown in Table 6.2. No significant excess is observed for the total dataset. In order to search for emission on shorter time scales and closer to the satellite trigger a further analysis was done on each run separately and the events corresponding to the first 300 s of the first run. Shorter time scales are not possible, because the number of events in the on-region would become too low to estimate the significance. No significant excess is found here either.

	N_{on}	N_{off}	α	N_{excess}	Significance
Total	46	427	0.12	-4	-0.6
First 300 s	8	39	0.13	3	1.2
1^{st} run	26	197	0.13	1	0.3
2^{nd} run	20	230	0.11	-6	-1.1

Table 6.2.: Results of the search of excess photons for the H.E.S.S. data on GRB 100621A. N_{on} is the number of gamma-ray candidates in the signal region around the GRB position and N_{off} the background estimate. When scaled by the normalisation factor α they yield the number of excess events $N_{excess} = N_{on} - \alpha N_{off}$.

Following the non-detection, upper limits on the fluxes are calculated for the time-integrated Konus-*Wind* spectrum after applying the EBL model, using the method discussed in Sec. 2.4.7. The results can be found in Table 6.3. Figure 6.2 shows a graphical representation of the differential upper limit. To illustrate the large uncertainty that comes with the extrapolation into the VHE range, the high-energy photon index β is varied within its one sigma error. This already gives an uncertainty of several orders of

[2] version hap-11-07-pl01

magnitude, without taking into account the errors of the other model parameters and their correlation with β.

	Above E_{th}	Differential at	
		E_{th}	1 TeV
Total	$3.3 \cdot 10^{-10}$	$6.1 \cdot 10^{-11}$	$1.0 \cdot 10^{-13}$
1^{st} run	$5.1 \cdot 10^{-10}$	$9.4 \cdot 10^{-11}$	$1.5 \cdot 10^{-13}$

Table 6.3.: The integral flux upper limit derived from the spectral analysis of the H.E.S.S. data on GRB 100621A for an energy threshold of $E_{\mathrm{th}} = 383$ GeV assuming the EBL absorbed Konus-*Wind* spectrum. The limits are at a confidence level of 95 %. The integral upper limits are also expressed as differential flux upper limits at a certain energy on the assumed spectrum.

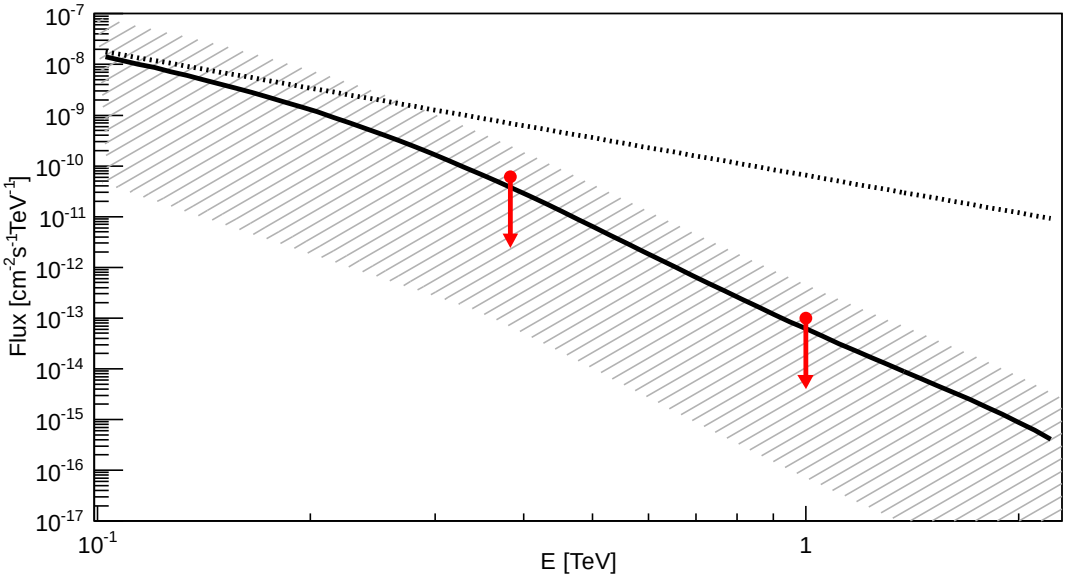

Figure 6.2.: Graphical representation of the results of the H.E.S.S. spectral analysis. The solid line shows the extrapolation of the time-integrated Konus-*Wind* spectrum into the H.E.S.S. energy range after accounting for EBL, while the dotted line shows the unabsorbed power-law. The shaded area shows the effect of varying the high-energy photon index β within its one sigma error. The two red dots are the differential representations of the integral flux upper limit for the analysis of the total data set (from table 6.3).

Interpretation

It can be seen that the H.E.S.S. upper limit is at the level of the extrapolation from the time-integrated Konus-*Wind* spectrum. This seriously constrains the possibility that GRB 100621A has an extra hard power-law like in the LAT super-bursts. This is remarkable because the super-burst were amongst the brightest ones at lower energies and

GRB 100621A was an exceptionally bright burst. However, it has to be taken into account that there is a considerable delay between the Konus-*Wind* spectrum and the H.E.S.S. observations.

Another constraint can be derived by comparing the energy output in the H.E.S.S. and XRT energy ranges (Fig. 6.3). As previously discussed the energy output in X-ray and VHE radiation should be at a comparable level for certain SSC scenarios. GRB 100621A exhibited an extremely bright X-ray afterglow and the H.E.S.S. observations are obtained during the shallow X-ray phase. During this phase the ratio between the energy output in X-ray ($F_{\mathrm{X-ray}}$) and VHE (F_{VHE}) can be constrained to:

$$\frac{F_{\mathrm{X-ray}}}{F_{\mathrm{VHE}}} > 0.4 \tag{6.6}$$

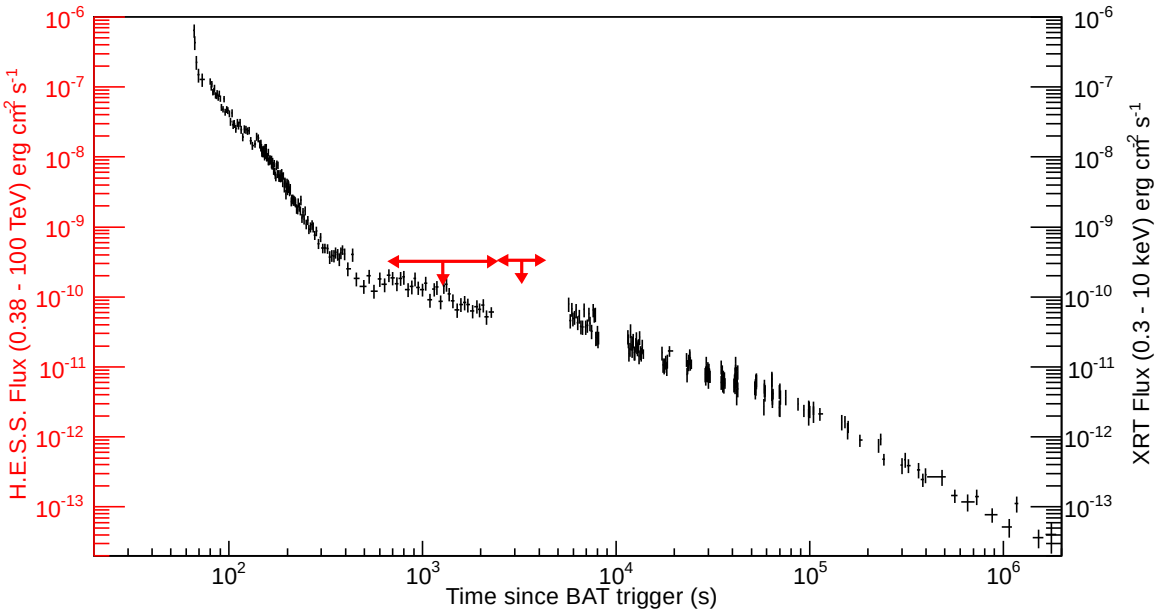

Figure 6.3.: Comparison of the upper limits (95% confidence level) on the energy output above the H.E.S.S. energy threshold (in lighter colour) using the unabsorbed Konus-*Wind* spectrum with the XRT energy flux (in darker colour). The ends of the line indicate the start and end time of the run from which the corresponding upper limit is derived. The X-ray light curve shows the typical canonical behaviour: a steep and bright afterglow directly after the prompt emission, a shallow slope and then the so-called classical afterglow.

The VHE upper limits lie at levels comparable to the X-ray energy flux during the same time. This limit is theoretically interesting, when the afterglow emission is modelled, because it constrains the synchrotron emission.

6.5.2. Other GRBs

For each GRB a point source analysis with the standard H.E.S.S. analysis software[3] is performed (see Sec. 2.4). Event reconstruction is done by using the Hillas parameters.

[3]version hap-12-03-pl02

Due to absorption on the EBL a very soft spectrum is expected for every GRB. Therefore the H.E.S.S loose cuts are used for gamma hadron separation with the enhancement of the multivariant cut according to the boosted decision trees [24]. The background is estimated using the reflected background method.

Data Quality

The criteria that select suitable observations and telescopes for the analysis have been described in Sec. 2.4.1. Two different lists of observations are prepared. The first one includes observations with good hardware status and is used for the detection analysis, because the weather has no impact in case signal and background are extracted from the same field of view. All observations in the second list pass the weather quality criterion and are used for the spectral analysis. For GRB 080804A three runs fail the good weather cut and one run for GRB 091018. All observations of GRB 080413A, GRB 070805 and GRB 070920B were taken under dubious weather conditions.

Detection and Spectral Analysis

Table 6.4 shows the results of the analysis of the H.E.S.S. data associated with the other GRBs from Table 6.1 that have good hardware status. The delays are discussed in more detail in Sec. 6.6. No significant excess is observed in any observation. Unfortunately, the raw data of the first run of the observation of GRB 080413 is corrupted. The analysis covers only the second run (the corresponding delay is listed in brackets). During the observation of GRB 081230 a power fluctuation interrupted the second run. This led to a time gap of approximately 20 min in the observation.

Following the non-detections, upper limits on the flux are calculated, using the procedure discussed in Sec. 2.4.7. For all GRBs an E^{-5} spectrum is assumed and no correction for EBL absorption is applied. Only the observations with good weather are used to reduce systematic uncertainties on the derived flux, which explains the different exposure times compared to Table 6.4. The results are shown in Table 6.5.

Due to their high redshift, the none-detection of some of the GRBs (GRB 120328A, GRB 080804, GRB 080413A and GRB 081221) is not a surprise. Two GRBs are interesting and therefore discussed in some more detail below.

GRB 110625A

This GRB was also triggered by *Fermi*-GBM at 21:08:18.24 UT, which is about the same time as the *Swift* trigger given above. The GRB position was at 88° from the LAT boresight at the trigger time and therefore outside the LAT field of view. However, the burst was bright enough to trigger a *Fermi* autonomous rapid repoint maneuver. This brought the GRB into the LAT field of view between $\sim 100 - 600$ seconds after the GBM trigger. Unfortunately the GRB position reconstructed by the GBM flight software that was used for the repointing is off by 68° from the XRT position, thus resulting in a non-optimal exposure for the LAT follow-up observations [173]. This GRB is one of the few GRBs co-detected by LAT and *Swift*.

The LAT emission shows a double-peaked light curve (first noticed by Tam & Kong [174]). The two emission epochs are roughly 220.9-350.5 s and 424.8-542.8 s after the GBM

GRB	Exp. [h]	Delay [s]	N_{ON}	N_{OFF}	α	N_{excess}	Signi-ficance
120328A	0.5	365	39	297	0.13	1.9	0.3
081230	1.3	1156	85	719	0.12	3.4	0.3
080804	1.8	350	114	705	0.11	15.6	1.6
080413A	0.3	526 (2112)	44	222	0.11	2.3	0.4
070805	0.9	350	44	144	0.12	-3.8	-0.9
110625A	1.3	1267	114	621	0.18	5.0	0.4
100418A	0.9	7975	27	288	0.11	-5.0	-0.9
091018	1.8	7200	45	391	0.11	1.6	0.2
090201	0.9	12848	34	269	0.11	4.1	0.7
081221	0.9	10054	66	463	0.12	11.9	1.5
070920B	1.4	13258	41	370	0.12	-3.6	-0.5

Table 6.4.: Results of the search of excess photons for the H.E.S.S. GRB observations. The column "Exp." gives the deadtime corrected livetime of the used observations and the column "Delay" the time between the GRB trigger and the beginning of the H.E.S.S. data taking. N_{on} is the number of gamma-ray candidates in the signal region around the GRB position and N_{off} the background estimate. When scaled by the normalisation factor α they yield the number of excess events $N_{\mathrm{excess}} = N_{\mathrm{on}} - \alpha N_{\mathrm{off}}$.

GRB	Exp. [h]	E_{th} [TeV]	Flux above E_{th} $[10^{-12}\mathrm{cm}^{-2}\mathrm{s}^{-1}]$
120328A	0.5	0.24	14.9
081230	1.3	0.38	12.6
080804	0.3	0.35	3.5
080413A	—	—	—
070805	—	—	—
110625A	1.3	0.32	11.3
100418A	0.9	0.75	1.9
091018	1.3	0.42	4.4
090201	0.9	0.35	7.7
081221	0.9	0.26	2.2
070920B	—	—	—

Table 6.5.: Integral flux upper limits for a confidence level of 95 % derived from the H.E.S.S. spectral analysis for an E^{-5} spectrum. The column "Exp." gives the deadtime corrected livetime of the used observations taken under good weather conditions. For GRB 080413A, GRB 070805 and GRB 070920B none of the observations passed the weather quality criterion.

trigger [175]. The interpretation of this data is challenging and it seems unlikely that the SSC mechanism of the external forward shock is responsible for the emission. A possible explanation is SSC with an underlying ultraviolet flare [175].

On the H.E.S.S. site GRB 110625A occurred during dark time, but the GRB position was still rising. Approximately 1200 s after the trigger the zenith angle criterion of 45 ° was met and observations were started. The analysis of the source is challenging because a known H.E.S.S. source is nearby (MGRO J1908+06) and there might be possible spill-over. One of the wobble positions makes it impossible to place off regions for the reflected background method that are not affected by this source. Thus only the first and the last two runs can be used with the reflected background method. A cross-check with the ring background method and the full data set also revealed no significant excess. Further analysis of this source is ongoing and will be published elsewhere.

GRB 100418A

This burst, the second closest in the ensemble, exhibited unusual optical and X-ray light curves. The X-ray curve showed the initial short-lived, rapid decline in X-rays, but then the optical and X-ray light curves stayed approximately constant out to at least ~ 7000 s after the trigger. They peak at $\sim 5 \cdot 10^4$ s and then follow a decay which is approximately a power-law [176]. The X-ray flux is however ~ 2 orders of magnitude lower than for GRB 100621A. A possible explanation for the unusual light-curve could be an underlying supernova explosion [177].

6.6. GRB Observations with H.E.S.S. II

As it was already pointed out in Chapter 2, the new H.E.S.S. II telescope will have a lower energy threshold of ≈ 30 GeV. Due to EBL absorption it is important to lower the energy threshold for GRB observations as much as possible. The H.E.S.S. II drive system (with a design speed of about 200 °/min) will allow faster slewing to the GRB position. Even if *Fermi* has shown that GeV emission can be detected for hundreds of seconds after the trigger it is still advantageous to observe the GRB as quickly as possible. In this section two optimisations are briefly discussed to enhance the chances of a GRB detection with H.E.S.S. II.

6.6.1. Follow-up Time

The delay between the satellite trigger and the start of the H.E.S.S. data taking can have various contributions. First of all there is a delay between the satellite trigger and the arrival of the trigger on site. It typically takes below 1 min to downlink the satellite trigger to the ground and the average travel time for a GCN notice to Namibia is below 1 s. However, for example for GRB 120328A the BAT trigger occurred at 03:06:19 UT, but the GCN notice was only issued at 03:10:08 UT. A possible explanation is that *Swift* was transferring the full data for older triggers to the ground (to a station in Malindi, Kenya) in which case the data stream of new triggers is buffered on-board the spacecraft. This is a common problem for H.E.S.S. prompt triggers, affecting $\sim 25\%$ of the triggers and causing delays up to 10 min.

Once the trigger has arrived on site there are two possible delays. One of them is a possible human-in-the-loop that needs to react to the alert. For H.E.S.S. I this delay has been eliminated in April 2011 with an automated repointing procedure that stops the current run, schedules the GRB as the next target and starts a new run. It has been successfully applied in the observation of GRB 120328A. However, this burst was not the typically case, because the alert arrived during a run transition and therefore a run stop was not necessary. An automated repointing procedure will also be used for H.E.S.S. II.

The other delay comes from the technical transition. It includes the time to stop the current run, to slew the telescope to a new target and to start a new run. A previous investigation has already shown that this transition is not optimal in H.E.S.S. and that a considerable amount of time can be saved [178]. This is even more important for H.E.S.S. II because due to the faster drive system the slewing time becomes comparable to the other delays. Work is currently underway to optimise the transition time as much as possible. The main idea is to start and stop the runs while the telescopes are still slewing to the GRB. The aim is to reduce the time apart from the actual slewing to $< 10\,\mathrm{s}$. Finally, the slewing time itself can also be optimised by allowing the telescope to go into "reverse", which means driving the telescope over zenith, so the camera would be upside down.

6.6.2. GBM Triggers

If one uses the current *Swift* trigger rate for GRBs (~ 90 per year) and calculates the expected number of triggers that meet the H.E.S.S. prompt trigger criteria and also accounts for weather conditions that do not allow observations, one arrives at a number of $\sim 2-3$ prompt triggers per year. This estimate is also consistent with the number of GRB observations in Table 6.1. It is known from *Fermi* that less than 10% of the GRBs detected by GBM are also seen by the LAT. Putting these two numbers together it becomes apparent that it might take considerable time until H.E.S.S. observes a GRB with possible emission in the LAT energy regime.

The obvious solution to this problem is to increase the trigger rate, e.g. by also including GBM triggers (~ 250 per year). The problem of the GBM triggers is their large positional error that originates from the reconstruction using the signal in scintillators facing different directions on the sky. Figure 6.4 compares the final GBM position that is available online with the *Swift*-XRT position. It can be seen that a large fraction of bursts would be outside the field of view of an IACT. The difference in position is also divided by the one sigma error of the position provided by GBM. The distribution is more or less Gaussian with some outliers, so it appears that the GBM errors are mostly correct and can be used to cut away badly reconstructed bursts. A final problem is related to the fact that GBM sends out a varying number of flight based positions (1-5 per burst) that are calculated on board of the spacecraft and a varying number of ground based positions (0-3 per burst) using more sophisticated analysis methods. The difference between these positions can be considerable (see e.g. the discussion on GRB 110625A above). Figure 6.4 shows that the first error can be much larger than the field of view of an IACT, even for some of the bright LAT bursts, which is no longer the case for last error.

A new trigger scheme for GBM is currently under development. The main idea is that the tracking position of the telescope will be updated after positional updates in case the

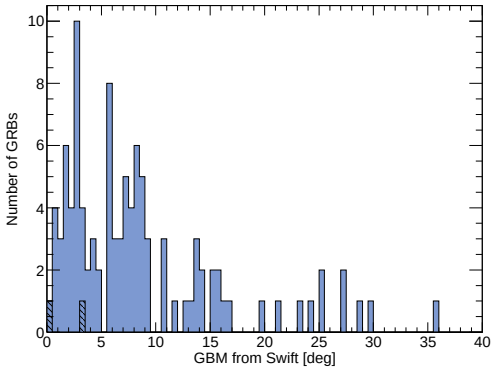

(a) Absolute difference between the last online GBM position and the *Swift*-XRT position. The shaded area shows the burst that were detected by the LAT as well.

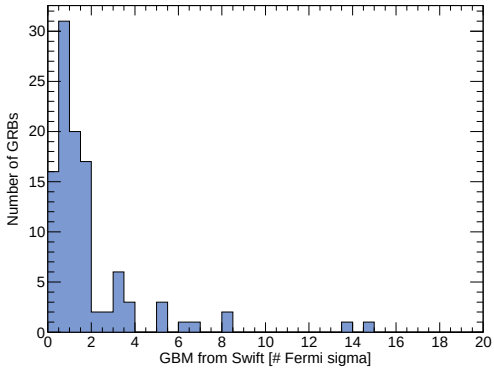

(b) Same plot as (a), but now the difference is scaled by the GBM one sigma error on the position.

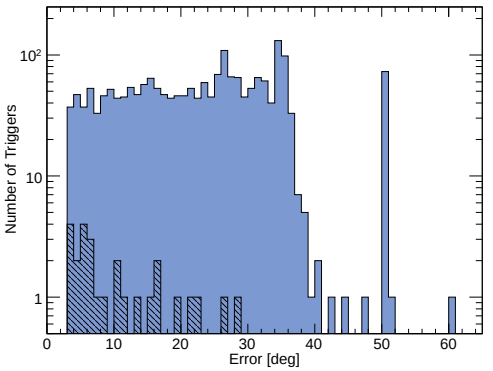

(c) Positional error given in the first GBM notice. The shaded area shows the burst that were detected by LAT as well.

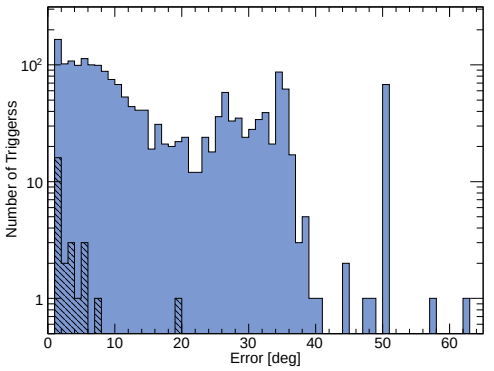

(d) Same plot as (c), but now using the last GBM notice.

Figure 6.4.: Several plots demonstrating the positional accuracy of the GBM triggers. Only the online available information is used, like it would be in a H.E.S.S. trigger.

GRB is not or near the edge of the current observation position.

Chapter 7

Summary and Outlook

Gamma-ray astronomy is an active and vibrant field that has matured to a reliable tool for astronomy in the last years. The energy range covers at least 14 decades and several detection methods are required to cover this huge energy range. Each of them has provided new results that have uncovered important insights into the physics of the sources.

This thesis covered the very-high-energy (VHE, 100 GeV - 100 TeV) regime of gamma-ray astronomy. Data from the High Energy Stereoscopic System (H.E.S.S.) has been used, which is one of the most successful Imaging Atmospheric Cherenkov Telescopes (IACT) to date. The experiment is currently entering its second phase, where the array is extended with a fifth, much larger telescope. This telescope will be the largest Cherenkov telescope ever built, improve the sensitivity and lower the energy range to a threshold that is compatible to the highest energies accessible for space-based instruments.

Data from the H.E.S.S. telescopes have been investigated for transient VHE emission of gamma-ray bursts and supernovae. Supernovae are enormous explosions at the end of the lifetime of massive stars and several models exist, invoking internal or external acceleration mechanisms, that predict VHE emission from young supernovae within one year after the explosion. The H.E.S.S. pointing positions have been compared to a recently created, unified SN catalogue in order to identify suitable SN explosions that are accidently in the field of view during the observation of other targets. Several candidates have been identified and the corresponding data were analysed. None of the SNe showed a significant signal and the results are compatible with the assumption of no signal. For the nearest SN the limit on the internal acceleration model is under certain assumptions quite constraining. However, further information about the SN remnant would be needed to draw definite conclusions on the model.

Gamma-ray bursts easily outshine every other gamma-ray source in the sky for the brief time they last. After almost 50 years of intensive research a standard picture appears to emerge than can successfully explain the majority of bursts. The observation of GRBs in the VHE regime is important to further characterise the acceleration mechanisms and emission models. H.E.S.S. already started to search for VHE gamma-ray emission from GRBs in 2003. In this thesis the GRB observations by H.E.S.S. between August 2007 and March 2012 were analysed. No sign of emission has been found and limits on the VHE emission have been placed. The most interesting limit comes from GRB 100621A, an exceptionally bright and nearby burst. The upper limit lies at the expectation when extrapolating from lower energies, thus constraining the existence of additional long-lasting spectral components that have been observed for some bright GRBs. Furthermore, the limit can constrain emission models and is thus interesting for theoretical modelling of the emission.

The new H.E.S.S. II telescope will have a lower energy threshold. Since absorbtion on extragalactic background light is more severe at higher energies, this will soften the constraint on the observation of distant targets like GRBs. Furthermore, the significantly faster drive system will allow to observe GRBs with a shorter delay, thus enhancing the chances of their detection. In this thesis work has started to reduce the follow-up time as much as possible, e.g. by introducing an automated repointing of the telescope after a GRB alert. Hopefully H.E.S.S. II will enable the detection of GRBs in the VHE range.

In this thesis the telescope pointing was presented as an important technical issue for IACTs. It is necessary to accurately relate the measured images in the Cherenkov camera to the origin in the sky in order to provide the best interpretation of source models and physics when used with data from other wavelengths. H.E.S.S. currently deploys two different methods to correct the telescope pointing. In the standard pointing approach, pointing corrections are measured for different telescope orientations and then used to create a mechanical model that is capable of predicting pointing corrections during data taking. A better accuracy can be achieved using precision pointing, where pointing corrections are modelled simultaneously to the data taking. The pointing corrections need two optical CCD cameras, one that monitors the movements of the Cherenkov camera and one that monitors the sky. During this thesis the necessary software to use CCD cameras on the new H.E.S.S. II telescope has been developed. It has recently been successfully used during the alignment of the H.E.S.S. II mirrors and will soon be used to get pointing data for the new telescope. The software was extensively tested during a replacement of the CCD cameras on the H.E.S.S. I telescopes. It has been shown that the replacement had no negative impact on the H.E.S.S. standard pointing.

A new approach for the H.E.S.S. pointing, the SingleCCD concept, has been developed and tested in this thesis. The main idea is to observe the sky and the Cherenkov camera in parallel. The advantages are that one CCD is saved, which is particularly interesting for the next generation of IACTs that will comprise a large number of telescopes, and that the relative movement between the two CCDs is removed as a systematic uncertainty. However, it also brings certain disadvantages compared to two CCDs, like a larger spot size and a lower resolution of the fitted position. In order to test the performance a SingleCCD has been installed on a H.E.S.S. telescope. Unfortunately, the camera was not attached firmly enough to the telescope, which led to a drift of the camera over time. This makes the analysis significantly harder and further work is needed, e.g. trying to model the drift of the camera. It has however been shown, that the basic principle appears to work and no reason has been discovered why the SingleCCD should not be able to replace the approach with two CCDs.

Acknowledgements

This thesis benefited greatly from the help and support of many people, whom I would like to gratefully acknowledge in the following.
I would like to thank Prof. Werner Hofmann for the opportunity to work with the H.E.S.S. collaboration and the great freedom in choosing my research topics. Additionally, I thank Prof. Stefan Wagner for supporting this thesis and reviewing it as second referee.
I am indebted to Christopher van Eldik for all his help concerning pointing, the SingleCCD and software related problems. He was always there for me and greatly contributed to the success of this thesis. His proofreading significantly improved the quality of the text. I enjoyed our collaboration very much!
Furthermore, I like to thank Wilfried Domainko for his excellent contribution to the physics part of this work. I acknowledge his profound knowledge of astrophysics and thank him for sharing parts of it with me. Our collaboration has been most pleasant for me.
Henning Gast helped me numerous times with software and physics related questions, for which I am truly thankful. Furthermore, his proofreading greatly improved the clarity of the text. I really enjoyed our common time and interesting discussions in Heidelberg!
Special thanks go to Ruth Crespo, for her help in all organisational and official work and supporting me in many issues. She has made bureaucracy less painful.
I would like to thank Paulus Krüger, for investigating certain aspects on pointing and helping me to better understand the SingleCCD.
Jakob Herpich was a great bachelor student and I really enjoyed our collaboration during the early investigations of the SingleCCD.
A special thanks goes also to the "DAQ guys" Arnim Balzer, Anton Lopatin and Daniel Göring for their help with all DAQ related questions and supporting me in creating the CCD controller. They helped immensely in setting up the automatic repointing in case of prompt GRB alerts.
I thank German Hermann for introducing the idea of the SingleCCD and for support during my thesis.
I would like to thank Thomas "Mizzi" Kihm for providing the socket interface for the CCD interface and his help in making it work and fixing bugs.
I appreciate the help from Jörg Baumgart, our team from the workshop, especially Stefan Schmidt, Christian Föhr, Nicolas Hartwig and Tina Frydlewicz. Thanks for building the nice SingleCCD housing, helping me with the electronics and getting things in and out of the country through customs. I thank the local crew in Namibia, above all Toni Hanke and Albert Jahnke, for the support when installing the SingleCCD.
I thank Andreas Förster for support with the CCD cameras in general and in connection with Atilla Abramowski for conducting the CCD replacement.
Yvonne Becherini, Camille Couturier and Jonathan Biteau have provided cross-checks for my results, which I kindly acknowledge here.

Appendix A

CCD Interface

This section briefly describes the different functions in the new CCD interface. Whenever possible, the new functions are similar to the implementation in the old interface [45, 43]. The functions are strongly orientated on the functionality of the Apogee CCDs and other CCDs will require a different implementation.

```
void StartCamera();
```

Starts the camera and gets it ready to execute camera commands. For the Apogee camera this function mainly calls `CApnCamera::InitDriver()`, which claims the USB port where the camera is connected. In case the camera was already started the function just resets the camera.

```
void StopCamera();
```

Stops the camera, which means stopping the driver. For the Apogee camera any ongoing exposure is interrupted and the data are discarded. `StopCooling()` is also called.

```
std::string GetIdentification();
```

Gives back a string stating the model and sensor used in the CCD.

```
int GetFanMode();
```

Returns the current value for the fan mode. For the Apogee CCD the fan mode ranges from zero to three, where zero means the fans are off and three that they are running with maximum speed.

```
void SetFanMode(int fanmode);
```

Sets the fan mode to the given number.

```
float GetTargetTemperature();
```

Returns the temperature the CCD is trying to cool to.

```
float GetCCDTemperature();
```

Returns the current temperature of the CCD ship.

```
float GetHeatsinkTemperature();
```

Returns the current temperature of the heat sink that is used by the Peltier element.

```
bool GetCoolerEnable();
```

Returns if the Peltier element is active.

```
void SetTargetTemperature(float target_temperature);
```

Sets the temperature, the CCD is trying to cool to, to the given number.

```
void SetCoolerEnable(int cooler_enable);
```

Enables or disables the Peltier element. To spare the CCD chip from mechanical stress this function should only be called if the CCD chip temperature is close to the temperature of the heat sink.

```
void StartCooling();
```

Sets the fan to maximum speed and enables the Peltier element.

```
void StopCooling();
```

Stops the fan and sets the desired CCD chip temperature to the temperature of the heat sink. This gradually warms the chip, so the chip is not exposed to mechanical stress that would happen if the cooling would just be disabled (active warming, see also [43]).

```
void TakeImage(float duration, int shutter_open,
               unsigned short xMin = 0, unsigned short yMin = 0,
               unsigned short xMax = 0, unsigned short yMax = 0,
               unsigned short xBinning = 1,
               unsigned short yBinning = 1);
```

Starts an exposure with the specified duration with open or closed shutter. The x and y coordinates are used to specify the region of interest. In case `xMax` or `yMax` is bigger than the CCD chip, the maximum values are used. It is checked whether the requested binning mode is supported by the camera. One important difference to the old interface is that TakeImage does now only start the exposure. During the exposure the camera can do other commands (like e.g. `GetCCDTemperature`). In typical user situations however, `TakeImage` and `GetImage` will always be called one after another.

```
unsigned short* GetImage();
```

Gets the image from the camera and stores it in an image buffer. The dimensions in x and y of the buffer can be read with the functions `GetLastPictureX()` and `GetLastPictureY()`. Since the pictures are usually in counts, only a function giving back an array of unsigned shorts was implemented, in contrast to the original interface.

```
bool GetIsExposing();
```

Returns if the camera is currently taking an image.

```
bool GetImageReady();
```

Returns if an image is ready and could be readout with `GetImage()`.

```
void DiscardExposure();
```

Stops the ongoing exposure and discards the data.

```
unsigned short GetLastPictureX();
unsigned short GetLastPictureY();
```

Since the function `GetImage()` returns only a buffer, these functions return the corresponding image dimensions in x and y.

```
  unsigned short GetMaxBinningX();
  unsigned short GetMaxBinningY();
  unsigned short GetMaxPixelX();
  unsigned short GetMaxPixelY();
  unsigned short GetNumberOfBits();
```

These functions can be used to query information about the camera, like the binning or the maximum chip size.

Appendix B

CCD Controller

This section briefly describes the main functions in the new CCD controller.

```
ConfigureHardware();
```

This function is called from the DAQ in the initialising step and is called once per DAQ start. Here the generic CCD camera object is created and the camera is started. The camera address and some default values for the exposure are read from a database. Cooling is stopped, but may get re-enabled later.

```
Configuring();
```

This function is called before each run. The exposure time is reset to the default from the database. Then the optimal exposure for the current run is determined by calling `GetExposureTime()`. This is needed for the LidCCD in pointing runs and the SkyCCD in all runs.

```
Starting();
```

In this function a flag is set to signal `ProcessEvent()` that pictures should be taken. During a pointing run the pictures are taken in `Starting()`, because we want exactly two LidCCD pictures with different frames and exposure times and ten SkyCCD images.

```
Stopping();
```

Deactivates the flag set by `Starting()`.

```
ProcessEvent();
```

This is the main function that is called continuously and has two main tasks. It is continuously checked whether or not the sun is below the horizon. Cooling is initiated once this conditions is fulfilled, so the cameras have finished their cooling before the data taking starts in the dark time. After the night the cooling is stopped and the Peltier element is deactivated if the chip has sufficiently warmed up. The second task is taking images in case `Starting()` was called before.

```
TakeImage();
```

This function takes the actual image and also runs a spot analysis. For the SkyCCD a check is done if stars are seen and the exposure time is changed in case there are no, not bright enough or too bright spots.

```
GetExposureTime();
```

An estimate for the exposure time is not needed for the LidCCD in observation runs, because the exposure time is fixed. For the SkyCCD or the LidCCD in pointing runs this function reads the current target specified for the drive system. In pointing runs the target is always a star, so its magnitude can be directly read from a database. For observation runs the brightest star in a 0.6° square around the target position is searched. The predetermined reference values from the database are then used to calculate the optimal exposure time.

Bibliography

[1] V. F. Hess, *Über Beobachtungen der durchdringenden Strahlung bei sieben Freiballonfahrten*, Physik. Zeitschr., **13** (1912), pp. 1084–1091

[2] M. Amenomori et al., *Anisotropy and Corotation of Galactic Cosmic Rays*, Science, **314** (2006), pp. 439–443

[3] J. W. Cronin, T. K. Gaisser & S. P. Swordy, *Cosmic Rays at the Energy Frontier*, Scientific American, **276** (1997), pp. 32–37

[4] W. Baade & F. Zwicky, *Cosmic Rays from Super-novae*, Proceedings of the National Academy of Science, **20** (1934), pp. 259–263

[5] R. W. Klebesadel, I. B. Strong & R. A. Olson, *Observations of Gamma-Ray Bursts of Cosmic Origin*, ApJ, **182** (1973), p. L85

[6] W. H. Heitler, *The Quantum Theory of Radiation*, Oxford University Press, 1954, 3 ed.

[7] K. Bernlöhr, *Simulation of imaging atmospheric Cherenkov telescopes with CORSIKA and sim_telarray*, Astroparticle Physics, **30** (2008), pp. 149–158

[8] F. Aharonian et al., *Energy Spectrum of Cosmic-Ray Electrons at TeV Energies*, Physical Review Letters, **101** (2008), no. 26, 261104

[9] T. C. Weekes et al., *Observation of TeV gamma rays from the Crab nebula using the atmospheric Cerenkov imaging technique*, ApJ, **342** (1989), pp. 379–395

[10] J. Albert et al., *VHE γ-Ray Observation of the Crab Nebula and its Pulsar with the MAGIC Telescope*, ApJ, **674** (2008), pp. 1037–1055

[11] J. Holder et al., *The first VERITAS telescope*, Astroparticle Physics, **25** (2006), pp. 391–401

[12] J. A. Hinton, *The status of the HESS project*, New A Rev., **48** (2004), pp. 331–337

[13] J. M. Davies & E. S. Cotton, *Design of the quartermaster solar furnace*, *Solar Furnace Symposium*, vol. 1 of *Solar Furnace Symposium*, 1957 pp. 16–22

[14] K. Bernlöhr et al., *The optical system of the H.E.S.S. imaging atmospheric Cherenkov telescopes. Part I: layout and components of the system*, Astroparticle Physics, **20** (2003), pp. 111–128

[15] R. Cornils et al., *The optical system of the H.E.S.S. imaging atmospheric Cherenkov telescopes. Part II: mirror alignment and point spread function*, Astroparticle Physics, **20** (2003), pp. 129–143

[16] S. Funk et al., *The trigger system of the H.E.S.S. telescope array*, Astroparticle Physics, **22** (2004), pp. 285–296

[17] F. Aharonian et al., *Observations of the Crab nebula with HESS*, A&A, **457** (2006), pp. 899–915

[18] F. Aharonian et al., *Calibration of cameras of the H.E.S.S. detector*, Astroparticle Physics, **22** (2004), pp. 109–125

[19] P. K. MacKeown et al., *Primary Cosmic Ray Spectrum above* 10^{12} *eV from Cerenkov Light Images*, *International Cosmic Ray Conference*, vol. 9 of *International Cosmic Ray Conference*, 1983 pp. 175–178

[20] A. M. Hillas, *Cerenkov light images of EAS produced by primary gamma*, F. C. Jones, ed., *International Cosmic Ray Conference*, vol. 3 of *International Cosmic Ray Conference*, 1985 pp. 445–448

[21] M. Ulrich et al., *An improved technique for the determination of shower geometry from single and stereo IACT images*, Journal of Physics G Nuclear Physics, **24** (1998), pp. 883–897

[22] S. Le Bohec et al., *A new analysis method for very high definition imaging atmospheric Cherenkov telescopes as applied to the CAT telescope.*, Nuclear Instruments and Methods in Physics Research A, **416** (1998), pp. 425–437

[23] W. Hofmann et al., *Comparison of techniques to reconstruct VHE gamma-ray showers from multiple stereoscopic Cherenkov images*, Astroparticle Physics, **12** (1999), pp. 135–143

[24] S. Ohm, C. van Eldik & K. Egberts, *γ/hadron separation in very-high-energy γ-ray astronomy using a multivariate analysis method*, Astroparticle Physics, **31** (2009), pp. 383–391

[25] T.-P. Li & Y.-Q. Ma, *Analysis methods for results in gamma-ray astronomy*, ApJ, **272** (1983), pp. 317–324

[26] D. Berge, S. Funk & J. Hinton, *Background modelling in very-high-energy γ-ray astronomy*, A&A, **466** (2007), pp. 1219–1229

[27] V. P. Fomin et al., *New methods of atmospheric Cherenkov imaging for gamma-ray astronomy. I. The false source method*, Astroparticle Physics, **2** (1994), pp. 137–150

[28] O. Bolz, *Absolute Energiekalibration der abbildenden Cherenkov-Teleskope des H.E.S.S. Experiments und Ergebnisse erster Beobachtungen des Supernova-Überrests RX J1713.7-3946*, Ph.D. thesis, Ruperto-Carola University of Heidelberg (2004)

[29] W. A. Rolke, A. M. López & J. Conrad, *Limits and confidence intervals in the presence of nuisance parameters*, Nuclear Instruments and Methods in Physics Research A, **551** (2005), pp. 493–503

[30] S. Gillessen, *Sub-Bogenminuten-genaue Positionen von TeV-Quellen mit H.E.S.S.*, Ph.D. thesis, Ruperto-Carola University of Heidelberg (2004)

[31] I. Braun, *Improving the Pointing Precision of the H.E.S.S.-Experiment*, Ph.D. thesis, Ruperto-Carola University of Heidelberg (2007)

[32] J. Herpich, *Testing a Single-CCD-Concept for the H.E.S.S. II Pointing*, Bachelor's thesis, Ruperto-Carola University of Heidelberg (2010)

[33] ESA, *The HIPPARCOS and Tycho Catalogues*, ESA SP-1200, (1997)

[34] N. Devillard, *The eclipse software*, The messenger, **87** (1997)

[35] S. Gillessen, *Überwachung der Abbildung eines Cerenkov-Teleskops und automatische Spiegeljustierung mit einer CCD-Kamera*, Diploma's thesis, Ruperto-Carola University of Heidelberg (1999)

[36] A. Molenaar, *Analysis of images from a H.E.S.S. 'lidCCD' camera: influences on center finding precision*, Internship report, Twente University (2005)

[37] F. James & M. Roos, *Minuit - a system for function minimization and analysis of the parameter errors and correlations*, Computer Physics Communications, **10** (1975), pp. 343–367

[38] G. Pühlhofer et al., *Locating TeV gamma-ray sources with sub-arcminute precision: the pointing calibration of the HEGRA system of Imaging Atmospheric Cherenkov Telescopes*, Astroparticle Physics, **8** (1997), pp. 101–108

[39] G. Pühlhofer, *TeV-γ-Emission des Supernova-Überrestes Cassiopeia A : Erster Nachweis mit dem HEGRA-Cherenkov-Teleskop-System*, Ph.D. thesis, Ruperto-Carola University of Heidelberg (2001)

[40] G. Pühlhofer et al., *The technical performance of the HEGRA system of imaging air Cherenkov telescopes*, Astroparticle Physics, **20** (2003), pp. 267–291

[41] F. Acero et al., *Localizing the VHE γ-ray source at the Galactic Centre*, MNRAS, **402** (2010), pp. 1877–1882

[42] E. J. Groth, *A pattern-matching algorithm for two-dimensional coordinate lists*, AJ, **91** (1986), pp. 1244–1248

[43] J. Dreyling-Eschweiler, *Aufbau und Test eines neuartigen CCD-Kamerasystems zur Kontrolle der Optik eines H.E.S.S.-Cherenkovteleskops*, Diploma's thesis, University of Hamburg (2010)

[44] Kihm, T. (MIZZI Computer Software), *STCP-Simple TCP Communication* (2008)

[45] A. Petz, *Entwicklung einer CCD-Kameraschnittstelle für das H.E.S.S.-Projekt und Untersuchung der Deformation des Spiegelträgers des ersten H.E.S.S.-Teleskops*, Diploma's thesis, University of Hamburg (2002)

[46] P. Krüger, *Talk at H.E.S.S. Collaboration Meeting, Leicester* (2012)

[47] P. Krüger, *Talk at Weekly H.E.S.S. Meeting at MPIK* (2012)

[48] R. Minkowski, *Spectra of Supernovae*, PASP, **53** (1941), p. 224

[49] M. Turatto, *Classification of Supernovae*, K. Weiler, ed., *Supernovae and Gamma-Ray Bursters*, vol. 598 of *Lecture Notes in Physics, Berlin Springer Verlag*, 2003 pp. 21–36

[50] F. Hoyle & W. A. Fowler, *Nucleosynthesis in Supernovae*, ApJ, **132** (1960), p. 565

[51] W. Hillebrandt & J. C. Niemeyer, *Type IA Supernova Explosion Models*, ARA&A, **38** (2000), pp. 191–230

[52] A. G. Riess et al., *Observational Evidence from Supernovae for an Accelerating Universe and a Cosmological Constant*, AJ, **116** (1998), pp. 1009–1038

[53] H. A. Bethe, *Supernova mechanisms*, Reviews of Modern Physics, **62** (1990), pp. 801–866

[54] V. S. Berezinsky & O. F. Prilutsky, *Pulsars and Cosmic Rays in the Dense Supernova Shells*, A&A, **66** (1978), pp. 325–334

[55] H. Sato, *Pulsars Covered by the Dense Envelopes as High-Energy Neutrino Sources*, Progress of Theoretical Physics, **58** (1977), pp. 549–559

[56] R. Silberberg & M. M. Shapiro, *High-energy cosmic neutrinos and photons from point sources, and implications for galactic confinement*, *International Cosmic Ray Conference*, vol. 2 of *International Cosmic Ray Conference*, 1977 pp. 26–29

[57] G. Cavallo & F. Pacini, *Intensity and Sectrum of the Continuum Gamma Ray Emission from Supernovae*, A&A, **88** (1980), pp. 367–369

[58] T. K. Gaisser & T. Stanev, *Energetic (> 1 GeV) Neutrinos as a Probe of Acceleration in the New Supernova*, Physical Review Letters, **58** (1987), pp. 1695–1697

[59] R. J. Protheroe, *Photon-photon pair production and the opacity of SN1987A to TeV and PeV gamma-rays*, Nature, **329** (1987), pp. 135–138

[60] T. K. Gaisser, A. Harding & T. Stanev, *Particle acceleration and production of energetic photons in SN1987A*, Nature, **329** (1987), pp. 314–316

[61] M. Honda & M. Mori, *Calculation of UHE Neutrino Luminosity of SN1987A and UHE Gamma-Ray Flux from Underground Experiment*, Progress of Theoretical Physics, **78** (1987), pp. 963–968

[62] T. K. Gaisser, T. Stanev & F. Halzen, *Ultra-high energy radiation from young supernovae*, Nature, **332** (1988), p. 314

[63] J. E. Gunn & J. P. Ostriker, *Acceleration of High-Energy Cosmic Rays by Pulsars*, Physical Review Letters, **22** (1969), pp. 728–731

[64] V. S. Berezinsky & V. S. Ptuskin, *Radiation from young SN II shells produced by cosmic rays accelerated in shock waves*, A&A, **215** (1989), pp. 399–408

[65] V. S. Berezinsky & V. S. Ptuskin, *Radiation generated in young type-II supernova envelopes by shock-accelerated cosmic rays*, Soviet Astronomy Letters, **14** (1988), p. 304

[66] T. Nugis & H. J. G. L. M. Lamers, *Mass-loss rates of Wolf-Rayet stars as a function of stellar parameters*, A&A, **360** (2000), pp. 227–244

[67] D. K. Nadezhin, *On the initial phase of interaction between expanding stellar envelopes and surrounding medium*, Ap&SS, **112** (1985), pp. 225–249

[68] R. A. Chevalier, *The interaction of the radiation from a Type II supernova with a circumstellar shell*, ApJ, **251** (1981), pp. 259–265

[69] R. A. Chevalier, *The radio and X-ray emission from type II supernovae*, ApJ, **259** (1982), pp. 302–310

[70] J. G. Kirk, P. Duffy & L. Ball, *Radio supernovae as TeV gamma-ray sources.*, A&A, **293** (1995), pp. L37–L40

[71] D. Lennarz, C. Wiebusch & for the IceCube Collaboration, *Search for High Energetic Neutrinos from Supernova Explosions with AMANDA*, *International Cosmic Ray Conference*, International Cosmic Ray Conference, 2009

[72] D. Lennarz, *Search for High Energetic Neutrinos from Supernova Explosions with the AMANDA Neutrino Telescope*, Diploma's thesis, RWTH Aachen University (2009)

[73] D. Lennarz, D. Altmann & C. Wiebusch, *A unified supernova catalogue*, A&A, **538** (2012), A120

[74] R. Barbon, E. Cappellaro & M. Turatto, *The Asiago Supernova Catalogue*, A&AS, **81** (1989), p. 421

[75] R. Barbon et al., *The Asiago Supernova Catalogue - 10 years after*, A&AS, **139** (1999), pp. 531–536

[76] D. Y. Tsvetkov & O. S. Bartunov, *Sternberg Astronomical Institute supernova catalogue*, Bulletin d'Information du Centre de Donnees Stellaires, **42** (1993), p. 17

[77] D. Y. Tsvetkov, N. N. Pavlyuk & O. S. Bartunov, *The SAI Catalog of Supernovae and Radial Distributions of Supernovae of Various Types in Galaxies*, Astronomy Letters, **30** (2004), pp. 729–736

[78] I. A. Bond et al., *Upper limit for ultra-high-energy gamma rays from SN 1987A obtained by Cerenkov technique at large zenith angles*, ApJ, **344** (1989), pp. L17–L19

[79] A. K. Harding et al., *Gamma-rays from cosmic ray interactions in supernova shells*, *International Cosmic Ray Conference*, vol. 1 of *International Cosmic Ray Conference*, 1991 p. 105

[80] X. W. Liu et al., *The missing compact star of SN1987A: a solid quark star?*, ArXiv e-prints, (2012)

[81] R. A. Chevalier, *A Model for the X-Ray Luminosity of Pulsar Nebulae*, ApJ, **539** (2000), pp. L45–L48

[82] J. R. Marshall et al., *Asymptotic giant branch superwind speed at low metallicity*, MNRAS, **355** (2004), pp. 1348–1360

[83] T. L. Cline & U. D. Desai, *Progress in gamma ray burst astronomy*, B. G. Taylor, ed., *The Context and Status of Gamma-Ray Astronomy*, 1974 pp. 37–45

[84] C. A. Meegan et al., *Spatial distribution of gamma-ray bursts observed by BATSE*, Nature, **355** (1992), pp. 143–145

[85] C. Kouveliotou et al., *Identification of two classes of gamma-ray bursts*, ApJ, **413** (1993), pp. L101–L104

[86] P. N. Bhat et al., *Evidence of sub-millisecond structure in a gamma-ray burst*, Nature, **359** (1992), p. 217

[87] D. Band et al., *BATSE observations of gamma-ray burst spectra. I - Spectral diversity*, ApJ, **413** (1993), pp. 281–292

[88] K. Hurley et al., *Detection of a γ-ray burst of very long duration and very high energy*, Nature, **372** (1994), pp. 652–654

[89] M. M. González et al., *A γ-ray burst with a high-energy spectral component inconsistent with the synchrotron shock model*, Nature, **424** (2003), pp. 749–751

[90] J. van Paradijs et al., *Transient optical emission from the error box of the γ-ray burst of 28 February 1997*, Nature, **386** (1997), pp. 686–689

[91] D. A. Frail et al., *The radio afterglow from the γ-ray burst of 8 May 1997*, Nature, **389** (1997), pp. 261–263

[92] M. R. Metzger et al., *Spectral constraints on the redshift of the optical counterpart to the γ-ray burst of 8 May 1997*, Nature, **387** (1997), pp. 878–880

[93] T. J. Galama et al., *An unusual supernova in the error box of the γ-ray burst of 25 April 1998*, Nature, **395** (1998), pp. 670–672

[94] S. A. Colgate, *Prompt gamma rays and X-rays from supernovae.*, Canadian Journal of Physics, **46** (1968), p. 476

[95] S. R. Kulkarni et al., *The afterglow, redshift and extreme energetics of the γ-ray burst of 23 January 1999*, Nature, **398** (1999), pp. 389–394

[96] N. Gehrels et al., *A short γ-ray burst apparently associated with an elliptical galaxy at redshift $z = 0.225$*, Nature, **437** (2005), pp. 851–854

[97] F. Piron, J. McEnery & V. Vasileiou, *Fermi-LAT observations of long-lasting high-energy emission from GRB 090323 and GRB 090328*, J. E. McEnery, J. L. Racusin, & N. Gehrels, ed., *American Institute of Physics Conference Series*, vol. 1358 of *American Institute of Physics Conference Series*, 2011 pp. 47–50

[98] B.-B. Zhang et al., *A Comprehensive Analysis of Fermi Gamma-ray Burst Data. I. Spectral Components and the Possible Physical Origins of LAT/GBM GRBs*, ApJ, **730** (2011), 141

[99] A. A. Abdo et al., *Fermi Observations of High-Energy Gamma-Ray Emission from GRB 080916C*, Science, **323** (2009), pp. 1688–1693

[100] A. A. Abdo et al., *Fermi Observations of GRB 090902B: A Distinct Spectral Component in the Prompt and Delayed Emission*, ApJ, **706** (2009), pp. L138–L144

[101] M. Ackermann et al., *Fermi Observations of GRB 090510: A Short-Hard Gamma-ray Burst with an Additional, Hard Power-law Component from 10 keV To GeV Energies*, ApJ, **716** (2010), pp. 1178–1190

[102] W. H. G. Lewin, J. van Paradijs & R. E. Taam, *X-Ray Bursts*, Space Sci. Rev., **62** (1993), pp. 223–389

[103] J. Granot, E. Ramirez-Ruiz & R. Perna, *Afterglow Observations Shed New Light on the Nature of X-Ray Flashes*, ApJ, **630** (2005), pp. 1003–1014

[104] A. K. Harding & M. G. Baring, *Escape of High-Energy Photons from Relativistically Expanding Gamma-Ray Burst Sources*, G. J. Fishman, ed., *Gamma-Ray Bursts*, vol. 307 of *American Institute of Physics Conference Series*, 1994 p. 520

[105] T. Piran, *Gamma-ray bursts and the fireball model*, Phys. Rep., **314** (1999), pp. 575–667

[106] M. J. Rees & P. Meszaros, *Relativistic fireballs - Energy conversion and time-scales*, MNRAS, **258** (1992), pp. 41P–43P

[107] N. Gehrels, E. Ramirez-Ruiz & D. B. Fox, *Gamma-Ray Bursts in the Swift Era*, ARA&A, **47** (2009), pp. 567–617

[108] S. E. Woosley, *Gamma-ray bursts from stellar mass accretion disks around black holes*, ApJ, **405** (1993), pp. 273–277

[109] R. D. Blandford & R. L. Znajek, *Electromagnetic extraction of energy from Kerr black holes*, MNRAS, **179** (1977), pp. 433–456

[110] D. Eichler et al., *Nucleosynthesis, neutrino bursts and gamma-rays from coalescing neutron stars*, Nature, **340** (1989), pp. 126–128

[111] F. A. Aharonian, A. M. Atoyan & T. Kifune, *Inverse Compton gamma radiation of faint synchrotron X-ray nebulae around pulsars*, MNRAS, **291** (1997), pp. 162–176

[112] A. Franceschini, G. Rodighiero & M. Vaccari, *Extragalactic optical-infrared background radiation, its time evolution and the cosmic photon-photon opacity*, A&A, **487** (2008), pp. 837–852

[113] F. Aharonian et al., *A low level of extragalactic background light as revealed by γ-rays from blazars*, Nature, **440** (2006), pp. 1018–1021

[114] Y.-Z. Fan & T. Piran, *High-energy γ-ray emission from gamma-ray bursts - before GLAST*, Frontiers of Physics in China, **3** (2008), pp. 306–330

[115] B. Zhang & P. Mészáros, *High-Energy Spectral Components in Gamma-Ray Burst Afterglows*, ApJ, **559** (2001), pp. 110–122

[116] A. Levinson, *Particle Acceleration and Curvature TeV Emission by Rotating, Supermassive Black Holes*, Physical Review Letters, **85** (2000), pp. 912–915

[117] R. Abbasi et al., *An absence of neutrinos associated with cosmic-ray acceleration in γ-ray bursts*, Nature, **484** (2012), pp. 351–354

[118] F. Aharonian et al., *HESS observations of γ-ray bursts in 2003-2007*, A&A, **495** (2009), pp. 505–512

[119] J. Albert et al., *MAGIC Upper Limits on the Very High Energy Emission from Gamma-Ray Bursts*, ApJ, **667** (2007), pp. 358–366

[120] VERITAS Collaboration et al., *VERITAS Observations of Gamma-Ray Bursts Detected by Swift*, ArXiv e-prints, (2011)

[121] F. Aharonian et al., *HESS Observations of the Prompt and Afterglow Phases of GRB 060602B*, ApJ, **690** (2009), pp. 1068–1073

[122] R. Wijnands et al., *GRB060602B = Swift J1749.4-2807: an unusual transiently accreting neutron-star X-ray binary*, MNRAS, **393** (2009), pp. 126–132

[123] C. Pagani et al., *GRB 120328A: Swift detection of a burst.*, GRB Coordinates Network, **13147** (2012), p. 1

[124] D. N. Burrows et al., *GRB 120328A: Swift-XRT refined analysis.*, GRB Coordinates Network, **13159** (2012), p. 1

[125] C. B. Markwardt et al., *GRB 120328A: Swift-BAT refined analysis.*, GRB Coordinates Network, **13154** (2012), p. 1

[126] N. P. M. Kuin & W. H. Baumgartner, *GRB 120308A: Swift/UVOT detection.*, GRB Coordinates Network, **13025** (2012), p. 1

[127] T. N. Ukwatta et al., *GRB 100621A: Swift detection of a burst.*, GRB Coordinates Network, **10870** (2010), pp. 1–+

[128] P. A. Evans et al., *GRB 100621A: enhanced Swift-XRT position.*, GRB Coordinates Network, **10873** (2010), p. 1

[129] T. N. Ukwatta et al., *GRB 100621A: Swift-BAT refined analysis.*, GRB Coordinates Network, **10875** (2010), pp. 1–+

[130] B. Milvang-Jensen et al., *GRB 100621A: VLT/X-shooter redshift.*, GRB Coordinates Network, **10876** (2010), pp. 1–+

[131] V. La Parola et al., *GRB 081230: Swift detection of a burst.*, GRB Coordinates Network, **8753** (2008), p. 1

[132] V. La Parola, B. Sbarufatti & V. Mangano, *GRB081230: Swift-XRT refined analysis.*, GRB Coordinates Network, **8758** (2008), p. 1

[133] D. M. Palmer et al., *GRB 081230, Swift-BAT refined analysis.*, GRB Coordinates Network, **8759** (2008), p. 1

[134] J. L. Racusin et al., *GRB 080804: Swift detection of a burst with optical afterglow.*, GRB Coordinates Network, **8057** (2008), p. 1

[135] A. P. Beardmore et al., *GRB 080804: enhanced Swift-XRT position.*, GRB Coordinates Network, **8066** (2008), p. 1

[136] C. Markwardt et al., *GRB 080804, Swift-BAT refined analysis.*, GRB Coordinates Network, **8067** (2008), p. 1

[137] C. C. Thoene et al., *GRB 080804: UVES redshift.*, GRB Coordinates Network, **8058** (2008), p. 1

[138] A. Cucchiara et al., *GRB080804: Gemini south redshift confirmation.*, GRB Coordinates Network, **8065** (2008), p. 1

[139] A. P. Beardmore et al., *GRB 080413: Swift detection of a burst with an optical afterglow.*, GRB Coordinates Network, **7594** (2008), p. 1

[140] J. P. Osborne et al., *GRB 080413: enhanced Swift-XRT position.*, GRB Coordinates Network, **7596** (2008), p. 1

[141] J. Tueller et al., *GRB 080413A, Swift-BAT refined analysis.*, GRB Coordinates Network, **7604** (2008), p. 1

[142] C. C. Thoene et al., *GRB 080413A: VLT/UVES redshift.*, GRB Coordinates Network, **7602** (2008), p. 1

[143] A. Cucchiara, D. B. Fox & S. B. Cenko, *GRB 080413A: gemini-south spectroscopy.*, GRB Coordinates Network, **7616** (2008), p. 1

[144] A. M. Parsons et al., *GRB 070805: Swift detection of a burst.*, GRB Coordinates Network, **6708** (2007), p. 1

[145] M. Stamatikos et al., *GRB 070805, Swift-BAT refined analysis.*, GRB Coordinates Network, **6711** (2007), p. 1

[146] K. L. Page et al., *GRB 110625A: Swift detection of a burst.*, GRB Coordinates Network, **12088** (2011), p. 1

[147] K. L. Page, *GRB 110625A: Swift-XRT refined analysis.*, GRB Coordinates Network, **12092** (2011), p. 1

[148] D. M. Palmer et al., *GRB 110625A: Swift-BAT refined analysis.*, GRB Coordinates Network, **12091** (2011), p. 1

[149] F. E. Marshall et al., *GRB 100418A: Swift detection of a burst with a possible optical afterglow.*, GRB Coordinates Network, **10612** (2010), p. 1

[150] J. P. Osborne et al., *GRB 100418A: enhanced Swift-XRT position.*, GRB Coordinates Network, **10614** (2010), p. 1

[151] T. N. Ukwatta et al., *GRB 100418A: Swift-BAT refined analysis.*, GRB Coordinates Network, **10615** (2010), p. 1

[152] A. de Ugarte Postigo et al., *Time resolved spectroscopy of GRB 100418A and its host galaxy with X-shooter*, Astronomische Nachrichten, **332** (2011), p. 297

[153] A. Cucchiara & D. B. Fox, *GRB 100418A: Gemini-N redshift confirmation.*, GRB Coordinates Network, **10624** (2010), p. 1

[154] M. Stamatikos et al., *GRB 091018: Swift detection of a burst with optical afterglow.*, GRB Coordinates Network, **10034** (2009), p. 1

[155] J. P. Osborne et al., *GRB 091018: enhanced Swift-XRT position.*, GRB Coordinates Network, **10037** (2009), p. 1

[156] C. B. Markwardt et al., *GRB 091018: Swift-BAT refined analysis.*, GRB Coordinates Network, **10040** (2009), p. 1

[157] H.-W. Chen et al., *GRB091018: Magellan echellette observations.*, GRB Coordinates Network, **10038** (2009), p. 1

[158] S. R. Oates et al., *GRB 090201: Swift detection of a burst.*, GRB Coordinates Network, **8865** (2009), p. 1

[159] A. P. Beardmore et al., *GRB 090201: enhanced Swift-XRT position.*, GRB Coordinates Network, **8872** (2009), p. 1

[160] W. H. Baumgartner et al., *GRB 090201: Swift-BAT refined analysis.*, GRB Coordinates Network, **8870** (2009), p. 1

[161] E. A. Hoversten et al., *GRB 081221: Swift detection of a burst.*, GRB Coordinates Network, **8687** (2008), p. 1

[162] P. A. Evans et al., *GRB 081221: enhanced Swift-XRT position.*, GRB Coordinates Network, **8690** (2008), p. 1

[163] J. R. Cummings et al., *GRB 081221, Swift-BAT refined analysis.*, GRB Coordinates Network, **8708** (2008), p. 1

[164] R. Salvaterra et al., *A Complete Sample of Bright Swift Long Gamma-Ray Bursts. I. Sample Presentation, Luminosity Function and Evolution*, ApJ, **749** (2012), 68

[165] J. L. Racusin et al., *GRB 070920B: Swift detection of a burst.*, GRB Coordinates Network, **6808** (2007), p. 1

[166] J. L. Racusin, *GRB 070920B: XRT observations.*, GRB Coordinates Network, **6820** (2007), p. 1

[167] S. D. Barthelmy et al., *GRB 070920B, Swift-BAT refined analysis.*, GRB Coordinates Network, **6811** (2007), p. 1

[168] G. Stratta, V. D'Elia & T. N. Ukwatta, *GRB 100621A: Swift XRT refined analysis.*, GRB Coordinates Network, **10877** (2010), pp. 1–+

[169] F. Aharonian et al., *Evidence for VHE γ-ray emission from the distant BL Lac PG 1553+113*, A&A, **448** (2006), pp. L19–L23

[170] S. Golenetskii et al., *Konus-wind observation of GRB 100621A.*, GRB Coordinates Network, **10882** (2010), pp. 1–+

[171] D. Frederiks, private communication, (2012)

[172] T. Krühler et al., *The SEDs and host galaxies of the dustiest GRB afterglows*, A&A, **534** (2011), A108

[173] D. Gruber et al., *GRB 110625A: Fermi GBM and LAT observations.*, GRB Coordinates Network, **12100** (2011), p. 1

[174] P. H. T. Tam & A. K. H. Kong, *GRB 110625A: Fermi LAT detection.*, GRB Coordinates Network, **12097** (2011), p. 1

[175] P. H. T. Tam, A. K. H. Kong & Y.-Z. Fan, *Fermi Large Area Telescope observations of GRB 110625A*, ArXiv e-prints, (2012)

[176] F. E. Marshall et al., *The Late Peaking Afterglow of GRB 100418A*, ApJ, **727** (2011), 132

[177] S. T. Holland et al., *GRB 100418A: possible evidence for a supernova.*, GRB Coordinates Network, **10661** (2010), p. 1

[178] T. Nowak, *Development of an Automatic Response System to Gamma-Ray Burst Alerts for the H.E.S.S. Telescope Array*, Diploma's thesis, University of Erlangen (2008)